

**PLACE IN RETURN BOX** to remove this checkout from your record.  
**TO AVOID FINES** return on or before date due.  
**MAY BE RECALLED** with earlier due date if requested.

DATE DUE	DATE DUE	DATE DUE

SEARCH FOR LARGE EXTRA DIMENSIONS WITH DIPHOTON EVENTS AT  
CDF

By

Simona Murgia

A DISSERTATION

Submitted to  
Michigan State University  
in partial fulfillment of the requirements  
for the degree of

DOCTOR OF PHILOSOPHY

Department of Physics and Astronomy

2002

## ABSTRACT

### SEARCH FOR LARGE EXTRA DIMENSIONS WITH DIPHOTON EVENTS AT CDF

By

Simona Murgia

In spite of its undisputed success, the Standard Model is not a theory of everything as it does not incorporate gravity. Gravity is the weakest of all forces and its strength becomes comparable to the remaining forces at energies of the order of the Planck scale, at approximately  $10^{19}$  GeV and the Standard Model is viewed as an effective theory at energies below this scale. Recently, a model of large extra dimensions has been formulated by Arkani-Hamed, Dimopoulos, and Dvali that claims that the electroweak scale (approximately 1 TeV) is the only fundamental scale in nature and the fact that the Planck scale appears so large is an artifact of the existence of extra dimensions in which only gravity propagates. This theory can be tested at existing collider experiments, where energies sufficiently high to probe the extra dimensions can be achieved. In particular, the existence of extra dimensions can manifest itself with production of Standard Model particles through graviton mediated processes and thus it predicts an enhancement of production cross sections at high invariant mass. The goal of this work is to search for an excess in the  $100 \text{ pb}^{-1}$  of diphoton data collected with the Collider Detector at Fermilab at  $\sqrt{s} = 1.8$  TeV during the 1992-1996 run. No excess is observed and thus we place a 95% confidence level limit on the Planck scale in the bulk extra dimensions  $M_S$  of 899 GeV for constructive interference and of 797 GeV for destructive interference (Hewett convention).

This work is for my family; my parents, Antonietta and Piero, for their love and support, for teaching me everything and because I will always need them; my sisters and brothers, Pamela, Manola, Stefano, and Alessandro, for their love and friendship; and my husband, Tim, for his love, for being so great and for sharing his life with me.



## ACKNOWLEDGEMENTS

This work has been a challenging experience and I have benefitted of the expertise of many physicists. Above all, I am grateful to my advisor, Joey Huston, for teaching me the skills necessary to work in high energy physics, for giving me the chance to contribute with an interesting analysis, and for his constant support and encouragement during the years. I am very grateful to Bob Blair for helping me solve many technical problems and for always taking the time to discuss my work and to David Gerdes for his collaboration and for all that I have learned from them. I would also like to thank Steve Kuhlmann for many useful suggestions and discussions.

I thank Tim Tait for many useful discussions on particle physics and of the theory of Extra Dimensions in particular.

At CDF, I would also like to thank Peter Wilson, Henry Frisch, Raymond Culbertson, John Conway, John Carlson, YeonSei Chung, Beate Heinemann, Carmine Pagliarone for their interest in this analysis and for many useful discussions. At MSU, I would like to thank my committee members Carl Bromberg, Phil Duxbury, Carl Schmidt, and Gary Westfall. I also thank my fellow graduate students and post-docs Marina Brozovic, Gene Flanagan, Gervasio Gomez, Justin Lancaster, Valeria Tano, Matthias Tönnemann, Rocio Vilar for many interesting discussions and for always helping each other out.

# Contents

<b>LIST OF TABLES</b>	<b>viii</b>
-----------------------	-------------

<b>LIST OF FIGURES</b>	<b>x</b>
------------------------	----------

<b>1 The Standard Model</b>	<b>1</b>
1.1 Introduction . . . . .	1
1.2 Gauge Invariance . . . . .	2
1.3 Particles and Interactions . . . . .	4
1.4 Electroweak Symmetry Breaking . . . . .	7
1.5 Highlight of the Parton Model and Diphoton Production in $p\bar{p}$ Collisions	10
1.5.1 Parton Distribution Functions and Fragmentation . . . . .	11
1.5.2 Standard Model Diphoton Production . . . . .	14
<b>2 Large Extra Dimensions</b>	<b>17</b>
2.1 Introduction . . . . .	17
2.2 Large Extra Dimensions . . . . .	18
2.3 Kaluza-Klein Modes of Gravity . . . . .	20
2.4 Probing Large Extra Dimensions at CDF . . . . .	23
2.5 Conventions . . . . .	28
<b>3 The CDF Detector</b>	<b>31</b>
3.1 The Tevatron . . . . .	31
3.2 The CDF Detector . . . . .	34
3.3 The Tracking System . . . . .	35
3.3.1 The SVX . . . . .	35
3.3.2 The VTX . . . . .	36
3.3.3 The CTC . . . . .	37
3.4 The Central Preradiator . . . . .	39
3.5 The Calorimeters . . . . .	39

3.5.1	Central and End Wall Hadron Calorimeter . . . . .	40
3.5.2	Plug Calorimeter . . . . .	42
3.5.3	Forward Calorimeter . . . . .	44
3.6	The Muon Chambers . . . . .	44
3.7	Beam-Beam Counters . . . . .	46
3.8	The Trigger . . . . .	47
<b>4</b>	<b>The Event Data Sample</b>	<b>48</b>
4.1	Introduction . . . . .	48
4.2	Cluster . . . . .	49
4.3	The Central-Central Diphoton Event Sample . . . . .	49
4.3.1	Global Selection . . . . .	50
4.3.2	Photon Identification . . . . .	51
4.3.3	Isolation . . . . .	54
4.4	The Central-Plug Diphoton Event Sample . . . . .	55
4.4.1	Trigger . . . . .	55
4.4.2	Offline Selection . . . . .	57
4.5	Plug Photon Isolation . . . . .	60
4.5.1	Underlying Event in Run 1b Minimum Bias and $Z^0$ Events . .	62
4.5.2	Plug Clustering Algorithm . . . . .	64
4.6	Efficiencies . . . . .	68
4.6.1	Central-Central Diphoton Selection Efficiency . . . . .	69
4.6.2	Central-Plug Diphoton Selection Efficiency . . . . .	70
4.7	Summary . . . . .	76
4.8	Acceptance $\times$ Efficiency for a Higgs decaying to $\gamma\gamma$ . . . . .	76
<b>5</b>	<b>Background Study</b>	<b>85</b>
5.1	Introduction . . . . .	85
5.2	Standard Model $\gamma\gamma$ Contribution in the Central-Plug Diphoton Sample	86
5.3	Purity of the Central-Plug Diphoton Sample . . . . .	87
5.3.1	$N_{ff}^{CP} + N_{f\gamma}^{CP}$ Estimate . . . . .	90
5.3.2	$N_{\gamma f}^{CP}$ Estimate . . . . .	91
5.3.3	Central-Plug Fake Estimate-Summary . . . . .	94
5.3.4	Shape of the Fake Invariant Mass Distribution . . . . .	94
5.3.5	Performance of the Single Arm Weighting Method for Central Diphotons . . . . .	95

5.4	Central-Plug Background Summary . . . . .	98
5.5	Background in the Central-Central Diphoton Sample . . . . .	98
5.6	Combined CC+CP Diphoton Sample - Background . . . . .	100
<b>6</b>	<b>Limit on Large Extra Dimensions with Central-Plug Diphotons</b>	<b>107</b>
6.1	Introduction . . . . .	107
6.2	$p\bar{p} \rightarrow \gamma\gamma X$ Differential Cross Section . . . . .	108
6.2.1	SM $\gamma\gamma$ and Fakes Mass Spectra . . . . .	108
6.2.2	The LED Monte Carlo Samples . . . . .	109
6.3	Likelihood Function . . . . .	111
6.4	Performance of the Fitter . . . . .	114
6.5	Monte Carlo Sensitivity . . . . .	121
6.6	Limits . . . . .	125
6.7	Systematics . . . . .	125
6.8	Limits with Systematics Included . . . . .	129
6.9	Conclusions . . . . .	129
<b>7</b>	<b>Limit on Large Extra Dimensions with Central and Plug Diphotons</b>	<b>136</b>
7.1	Combined Likelihood Function . . . . .	136
7.2	Performance of the Fit . . . . .	139
7.3	Monte Carlo Sensitivity for the Central-Central and Central-Plug Com- bined Sample . . . . .	139
7.4	Data $\eta_{95}$ . . . . .	141
7.5	Systematic Effects . . . . .	142
7.6	Combined Limits . . . . .	143
<b>8</b>	<b>Conclusions</b>	<b>148</b>
	<b>LIST OF REFERENCES</b>	<b>153</b>

# List of Tables

1.1	Vector boson masses[4]. . . . .	7
1.2	Lepton and quark masses[4]. . . . .	8
1.3	Quantum numbers of the fermions. . . . .	8
4.1	Efficiencies for the isolated 23 GeV trigger up to $E_T=55$ GeV and for the non-isolated 50 GeV trigger for $E_T > 55$ GeV. . . . .	57
4.2	Plug cluster selection and events passing. . . . .	61
4.3	Efficiencies and correction factors for global event selection and central photon identification cuts. In the table, ETOUT means out-of-time energy. . . . .	70
4.4	Efficiencies for the plug photon identification cuts (statistical uncertainty only). . . . .	75
4.5	Events in the Central-Plug diphoton sample that pass the $W^\pm/Z^0$ selection. . . . .	80
5.1	Systematic uncertainties from CES and CPR weighting. The total systematic error is determined by adding the contributions in quadrature. . . . .	91
5.2	Summary of predicted and observed events in the Central-Plug diphoton sample. . . . .	99
6.1	$\delta\eta_{95}$ in $TeV^{-4}$ corresponding to the systematic uncertainties incorporated into the limit for $\lambda = -1$ . . . . .	127
6.2	$\delta\eta_{95}$ in $TeV^{-4}$ corresponding to the systematic uncertainties incorporated into the limit for $\lambda = +1$ . . . . .	128
7.1	$\delta\eta_{95}$ in $TeV^{-4}$ corresponding to the systematic uncertainties incorporated into the combined limit for $\lambda = -1$ and $\lambda = +1$ . . . . .	143
8.1	$M_S^{95}$ in Hewett convention for the Central-Central (CC) and Central-Plug (CP) samples individually and combined (CC+CP) with $K = 1.0$ . . . . .	150
8.2	Dielectron and diphoton limits on $M_S$ in Hewett, GRW, HLZ conventions. The combined dielectron and diphoton limit ( $e^+e^-+\gamma\gamma$ ) has been determined for $K = 1.0$ and $K = 1.3$ . . . . .	150

8.3	D0 combined dielectron and diphoton limits on $M_S$ in Hewett, GRW, HLZ conventions with $K = 1.3$ . Limits are expressed in $TeV$ . . . .	151
-----	--	-----

# List of Figures

1.1	Sketch of the potential energy for a real field $\phi$ . . . . .	10
1.2	This picture schematically represents the factorization of the $p\bar{p} \rightarrow C + X$ scattering into the parton distribution functions $G$ , the cross section of the hard scattering $\hat{\sigma}$ and the fragmentation functions $D$ . . . . .	15
1.3	Representative Feynman diagrams for Standard Model diphoton production . . . . .	16
2.1	Schematic view of the effect of extra dimensions on field lines . . . . .	19
2.2	Representative graviton interaction vertices in linearized quantum gravity . . . . .	23
2.3	Examples of real graviton emission (left) and virtual graviton emission (right). $f$ refers to the SM quarks and leptons and $A$ are the SM gauge fields $\gamma$ , $W$ , $Z$ or gluon. . . . .	24
2.4	Feynman diagrams for LED diphoton production . . . . .	24
2.5	Invariant mass distribution of SM and SM+LED $\gamma\gamma$ events. LED events are simulated with $M_{S,Hewett}=600$ GeV and $\lambda=-1$ . . . . .	28
2.6	Invariant mass distribution for SM+LED $\gamma\gamma$ events in case of destructive ( $\lambda=+1$ ) and constructive ( $\lambda=-1$ ) interference for $M_S = 600$ GeV . . . . .	29
3.1	Schematic view of the Fermilab Tevatron and the different stages of acceleration for the protons and the antiprotons . . . . .	32
3.2	Cross section of an upper quarter of the CDF detector . . . . .	33
3.3	Isometric view of one of the SVX barrels . . . . .	35
3.4	SVX ladder . . . . .	36
3.5	Cross sectional view of the VTX (left) and schematic view of one wedge (right) . . . . .	37
3.6	Transverse view of the CTC. The superlayers and the tilted cells are shown . . . . .	38
3.7	$\eta$ , $\phi$ segmentation of central, plug, end wall and forward calorimeters . . . . .	42
3.8	Anode wires and cathode strips in the CES . . . . .	43
3.9	Absorber sheet, proportional tubes, and cathode pads in one layer of the PEM . . . . .	44
3.10	Proportional tubes in the PHA . . . . .	45

3.11	Location of the CMU modules with respect to the central calorimeter	46
4.1	$\eta$ dependence of the cone 0.4 isolation $E_T(Z^0 \rightarrow e^+e^- \text{ events})$	62
4.2	$E_T$ in cone vs $\eta$ in minimum bias events	64
4.3	$E_T$ in cone vs $\eta$ in $Z^0 \rightarrow e^+e^-$ events.	65
4.4	Number of towers included in a cluster in $Z^0 \rightarrow e^+e^-$ events $ \eta $	66
4.5	$\eta$ dependence of the annulus $E_T$ ( $Z^0 \rightarrow e^+e^-$ events)	67
4.6	$\eta$ dependence of the efficiency for annulus (squares) and cone 0.4 isolation (circles) $E_T$ ( $Z^0 \rightarrow e^+e^-$ events)	68
4.7	Efficiency of the Annulus $E_T$ (circles) and Cone 0.4 (triangles) isolation versus $E_T$ ( $Z^0 \rightarrow e^+e^-$ events)	69
4.8	$\eta$ dependence of the efficiency for the VTX occupancy cut (minimum bias events)	72
4.9	$\eta$ and $E_T$ dependence of the efficiency for the plug cuts ( $Z^0 \rightarrow e^+e^-$ events)	73
4.10	$\eta$ and $E_T$ dependence of the efficiency for the plug cuts ( $Z^0 \rightarrow e^+e^-$ events)	74
4.11	Invariant mass distribution of the events in the Central-Plug diphoton sample	77
4.12	Invariant mass distribution of the events in the CDF diphoton sample. The contributions from the Central-Plug sample and Central-Central sample are also shown	78
4.13	Acceptance $\times$ efficiency for Pythia Higgses of different masses. The triangles show the acceptance $\times$ efficiency for Central-Central diphotons and the squares for the Central-Central and Central-Plug combined.	81
4.14	Invariant mass distribution for events with one or more jets in addition to two photons for the Central-Plug diphoton selection (circles) and for the CC and CP samples combined (squares)	82
4.15	Invariant mass distribution for events with two or more jets in addition to two photons for the Central-Plug diphoton selection (circles) and for the CC and CP samples combined (squares)	83
4.16	Invariant mass distribution for events passing the $W^\pm/Z^0$ requirements in addition to the diphoton selection for the Central-Plug diphoton selection (circles) and for the CC and CP samples combined (squares)	84
5.1	$\gamma\gamma$ contribution from $q\bar{q} \rightarrow \gamma\gamma$ and $gg \rightarrow \gamma\gamma$ in the Central-Plug diphoton sample	87
5.2	Fractional contribution from $q\bar{q} \rightarrow \gamma\gamma$ and $gg \rightarrow \gamma\gamma$ in the Central-Plug diphoton sample	88
5.3	Cone 0.4 isolation distribution for jets in the dijet sample that pass the annulus isolation cut in the Central-Plug diphoton sample	101



5.4	Ratio between the $\pi^0\pi^0$ and $\gamma\pi^0$ cross sections versus the invariant mass of the pair . . . . .	102
5.5	Cone 0.4 isolation distribution for jets in the dijet sample that pass the annulus isolation cut in the sample containing central diphotons . . .	103
5.6	Combined SM $\gamma\gamma$ +fake contribution in the control diphoton sample .	104
5.7	SM $\gamma\gamma$ and fake contributions in the Central-Plug diphoton sample .	105
5.8	SM $\gamma\gamma$ and fake contributions in the combined Central-Plug and Central-Central diphoton sample . . . . .	106
6.1	Turn-on curve . . . . .	110
6.2	Top: Invariant mass distribution for the Monte Carlo SM $\gamma\gamma$ events after the CP selection has been applied. The solid line is a fit of the distribution. Bottom: close up in linear scale of the peak region of the picture on top. The fit parameters are displayed in the legend . . . .	115
6.3	Top: Invariant mass distribution for the Monte Carlo SM $\gamma+jet$ events after the CP selection has been applied. The solid line is a fit of the distribution. Bottom: close up in linear scale of the peak region of the picture on top. The fit parameters are displayed in the legend . . . .	116
6.4	Invariant mass distribution for the Monte Carlo events resulting from the interference between the SM and LED processes after the CP selection has been applied. The solid line is a fit of the distribution. The fit parameters are displayed in the legend . . . . .	117
6.5	Invariant mass distribution for the Monte Carlo direct KK events after the CP selection has been applied. The solid line is a fit of the distribution. The fit parameters are displayed in the legend . . . . .	118
6.6	Invariant mass distribution for pseudoexperiments in presence of extra dimensions generated with $\lambda = -1$ and $M_S=600$ GeV . . . . .	119
6.7	Invariant mass distribution for pseudoexperiments in presence of extra dimensions generated with $\lambda = +1$ and $M_S=600$ GeV . . . . .	120
6.8	Fitted values of $M_S$ (top plot) and $\eta$ (bottom plot) for $\lambda=-1$ . The gaussian fit is shown. The mean value of the distribution agrees well with value of $M_S^{true}$ used to generate the pseudoexperiments . . . . .	122
6.9	Fitted values of $n_{SM}$ (top plot) and $n_b$ (bottom plot) for $\lambda=-1$ . . . .	123
6.10	Invariant mass distribution for pseudoexperiments in absence of extra dimensions ( $\eta = 0$ ) . . . . .	124
6.11	Top: distribution of $\eta_{95}$ for the 1000 pseudoexperiments and median for $\lambda = -1$ . Bottom: same as in the top plot but for $\lambda = +1$ . . . . .	130
6.12	Top: Likelihood function for equally spaced values of $\eta$ for the events in the CP data sample ( $\lambda = -1$ ). Bottom: same as in the top plot but for $\lambda = +1$ . . . . .	131
6.13	Default fit to the $\gamma + jet$ invariant mass distribution for Pythia events (dashed line). The two variation of the shape included in the limit as a systematic uncertainty are also displayed . . . . .	132

6.14	Ratio between the $\pi^0\pi^0$ and $\gamma\pi^0$ cross sections versus the invariant mass of the pair. Fit with a polynomial (dashed line). $\pm 1\sigma$ shift (dotted and dash-dotted lines) . . . . .	133
6.15	Top: Smeared likelihood function for $\lambda = -1$ for the events in the CP data sample. Bottom: same as in the top plot but for $\lambda = +1$ . . . .	134
6.16	The circles represent the Central-Plug data. The LED signal corresponding to the $\lambda = -1$ limit is superimposed . . . . .	135
7.1	$\eta_{fit}$ ( $\eta$ that minimizes the likelihood function) versus $\eta_{true}$ ( $\eta$ used to generate pseudoexperiments). The linear correspondence exemplifies the fact that the likelihood function correctly interprets the data in the presence of extra dimensions . . . . .	140
7.2	$\eta_{95}$ for the pseudoexperiments. One entry per pseudoexperiment . . .	141
7.3	Unsmeared (top) and smeared (bottom) likelihood function for the combined CC+CP diphoton data sample for $\lambda = -1$ . . . . .	144
7.4	Unsmeared (top) and smeared (bottom) likelihood function for the combined CC+CP diphoton data sample for $\lambda = +1$ . . . . .	145
7.5	Invariant mass distribution for the diphoton data (circles) overlapped with the expected invariant mass distribution from SM $\gamma\gamma$ +fake sources. The excluded contribution from the direct KK graviton exchange and SM+KK interference is also shown. The LED contribution corresponds to approximately 5 events . . . . .	146
7.6	Invariant mass distribution for the diphoton data (circles) overlapped with the expected invariant mass distribution from SM $\gamma\gamma$ +fake sources combined with the excluded contribution from LED sources. The invariant mass contribution from SM $\gamma\gamma$ +fake sources alone is also shown	147

Images in this dissertation are presented in color.

# Chapter 1

## The Standard Model

### 1.1 Introduction

The Standard Model (SM) is the theory of the particles and the interactions that are ultimately responsible for building the universe we live in. The Standard Model has so far been very successful in explaining the phenomena we observe in nature and its validity has been confirmed when the model led to several predictions that were verified by the experiments, including the discovery of the top quark in the mid-nineties and of the  $W^\pm$  and the  $Z^0$  gauge bosons about 10 years earlier. The last milestone of the Standard Model would be to discover the Higgs boson which has eluded the experiments so far. Although the model is built on very solid grounds, some questions are still unanswered and more work is being done that will either confirm the SM or lead to the discovery of new physics through the common effort of theoretical and experimental particle physicists. In this chapter we will highlight the important parts of the Standard Model[1]. In the next chapter, shortcomings of the Standard Model will be discussed and the theory of Large Extra Dimensions by Arkani-Hamed, Dimopoulos, and Dvali [8], that among other theories attempts to address these issues, will be introduced.

The goal of the analysis presented in this dissertation is to search for large ex-

tra dimensions by studying prompt (or direct) diphoton production at the Tevatron Collider Detector at Fermilab (CDF) and looking for a deviation from the Standard Model prediction that arises from graviton-mediated diphoton production, where the gravitons can propagate in the extra dimensions. The last few sections of this chapter will be devoted to explaining prompt diphoton production in the Standard Model. Diphoton production in the presence of large extra dimensions will be addressed in the next chapter.

## 1.2 Gauge Invariance

In particle physics, it is of fundamental importance that requiring invariance of the theory under transformations in internal spaces dictates the form of interactions between fields, i.e. interactions and their associated currents can be derived. Gauge invariance also leads to quantities being conserved. So far three symmetries have been discovered in nature. They are  $U(1)$ ,  $SU(2)$ ,  $SU(3)$ . Why it is these three particular transformations and if there are more symmetries yet to be discovered is at this time unknown.

The Lagrangian for fermions can be written starting from the Dirac action and substituting the covariant derivative for the regular space-time derivative in order to preserve local gauge invariance under  $U(1) \times SU(2) \times SU(3)$  transformations. Formally, the covariant derivative can be written as:

$$D_\mu = \partial_\mu + i g_1 \frac{Y}{2} B_\mu + i g_2 \tau^j W_\mu^j + i g_3 \lambda^a G_\mu^a, \quad (1.1)$$

where  $g_1, g_2, g_3$  are the strengths of the respective interactions. The last three terms are added to preserve the invariance of the Lagrangian under transformations of the fields of the kind:

$$\Psi(x) \rightarrow e^{i\alpha^a(x)T^a} \Psi(x), \quad (1.2)$$

where  $\alpha$  is the space-time dependent phase of the transformation and  $T$  are the generators of the transformation. The index  $a$  runs from one to the number of degrees of freedom of the transformation and there is a vector boson associated with each degree of freedom.

The first term in equation 1.1 is the space-time derivative. The second term is added to preserve invariance under  $U(1)$  transformations.  $B_\mu$  is the spin one field that is introduced to preserve invariance and  $Y$  is a constant that represents the hypercharge and can be different for the different fermions.  $B_\mu$  couples to  $Y$  with strength  $g_1$ . The third term guarantees invariance under  $SU(2)$  rotations in the weak isospin space. The three vector bosons associated with these transformations are  $W_\mu^j$  ( $j=1,2,3$ ), and the  $\tau^j$  are the generators of the transformation. In matrix representation the  $\tau^j$  are 1/2 times the Pauli matrices.  $W_\mu^j$  couples to the weak isospin with strength  $g_2$ . As it will be explained in section 1.4, the  $U(1) \times SU(2)$  symmetry is broken and the  $B$  and  $W$  fields mix:

$$A^\mu = B^\mu \cos \theta_W + W_3^\mu \sin \theta_W \quad (1.3)$$

$$Z^\mu = -B^\mu \sin \theta_W + W_3^\mu \cos \theta_W \quad (1.4)$$

with:

$$\tan \theta_W = \frac{g_1}{g_2}, \quad (1.5)$$

where  $\theta_W$  is the Weinberg angle and determines the mixing between the  $B^\mu$  and  $W_3^\mu$  currents.  $A^\mu$  represents the spin-1 vector boson for the electromagnetic interaction, the photon.  $A^\mu$  couples to the electric charge  $Q = \tau^3 + Y/2$  ( $\tau^3$  is the third component of the weak isospin of the fermion) with strength  $e$ . The quantum field theory of the electromagnetic interaction is called QED (quantum electrodynamics) and is a well understood theory.  $Z_\mu$  represents the neutral current interaction carried by the  $Z^0$

boson.  $Z^\mu$  couples to  $Q_Z = (\tau^3 - Q \sin^2 \theta_W)$  with strength  $e/(\sin \theta_W \cos \theta_W)$ . The *remaining*  $SU(2)$  fields ( $W_1^\mu, W_2^\mu$ ) provide the charged weak interaction carried by the  $W^\pm$  bosons and couple with strength  $g_2$  to  $\tau^1$  and  $\tau^2$ .

Finally, the fourth term in equation 1.1 preserves  $SU(3)$  invariance which is responsible for the interaction between particles that have a color charge. The color is a property that strongly interacting particles carry, analogous to the electric charge for electromagnetic interaction. Its vector bosons,  $G_\mu^a$  ( $a=1,\dots,8$ ), are eight gluons and couple to color with strength  $g_3$ . The eight fields differ by the combination of color they carry. The quantum field theory of strongly interacting particles is known as QCD (quantum chromodynamics). QCD is reasonably well understood at high energies, but poorly understood at low energies.

### 1.3 Particles and Interactions

The framework of the Standard Model consists of particles and their interactions. We have explained how the invariance of a theory with respect to gauge transformations implies the existence of associated fields that describe the interaction between the particles in the theory. In perturbative quantum field theory the interactions are described as the exchange of field quanta, the vector bosons. The vector bosons are all spin one particles. The photons and the gluons are massless, while the  $Z^0$  and the  $W^\pm$  are massive. Vector bosons do not make the building blocks of matter, but they are ultimately responsible for holding it together. The vector boson masses are listed in table 1.1.

Matter is made out of fermions. Fermions are spin  $\frac{1}{2}$  particles and are divided into leptons and quarks. Left-handed leptons are  $SU(2)$  doublets. In matrix notation, the upper component of the doublet is the left handed neutrino and the lower component

is the left handed electron:

$$L_L = \begin{pmatrix} \nu_e \\ e \end{pmatrix}_L. \quad (1.6)$$

Because of the Higgs mechanism (see section 1.4),  $SU(2)$  invariance is broken which allows us to physically distinguish  $e_L$  and  $\nu_e$ . If the symmetry were exact, they would be indistinguishable. The neutrino is neutral and thus does not interact electromagnetically (in other words it does not couple to photons) while the electron has charge  $-1$  and interacts with other charged particles through the exchange of photons. Under rotation in the weak isospin space, left handed neutrinos turn into left handed electrons through the charged current interaction, i.e. the exchange of a  $W$  boson. In addition, left handed leptons couple to the  $Z$  by making the transitions  $e_L \rightarrow Z^0 e_L$ ,  $\nu_L \rightarrow Z^0 \nu_L$  possible. Right handed neutrinos do not couple weakly and strictly speaking are not included in the Standard Model. As a consequence in the Standard Model neutrinos are massless and their interactions violate parity. Right handed electrons form singlets in the weak isospin space and thus do not interact with the  $W$  boson. However neutral current interactions via  $Z$  exchange are allowed. Leptons are colorless and do not interact strongly.

Quarks feel the electroweak interaction in much the same way as just described for the leptons. Left handed quarks form doublets in the weak isospin space. The upper component of the doublet is the left handed up quark and the lower component is the left handed down quark:

$$Q_L = \begin{pmatrix} u \\ d \end{pmatrix}_L. \quad (1.7)$$

The right handed up and down quarks are weak singlets. Just as described for the leptons, charged current transitions are not allowed for  $u_R$  and  $d_R$ . Up and down quarks are electrically charged and thus couple to photons. Furthermore, they form

triplets in the  $SU(3)$  color space:

$$q = \begin{pmatrix} q_r \\ q_g \\ q_b \end{pmatrix}. \quad (1.8)$$

The subscripts  $r, g$  and  $b$  refer to the color charge (red, green and blue). Particles carrying color charge interact through the exchange of gluons. Since gluons themselves carry color, they interact with each other. This property of the strong interaction leads to the concepts of *confinement* and *asymptotic freedom*. Confinement refers to the observation that quarks and gluons do not exist in a free state and will be explained in section 1.5.1. Asymptotic freedom is a consequence of the fact that the strong coupling  $\alpha_s$  runs with the energy scale (at leading order):

$$\alpha_s(\mu) = \frac{12\pi}{(33 - 2n_f) \ln \frac{\mu^2}{\Lambda_{QCD}^2}}. \quad (1.9)$$

In equation 1.9,  $\mu$  is the energy scale,  $\Lambda_{QCD}$  is the scale where QCD becomes strong ( $\Lambda_{QCD} \sim 200$  MeV), and  $n_f$  is the number of light quark flavors. Equation 1.9 dictates that at large  $\mu^2$  (high momentum transfer or, conversely, small distances)  $\alpha_s$  becomes smaller and thus quarks behave more and more as if they were free. On the other hand, as  $\mu^2$  decreases,  $\alpha_s$  becomes larger. For  $\mu^2 \rightarrow \Lambda_{QCD}^2$ ,  $\alpha_s$  is very large, confinement occurs and quarks form colorless bound states called *hadrons* held together through the strong force. Bound states of a quark and an antiquark are called *mesons* and have integer spin, while bound states of three quarks are known as *baryons* and have 1/2-integer spin. Quark masses are measured by probing hadrons and depend on the energy scale.

The only leptons we have mentioned so far are the electron ( $e$ ) and the electron neutrino ( $\nu_e$ ) and the only quarks are the up and the down quarks. These fermions constitute a family in the Standard Model. The Standard Model includes three



Table 1.1: Vector boson masses[4].

Particle	Symbol	Mass (GeV)	
Photon	$A$	0	Electromagnetic Force
W Boson	$W^\pm$	80.42	Charged Weak Force
Z Boson	$Z^0$	91.188	Neutral Weak Force
Gluon	$G^a$	0	Strong Force

families. The second and the third families have exactly the same quantum numbers and gauge interactions as described previously for the first family, but heavier masses. Each family consists of up- and down-type quarks and a lepton and its neutrino. It is important to point out that although the three families carry identical quantum numbers, thus interacting in exactly the same way, the Universe around us is made out of only the first generation fermions. The rest of the particles can be produced in nature, created in the upper atmosphere by interaction with high energy cosmic rays or in accelerators, but are very short lived. To complete the picture, for every particle there is a corresponding antiparticle that has the same spin as the particle, but opposite charges. A summary of quark and lepton masses can be found in table 1.2. The quantum numbers for the fermions in the first family are listed in table 1.3.

## 1.4 Electroweak Symmetry Breaking

We have seen in the previous section that photons and gluons are massless while the  $W^\pm$  and  $Z^0$  bosons as well as the fermions are massive. Mass terms cannot be inserted by hand in the Lagrangian as they would break gauge invariance. On the other hand, gauge invariance must be a property of the Lagrangian otherwise unrenormalizable divergences would appear in the theory in loop calculations. The Higgs mechanism

Table 1.2: Lepton and quark masses[4].

Particle	Symbol	Pole Mass (GeV)	
Electron neutrino	$\nu_e$	0	
Electron	$e$	0.00051	First Generation
Up quark	$u$	0.001 to 0.005	
Down quark	$d$	0.003 to 0.009	
Muon neutrino	$\nu_\mu$	0	
Muon	$\mu$	0.106	Second Generation
Charm quark	$c$	1.15 to 1.35	
Strange quark	$s$	0.075 to 0.170	
Tau neutrino	$\nu_\tau$	0	
Tau	$\tau$	1.78	Third Generation
Top quark	$t$	174	
Bottom quark	$b$	4.0 to 4.4	

Table 1.3: Quantum numbers of the fermions.

Particle	$Q$	$\tau^3$	$Y$	$C$
$\nu_{eL}$	0	1/2	-1	0
$e_L$	-1	-1/2	-1	0
$u_L$	2/3	1/2	1/3	$r, g, b$
$d_L$	-1/3	-1/2	1/3	$r, g, b$
$e_R$	-1	0	-2	0
$u_R$	2/3	0	4/3	$r, g, b$
$d_R$	-1/3	0	-2/3	$r, g, b$

solves this problem by giving masses to the  $W$ ,  $Z$ , and the fermions while leaving the photon and the gluon massless. This is achieved by introducing a spin-zero field which is a  $SU(2)$  doublet that does not couple strongly and has hypercharge  $Y = +1$ . This is the Higgs doublet:

$$\phi = \sqrt{\frac{1}{2}} \begin{pmatrix} \phi_1 + i\phi_2 \\ \phi_3 + i\phi_4 \end{pmatrix}, \quad (1.10)$$

where  $\phi_1, \phi_2, \phi_3$ , and  $\phi_4$  are real fields. Let us consider this field in a potential  $V$ . The general renormalizable form for  $V$  is:

$$V(\phi) = \mu^2 \phi^\dagger \phi + \lambda (\phi^\dagger \phi)^2, \quad (1.11)$$

where  $\mu$  and  $\lambda$  are arbitrary constants. One proceeds to find the minimum of the potential and subsequently to expand the field  $\phi$  around the minimum. For  $\mu^2 > 0$  the potential has a minimum at  $\phi^\dagger \phi = 0$  and this case is not interesting as the symmetry is unbroken and everything remains massless. However, by choosing  $\mu^2 < 0$ , the minimum of the potential is:

$$\phi^\dagger \phi = \frac{-\mu^2}{2\lambda} = \frac{v^2}{2}. \quad (1.12)$$

There is more than one minimum that satisfies equation 1.12 and thus there is a set of vacuum expectation values (vev's) corresponding to each choice obeying equation 1.12. Choosing one minimum is what breaks the  $U(1) \times SU(2)$  symmetry. This is easier to visualize in the case of a real scalar field. In this case there are two possible minima of the potential,  $\pm v$ . The potential is sketched in figure 1.1.

By choosing  $\phi_1 = \phi_2 = \phi_4 = 0$  and  $\phi_3 = v$ , the ground state is:

$$\phi_0 = \sqrt{\frac{1}{2}} \begin{pmatrix} 0 \\ v \end{pmatrix}. \quad (1.13)$$

The next step consists of expanding  $\phi$  around the minimum:

$$\phi = \sqrt{\frac{1}{2}} \begin{pmatrix} 0 \\ v + H(x) \end{pmatrix}, \quad (1.14)$$

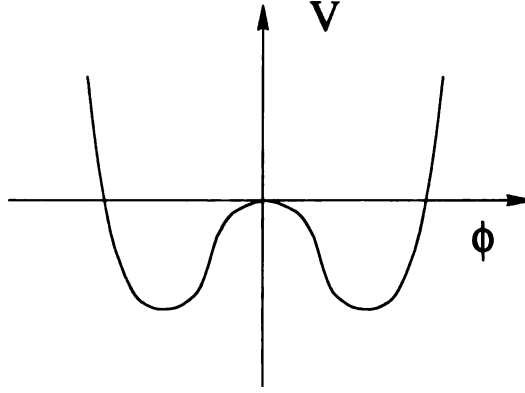


Figure 1.1: Sketch of the potential energy for a real field  $\phi$ .

where  $H$  is the physical Higgs particle.  $\phi_1, \phi_2$  and  $\phi_4$  would correspond to massless boson fields introduced by choosing a direction in the  $\phi$  space thus breaking three global symmetries. They do not correspond to physical particles and are incorporated in the  $W^\pm$  and  $Z^0$  by field redefinitions to provide the longitudinal polarization states. Substituting  $\phi$  in the Lagrangian, introduces mass terms for the  $W$  and the  $Z$ :

$$M_W = \frac{vg_2}{2} \quad (1.15)$$

$$M_Z = \frac{1}{2}v\sqrt{g_1^2 + g_2^2} \quad (1.16)$$

$v$  can be extracted from experimental measurements and its value is 246 GeV. The photon field  $A^\mu$  remains massless as the  $U(1)$  symmetry is not broken. By the same mechanism, the Higgs field acquires a mass itself  $m_{H^0} = \sqrt{2\lambda v^2}$ . Fermions acquire their masses by interacting with the Higgs field. Since the Higgs is what introduces masses, its coupling to particles is proportional to the mass of the particles, thus the heavier is the particle, the stronger is the strength of the coupling to the Higgs boson.

## 1.5 Highlight of the Parton Model and Diphoton Production in $p\bar{p}$ Collisions

At the Fermilab Tevatron, protons collide with antiproton beams with a center of mass energy of 1.8 TeV. At these energies, the constituents of the protons and of

the antiprotons are capable of producing hard scatterings, i.e. high momentum interactions between their constituents. This very fact, that hadrons are not point-like particles, makes it difficult to compute cross sections in hadron collisions. In section 1.5.1 the parton model will be briefly introduced and the factorization theorem will be discussed to explain how cross sections are calculated in hadron collisions[2]. In section 1.5.2, diphoton production in a hadron collider will be briefly discussed[3].

### 1.5.1 Parton Distribution Functions and Fragmentation

Electron-proton deeply inelastic scattering (DIS) experiments have probed the structure of the proton and have demonstrated that protons are not point-like particles. When the momentum of the photon in the electron-proton interaction is large and thus the wavelength is small enough to discern the partons inside the proton, the measured cross-section is approximately independent of the momentum transferred  $q^2 = -Q^2$ , while it only depends on the fraction of the proton momentum  $x$  carried by the interacting parton (this is known as Bjorken scaling). This occurs only if the partons in the proton interact with the photon as point-like free particles (the fact that partons inside the proton act as free particles when probed at high energies, is a result of asymptotic freedom, described in section 1.3). The cross section for the process can be factorized into the product of the cross section  $\hat{\sigma}$  for the photon-parton hard (i.e. high momentum) scattering, the parton distribution functions (PDF's) and the fragmentation functions.  $\hat{\sigma}$  can be calculated perturbatively from first principles, while the PDF's and the fragmentation functions represent the low momentum, large distance non-perturbative (high  $\alpha_s$ ) part that cannot be calculated from first principles but can be measured. Proton PDF's measure the probability for the partons to have a fraction of the proton momentum  $x$ . The PDF's are universal, meaning that they can be measured for a certain DIS process, but they can be used in calculations

of the cross section for other processes (to measure PDF's constraints from data are added to a fit). It is possible to extrapolate the PDF's to different values of  $Q^2$  if they are known at a particular value of  $Q^2$  and  $x$  through evolution equations (Altarelli-Parisi equations determined from perturbative QCD). Different sets of PDF's exist, and the most popular are from the CTEQ and the MRS groups. In the framework of the parton model, the proton contains two up quarks and a down quark. These are called valence quarks. In addition, since quark-antiquark pairs (including strong, charm, and bottom) can be created, additional quarks are present in the proton, and they are called sea quarks. Unlike the sea quarks, the valence quarks determine the quantum numbers of the proton exclusively. However DIS experiments have also shown that at high momentum transfer only about half of the proton momentum is carried by quarks, while the rest is carried by gluons, that are also part of the sea (photons do not interact with the neutral gluons and thus cannot probe their momentum directly). The proton parton densities show that the quark-gluon sea is dominant at small  $x$ , while at larger  $x$ , valence quarks have most of the momentum and thus little phase space is left for the sea quarks and gluons.

As a result of higher order contributions from perturbative QCD, when real gluon emission or virtual gluon exchange is included, scaling is violated and terms like  $\ln Q^2$  appear in the cross section and must be resummed (they produce soft and collinear singularities).

When looking at the scattering from the other end, i.e. from the products of the interaction, it is necessary to introduce the concepts of *jets* and *fragmentation* (or *hadronization*). The strong potential between two color objects, say a  $q\bar{q}$  pair, increases approximately linearly with the distance. This implies that the force between the color charges is constant (this is a consequence of gluon self interaction, i.e. the gluons exchanged between the pair also interact with each other *strengthening* the

color field as the particles are pulled apart) and thus the work necessary to pull apart the color charges increases with the distance. When the distance is large enough that it is energetically favorable to produce another  $q\bar{q}$  pair, the color string snaps and a  $q\bar{q}$  pair is generated. This leads to confinement. The  $q\bar{q}$  pairs then recombine to form color singlets and thus quarks or gluons cannot be observed in a free state. Instead, they produce a shower of hadrons called a jet, approximately collinear with the parton, which ultimately is detected in the experiment. This process is called fragmentation or hadronization as the quarks cannot be pulled further apart than about 1 fm without fragmenting into color singlet states. The fact that a quark carries color, while the fragments in the jet are all color singlets (otherwise they would not exist in a unbound state), raises a problem as it appears as if the color charge were not conserved. This is a non-perturbative problem currently impossible to solve, but basically the fact that the quark also interacts through color exchange with the spectator partons and other color fluxes in the event ensures that the color charge is conserved.

Analogously to the definition of PDF, in the case of fragmentation one defines fragmentation functions. These functions represent the probability for a certain parton to fragment into a hadron with a certain fraction of the parton energy. Fragmentation functions are not calculable perturbatively as hadron formation originates at long distances and is not perturbative (same as for PDF's).

At the Tevatron, high energy proton-antiproton collisions occur. The discussion carried out at the beginning of this section for DIS experiments, can be applied to hadron-hadron collisions. When proton and antiproton collide at high energy, the constituent partons of the proton have enough energy to *see* the partons in the antiproton and a hard scattering occurs. By convolving the cross section for the hard scattering process with the PDF's (and because of the factorization theorem which

guarantees that the long distance physics is universal, the same PDF's measured in DIS experiments for the proton can be used), the cross section for a generic interaction  $p\bar{p} \rightarrow C + X$ , where  $C$  and  $X$  are the final state particles, can be written as:

$$E_C \frac{d\sigma}{d^3p_C}(p\bar{p} \rightarrow C + X) = \sum_{abcd} \int dx_a dx_b dz_c G_{a/p}(x_a, \mu) G_{b/\bar{p}}(x_b, \mu) \quad (1.17)$$

$$\times D_{C/c}(z_c, \mu) \frac{\hat{s}}{z_c^2 \pi} \frac{d\hat{\sigma}}{d\hat{t}}(ab \rightarrow cd) \delta(\hat{s} + \hat{t} + \hat{u} - m_a^2 - m_b^2 - m_c^2 - m_d^2),$$

where  $x_i$  is the momentum fraction of the proton carried by parton  $i = a, b$ ,  $G_{a/p}(x_a, \mu)$  is the probability for parton  $a$  to be found with a fraction  $x_a$  of the proton momentum, and similarly  $G_{b/\bar{p}}(x_b, \mu)$  is the probability for parton  $b$  to be found with a fraction  $x_b$  of the antiproton momentum, and  $\hat{\sigma}$  is the partonic level cross section.  $\mu$  is the factorization scale of the process and should be chosen to be of the same order as relevant energy scales in the specific process.  $D_{C/c}(z_c, \mu)$  is the fragmentation function for particle  $C$  from parton  $c$  and  $z_c$  is the fraction of the parton energy carried by  $C$ . Finally,  $\hat{s}$ ,  $\hat{t}$  and  $\hat{u}$  are the Mandelstam variables for the hard scattering. The factorization is graphically illustrated in figure 1.2.

### 1.5.2 Standard Model Diphoton Production

In the introduction, it was mentioned that prompt diphoton production provides a tool to test the existence of large extra dimensions. In fact, a quantum field theory of gravity incorporates gravitons as the quanta of the gravitational field in the same way a quantum field theory of electromagnetism includes photons as quanta of the electromagnetic field. Gravitons couple to all particles (including themselves) and thus provide an additional mechanism to produce SM particles. In particular, through graviton mediated processes, fermion and vector bosons can be pair produced. These additional processes yield an enhancement of the number of pairs expected from SM sources alone. Diphoton production is a very promising search channel as photons



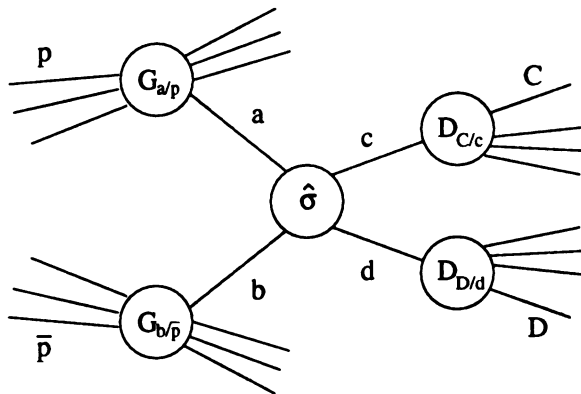


Figure 1.2: This picture schematically represents the factorization of the  $p\bar{p} \rightarrow C + X$  scattering into the parton distribution functions  $G$ , the cross section of the hard scattering  $\hat{\sigma}$  and the fragmentation functions  $D$ .

provide a clean signal at a hadron collider. This is true in part because photons are expected to be isolated, i.e. with no hadrons nearby, and thus can be efficiently distinguished from jets which make most of the background in this channel. Furthermore, the 4-momenta of a photon can be measured with very high resolution in the CDF electromagnetic calorimeter. Unlike photons, the measurement of jets relies on the definition of jet and on the worse hadron calorimeter resolution.

Diphotons are produced at the parton level via two main mechanisms:

- $q\bar{q} \rightarrow \gamma\gamma$
- $gg \rightarrow \gamma\gamma$

The tree level SM process  $q\bar{q} \rightarrow \gamma\gamma$  is the main contribution to the SM diphoton cross section. The loop-level process  $gg \rightarrow \gamma\gamma$ , although higher in order in the perturbation series, it is an important contribution to the diphoton cross section at low energies because of the large gluon parton distribution functions in this region. The Feynman

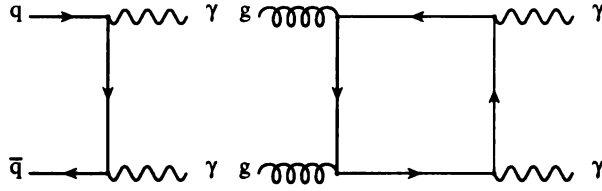


Figure 1.3: Representative Feynman diagrams for Standard Model diphoton production.

diagrams for these processes are displayed in figure 1.3.

The main background to diphoton production is jets fragmenting into  $\pi^0$  or  $\eta$  that carry most of the jet's energy and decay into multiple photons (the branching ratio for  $\pi^0 \rightarrow 2\gamma$  is almost 99% and for  $\eta \rightarrow 2\gamma$  is almost 72%). Although approximately one out of every one thousand jets pass the photon selection used in this analysis[5], jet production in hadron collision is overwhelmingly big (at leading order and with the same selection, the jet+ $\gamma$  production cross section is 3 orders of magnitude larger than the  $\gamma\gamma$  cross section and the dijet production cross section is almost 7 orders of magnitude larger; numbers from Pythia[22]) and thus generates a non negligible background. This is a result of a larger number of processes that produce jets compared to photons, larger color and spin factors and larger coupling for strong processes than for electromagnetic ones.

# Chapter 2

## Large Extra Dimensions

### 2.1 Introduction

Although the Standard Model has been successful in explaining a vast number of experimental results in particle physics and incorporating them into a theory, such a theory is not considered a fundamental theory for two reasons. In fact, it does not incorporate gravity and does not provide a viable explanation for the hierarchy between the electroweak scale and the Planck scale. The electroweak scale is the scale at which the symmetry between electromagnetism and the weak interaction is broken and the Planck scale is the scale at which all four forces, including the strong force and gravity, presumably have the same strength. The electroweak scale ( $M_{EW}$ ) is of the order of  $10^3$  GeV while the Planck scale ( $M_{Pl}$ ) is much higher,  $10^{19}$  GeV. No new physics is predicted between these two scales and thus this 16 order of magnitude gap is also known as the energy *desert*. The existence of such an enormous desert is not understood. In this framework, gravity is so weak compared to other forces because of the large discrepancy between the Planck scale and the electroweak scale.

Furthermore, loop corrections to the mass of the Higgs boson are proportional to a cut-off which could be as large as  $M_{Pl}$ . In order to have these corrections of the order of the weak scale, cancellations of the order of the Planck scale should occur.

This is an additional puzzle in the hierarchy problem.

In this chapter we will discuss the theory of Large Extra Dimensions (LED) by Arkani-Hamed, Dimopoulos, and Dvali [8] which among other theories tries to explain the seemingly large discrepancy between  $M_{Pl}$  and  $M_{EW}$ . We briefly mention that Supersymmetry (SUSY) has been the leading theory to solve the hierarchy problem. This is achieved by adding particles at the electroweak scale by assuming a symmetry between fermions and bosons and postulating the existence of boson superpartners for all fermions and fermion superpartners for all bosons. By doing so, SUSY predicts  $g_1$ ,  $g_2$ , and  $g_3$  to unify just below the Planck scale, while they fail to converge in the SM. And the superpartners provide the necessary cancellation of quadratic divergences in the computation of the Higgs mass.

## 2.2 Large Extra Dimensions

Extra dimensional theories date back to the 1920's, however only recently several extra dimensional theories have been formulated that have testable consequences at the TeV scale. In this dissertation we will focus on the model of low-scale quantum gravity incorporating large extra dimensions by Arkani-Hamed, Dimopoulos, and Dvali. This model in fact can be probed at current TeV scale colliders as it postulates that the electroweak scale is the only fundamental scale in nature. In this scenario, the Planck scale is lowered to values of the order of the weak scale and thus the hierarchy problem is simply removed. It was mentioned in the introduction that gravity appears so weak because the Planck scale is so large with respect to the electroweak scale. By lowering the Planck scale, the weakness of gravity is explained by adding finite spatial dimensions where only gravity can propagate while the other interactions are confined in the three infinite dimensions in which we live. How does the Planck scale become

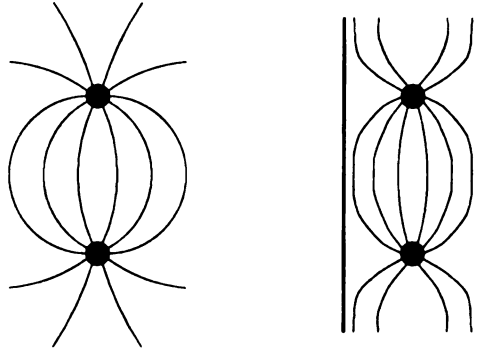


Figure 2.1: Schematic view of the effect of extra dimensions on field lines.

smaller by adding extra dimensions and why does gravity appear so much weaker compared to the other forces? Let us for the moment think in terms of electric fields and imagine the field created by two opposite electric charges. When the density of field lines is large, the force on a charged test particle going through that region of the field is larger than if the density of lines were smaller. Let us now imagine walls that surround both particles and assume that the walls repel the electric field (see figure 2.1). As the walls move closer to the charges, the field lines get closer and closer as the area in which the electric field propagates shrinks. This also implies that the strength of the field is increasing. We now generalize the electric field to include the electroweak and strong interactions but not gravity. In this picture, the walls represent the brane. Gravity does not *see* the walls and thus can propagate through them. As a result the Standard Model forces artificially appear much stronger than gravity despite the fact that originally all of their couplings were comparable. This discussion is summarized in equation 2.1, that relates the Planck scale in the extra dimensions ( $M_S$ ), the size of the extra dimensions ( $R$ ) and the Planck scale ( $M_{Pl}$ ) (Gauss' Law):

$$M_{Pl}^2 \approx M_S^{n+2} R^n, \quad (2.1)$$

where  $n$  is the number of extra dimensions. Equation 2.1 implies that the suppression of gravity is proportional to the volume in the extra dimensions. In other words, the smaller is the size of the extra dimension, the larger is  $M_S$ .

To preserve the validity of Newton's law which dictates that the gravitational potential falls as  $V(r) \propto 1/r$ , extra dimensions must be compactified. For distances  $r < R$  gravity can propagate in the extra dimension and thus it weakens (dilutes) faster as  $V(r) \propto 1/r^{n+1}$ . For one extra dimension, with  $M_{Pl} \sim 10^{19}\text{GeV}$ ,  $M_S \sim 10^3\text{GeV}$  and  $n=1$ , equation 2.1 yields  $R \sim 10^{13}$  m. This scenario is ruled out as such a large dimension would certainly have produced noticeable deviations from Newton's law at the scale of the solar system. For two extra dimensions,  $R$  is of the order of 1mm. Gravity has not been tested at submillimeter distances and thus compactified extra dimensions of this magnitude are not ruled out.

In Cavendish-type experiments[6], deviations from  $V(r) \propto 1/r$  at the mm scale are investigated. In addition, the strongest limits on two extra dimensions come from astrophysics [7]. As an example of these studies, extra dimensions would manifest in faster supernova cooling as stars would lose their energy faster by radiating gravitons in the extra dimensions. Astrophysics and Cavendish experiments have ruled out the existence of one or two extra dimensions. In this scenario  $n > 2$  is still an open possibility.

## 2.3 Kaluza-Klein Modes of Gravity

As discussed in section 2.2, the theory of large extra dimensions solves the hierarchy problem by introducing the concept that the Planck scale being so large is an artifact of the SM gauge bosons, quarks and leptons being confined in three spatial dimensions, known as the *3-brane*, while gravity can propagate in the  $3+n$  (the brane +  $n$  spatial

extra dimensions) dimensional space known as the *bulk*.

This model incorporates a low energy (effective) field theory of gravity in the bulk and thus the existence of the graviton. The graviton is the spin-2 tensor boson for gravity. The graviton has no gauge charges, is massless and couples to all the Standard Model particles as well as to itself.

Since the extra dimensions are compactified, the momentum must satisfy boundary conditions. As a result, the momentum along the extra dimension is quantized, i.e.:

$$p_4^k = \frac{2\pi k}{R}, \quad k = 0, 1, 2, \dots \quad (2.2)$$

where the subscript 4 refers to the extra dimension. The spacing between the levels is proportional to  $1/R$ , where  $R$  is the size of the extra dimension, hence the larger is the extra dimension, the closer are the levels. The momentum modes of excitation of the graviton transverse to the brane are perceived in the brane as different mass states. In fact, for the massless graviton in  $4+n$  dimensions, the square of the  $4+n$ -momentum is equal to zero:

$$p^2 = 0 \quad (2.3)$$

Since the space-like components acquire a minus sign in the Lorentz metric, we have:

$$p^2 = p_0^2 - p_1^2 - p_2^2 - p_3^2 - p_4^2 - \dots - p_{4+n}^2 = 0 \quad (2.4)$$

thus the 4-momentum square of the graviton in the brane,  $p_{brane}^2$ , is:

$$p_{brane}^2 = p_0^2 - p_1^2 - p_2^2 - p_3^2 = p_4^2 + \dots + p_{4+n}^2 = m_{brane}^2. \quad (2.5)$$

The right-hand side of this equation is a positive definite quantity and it looks like a mass. In other words, gravitons appear massive to an observer in the brane<sup>1</sup>.

---

<sup>1</sup>For extra time-like dimensions, since the metric dictates a positive sign for the time-like components of the  $4+n$ -momentum, the mass squared would go negative. As a result, extra time-like dimensions are not allowed.

Analogously to the momentum states, the spacing between mass states is proportional to  $1/R$ . This collection of mass states forms what is known as the Kaluza-Klein (KK) tower of gravitons. The tower can extend up to infinity, but there is a cut-off imposed by the fact that this is an effective theory and thus it breaks down at  $M_S$ .

Gravitons couple to the Energy-Momentum tensor. Examples of the coupling can be found by starting with the QED Lagrangian. Local gauge invariance of QED requires the existence of the spin 1 photon field. The interaction Lagrangian for QED can be written as:

$$\mathcal{L}_{QED} = eQ\bar{\psi} \not{A}\psi = eQ\bar{\psi}\gamma^\mu\psi A^\nu\eta_{\mu\nu}, \quad (2.6)$$

where  $eQ$  is the electric charge,  $\psi$  is the fermion field,  $A^\nu$  is the electromagnetic field vector and  $\eta_{\mu\nu}$  is the Lorentz metric:

$$\eta_{\mu\nu} = \begin{pmatrix} 1 & 0 & 0 & 0 \\ 0 & -1 & 0 & 0 \\ 0 & 0 & -1 & 0 \\ 0 & 0 & 0 & -1 \end{pmatrix}. \quad (2.7)$$

When adding  $4 + n$  dimensional gravity to the theory, one replaces  $\eta_{\mu\nu}$  with the spin 2 graviton tensor field  $g_{\mu\nu}$ :

$$g_{\mu\nu} = \eta_{\mu\nu} + \frac{h_{\mu\nu}}{M_S^{\frac{n}{2}+1}}, \quad (2.8)$$

( $h_{\mu\nu}$  is the fluctuation around the Lorentz metric) and multiplies  $\mathcal{L}_{QED}$  by  $\sqrt{-\det g_{\mu\nu}}$  (the minus sign comes from the choice of Lorentz metric) in order to have invariance under local coordinate transformations:

$$\begin{aligned} \mathcal{L}_{QED+Gravity} &= \sqrt{-\det g_{\mu\nu}}(eQ\bar{\psi}\gamma^\mu\psi A^\nu g_{\mu\nu}) = \\ &= (1 + c_1 g^2 + c_2 g^4 + \dots)(eQ\bar{\psi}\gamma^\mu\psi A^\nu g_{\mu\nu}), \end{aligned} \quad (2.9)$$



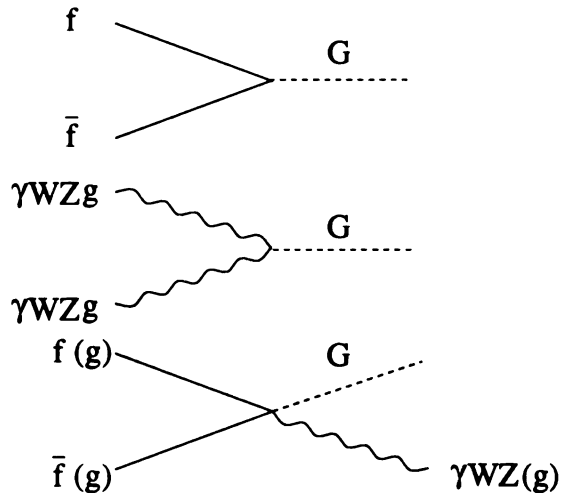


Figure 2.2: Representative graviton interaction vertices in linearized quantum gravity.

where in the last step the power series expansion for the square root was used. The  $g$ 's are products of elements in the graviton tensor with the indices contracted and the  $c_i$  are constants from the power series expansion. For energies small compared to  $M_S$ , only the first term is used. This is called the linear approximation. The term containing  $\eta_{\mu\nu}$  gives back QED, while the  $h_{\mu\nu}$  term includes the graviton coupling to fermion and boson fields. This discussion can be extended to the remaining interactions and thus gravitons can be attached to any SM vertex. Representative graviton vertices in the linear approximation are illustrated in figure 2.2. Beyond the linear approximation, vertices with more incoming gravitons occur. The strength of the interaction of any one of the KK gravitons with the particles confined in the brane is universal, i.e. it is the same for all the particles, and is proportional to  $1/M_{Pl}$ .

## 2.4 Probing Large Extra Dimensions at CDF

The existence of KK gravitons can be tested at colliders searching for two different processes: real graviton emission and virtual graviton exchange. At leading order, virtual graviton exchange includes processes in which a virtual graviton is produced by

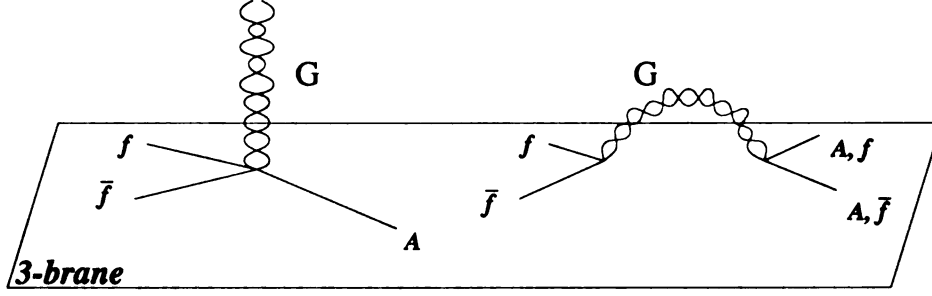


Figure 2.3: Examples of real graviton emission (left) and virtual graviton emission (right).  $f$  refers to the SM quarks and leptons and  $A$  are the SM gauge fields  $\gamma$ ,  $W$ ,  $Z$  or gluon.

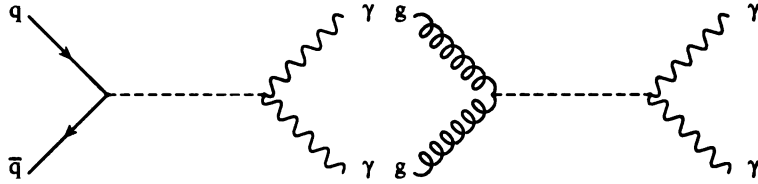


Figure 2.4: Feynman diagrams for LED diphoton production.

the annihilation of two SM particles in the initial state, the graviton then propagates in the extra dimension and finally decays into SM particles that appear in the brane. Real graviton production occurs when a graviton is produced together with something else by the interaction of SM particles and escapes in the extra dimensions leaving missing energy in the event as a flag. In figure 2.3 these two possible outcomes are illustrated.

In this dissertation, we investigate the existence of gravitons by looking at their decay into diphotons. At leading order, the differential cross section for  $p\bar{p} \rightarrow \gamma\gamma X$  in the presence of large extra dimensions can be written as [13]:

$$\begin{aligned}
 \frac{d^3\sigma}{dM_{\gamma\gamma}dydz} &= \left\{ \sum_q \frac{1}{48\pi s M_{\gamma\gamma}} f_q(x_1) f_{\bar{q}}(x_2) \right. \\
 &\times \left[ 2e^4 Q_q^4 \frac{1+z^2}{1-z^2} + 2\pi e^2 Q_q^2 M_{\gamma\gamma}^4 \eta (1+z^2) + \frac{\pi^2}{2} M_{\gamma\gamma}^8 \eta^2 (1-z^4) \right] \\
 &\left. + \frac{\pi}{256s} f_g(x_1) f_g(x_2) M_{\gamma\gamma}^7 \eta^2 (1+6z^2+z^4) \right\}. \quad (2.10)
 \end{aligned}$$

This expression includes the leading order Feynman diagrams for graviton mediated diphoton production, with  $q\bar{q}$  as well as  $gg$  in the initial states, shown in figure 2.4, the Standard Model  $q\bar{q}$  contribution to diphoton production discussed in section 1.5.2 and the interference between the  $q\bar{q}$  initiated SM and LED processes. However, the cross section for gluon initiated SM diphoton production is not included in this equation but is included in the Monte Carlo simulation used in the analysis. Finally, equation 2.10 does not incorporate the interference between the SM  $gg$  box diagram and the tree level  $gg$  graviton mediated diphoton production. Furthermore, this contribution is not simulated in the Monte Carlo used in this analysis as it is small compared to the direct KK terms[12].

In equation 2.10,  $M_{\gamma\gamma}$  is the invariant mass of the photon pair,  $y$  is the rapidity of the photon pair,  $z=\cos\theta^*$  is the cosine of the scattering angle in the center-of-mass frame of the hard scattering (photons),  $\sqrt{s}$  is the center-of-mass energy of the  $p\bar{p}$  collision,  $f_{q/g}(x_i)$  are the proton parton distribution functions, with  $x_{1,2} = (M_{\gamma\gamma}/\sqrt{s})\exp^{\pm y}$ ,  $eQ_q$  is the electric charge of quark  $q$ . Finally, graviton mediated processes introduce the  $\eta$  dependence in the equation.  $\eta = \lambda/M_S^4$  is the parameter that characterizes large extra dimensions:

- $M_S$ : this quantity has already been discussed earlier in this chapter and represents the Planck scale in the bulk.  $M_S$  should be of order 1 TeV.
- $\lambda$ : this parameter is dimensionless and its value is model dependent. In the convention we will adopt (Hewett [9]),  $\lambda = \pm 1$  is used. The different signs of  $\lambda$  allow for different signs of the interference between SM and LED graphs. More conventions are discussed in section 2.5.

Sometimes in the literature next-to-leading order QCD corrections are accounted for by multiplying equation 2.10 by a constant  $K$  factor of 1.3. In this work, we

use  $K=1$  as there is no clear reason why  $K=1.3$  should apply to graviton exchange processes. However, in order to compare our result to results from other experiments, limits with  $K=1.3$  will be quoted as well (see chapter 8).

By integrating over the  $y$  and the  $z$  dependence<sup>2</sup>, equation 2.10 can be written as:

$$\frac{d\sigma}{dM_{\gamma\gamma}} = \left. \frac{d\sigma}{dM_{\gamma\gamma}} \right|_{SM} + \eta \left. \frac{d\sigma}{dM_{\gamma\gamma}} \right|_{INT} + \eta^2 \left. \frac{d\sigma}{dM_{\gamma\gamma}} \right|_{KK}. \quad (2.11)$$

The first term on the right-hand side of equation 2.11 is the contribution from SM processes only. The second term, proportional to the first power of  $\eta$ , is the result of the interference between the SM processes and the LED processes. Finally, the last term, proportional to  $\eta^2$ , is the contribution coming from the direct Kaluza-Klein tower exchange.

A very important feature of the interference and direct KK cross sections is that their shapes are independent of  $\eta$ , which affects only the relative and absolute normalization. They only depend on PDF's and on the kinematics of the process. This property will be used in setting a limit (see chapter 6).

Since the LED contribution to diphoton production happens through a Kaluza-Klein tower of graviton states with a closely spaced mass spectrum, evidence for extra dimensions in the diphoton channel does not appear as a single resonance, but rather as an enhancement of the diphoton cross section at high invariant mass where the Standard Model contribution is rapidly falling. In fact, the spacing between the graviton mass states is proportional to  $1/R$  (see section 2.3), and since the mass states can be very light (of order keV for  $n=3$  and heavier for more extra dimensions), at high energies a large number of gravitons can be produced or, in other words, more modes of the momentum in the bulk can be excited. This behavior is reproduced in

---

<sup>2</sup>Since the graviton is a spin 2 object, graviton mediated processes modify the  $z$  distribution. The D0 collaboration searched for such an excess[14]. At CDF, however, it was concluded[15] that including  $z$  would give only a minimal improvement and thus in this analysis only a high mass excess will be investigated.

the mass spectrum for simulated SM+LED diphoton production with  $M_S=600$  GeV shown in figure 2.5. We observe that the SM mass spectrum is in fact very small in the high mass region where Direct KK processes become dominant. The fall off of the Direct KK distribution at high mass is an effect of the decreasing parton luminosities.

The invariant mass distributions for simulated SM + LED  $\gamma\gamma$  events in the case of constructive interference as well as destructive interference with  $M_S=600$  GeV are shown in figure 2.6. We observe that while for  $\lambda = -1$ , the SM+LED  $\gamma\gamma$  invariant mass distribution features an overall increase at high mass compared to the SM contribution alone, the destructive interference modifies the SM spectrum by adding what looks like a wide resonance. These are the kind of deviations from the Standard Model we will seek in this analysis.

The distributions in figures 2.5 and 2.6 are from Monte Carlo simulation of SM and LED diphoton production, including the simulation of the CDF detector and correspond to a choice of  $M_S = 600$  GeV, a value accessible with our experiment. As it was mentioned earlier in this section, the MC simulation does not incorporate the interference between the SM and LED  $gg$  initiated diphoton production mechanisms. The Monte Carlo samples will be discussed more in detail in chapter 6.

The search for large extra dimensions has been also pursued at CDF in the dielectron channel, which, analogously to the diphoton channel, offers a clean signal with small SM background making it easier to detect an excess. The diphoton and dielectron analysis have been combined to improve the reach of this search. This will be discussed in chapter 8. Jet production, however, is very large in a hadron collider and it is expected to be very difficult to extract signals of new physics.

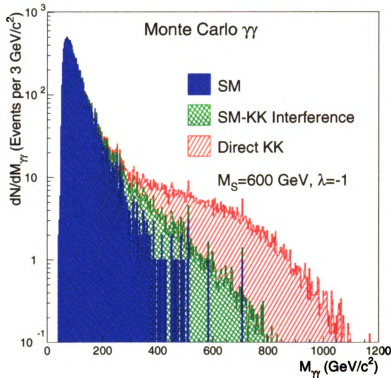


Figure 2.5: Invariant mass distribution of SM and SM+LED  $\gamma\gamma$  events. LED events are simulated with  $M_{S,Hewett}=600$  GeV and  $\lambda=-1$ .

## 2.5 Conventions

There are several notations to express the Planck scale in the extra dimensions. The most common ones are the Hewett convention [9], the Giudice, Rattazzi and Wells notation (GRW) [10], and finally the Han, Lykken and Zhang convention (HLZ) [11]. The  $\eta$  parameter characterizes the strength of the graviton interaction and is the same in all conventions. It can be expressed as:

$$\eta = \frac{\lambda}{M_S^4}, \quad (2.12)$$

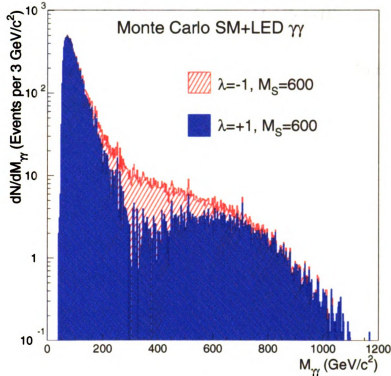


Figure 2.6: Invariant mass distribution of SM+LED  $\gamma\gamma$  events in case of destructive ( $\lambda=+1$ ) and constructive ( $\lambda=-1$ ) interference for  $M_S = 600$  GeV.

where  $\lambda$  is a parameter of order one whose value and sign is convention dependent and  $M_S$  is the Planck scale in the extra dimensions. In Hewett convention, the sign of  $\lambda$  is not fixed and thus the sign of the interference can be either positive or negative. The magnitude of  $\lambda$  is of order one and for numerical calculations  $\lambda = \pm 1$  is used. In GRW convention, the sign of  $\lambda$  is fixed. In HLZ notation,  $\lambda$  depends on the number of extra dimensions  $n$  and its sign is fixed. Hewett's convention has been adopted throughout this thesis. To translate results from Hewett's convention to GRW notation one simply multiplies  $M_S(\text{Hewett})$  by a geometric factor:

$$M_S(\text{GRW}) = \sqrt[4]{\frac{\pi}{2}} M_S(\text{Hewett}). \quad (2.13)$$

HLZ notation explicitly incorporates the  $n$  dependence in  $\lambda$ , and thus ( $n > 2$ ):

$$M_S(HLZ) = \sqrt[4]{\frac{2}{n-2}} \times \frac{\pi}{2} M_S(Hewett) \quad (2.14)$$

The  $n$  dependence arises in the geometrical factor because of different assumptions about the topology of the extra dimensions.



# Chapter 3

## The CDF Detector

The Collider Detector at Fermilab (CDF) is located at the Fermilab Tevatron in Batavia, Illinois. Its purpose is to detect particles resulting from the  $p\bar{p}$  collisions at a center-of-mass energy of 1.8 TeV.

The detector consists of different layers of sensitive material arranged along the Tevatron beam pipe to cover as much of the solid angle around the interaction point as possible. This chapter is meant as a brief overview of the CDF detector. A more detailed description of the detector can be found in [16]. The CDF detector has been recently upgraded for Run II.

### 3.1 The Tevatron

The Tevatron is a  $p\bar{p}$  collider. The protons and the antiprotons move in opposite directions around a circular orbit of 2 km in diameter. By the time the protons are injected into the Tevatron, they have gone through various stages of acceleration (see figure 3.1). The protons in the form of hydrogen gas are initially contained inside a bottle. The negative hydrogen ions contained in the gas are extracted and accelerated in a Cockroft-Walton electrostatic generator to an energy of 75 KeV. The ions are then further accelerated to 400 MeV in a linear accelerator (LINAC) containing RF

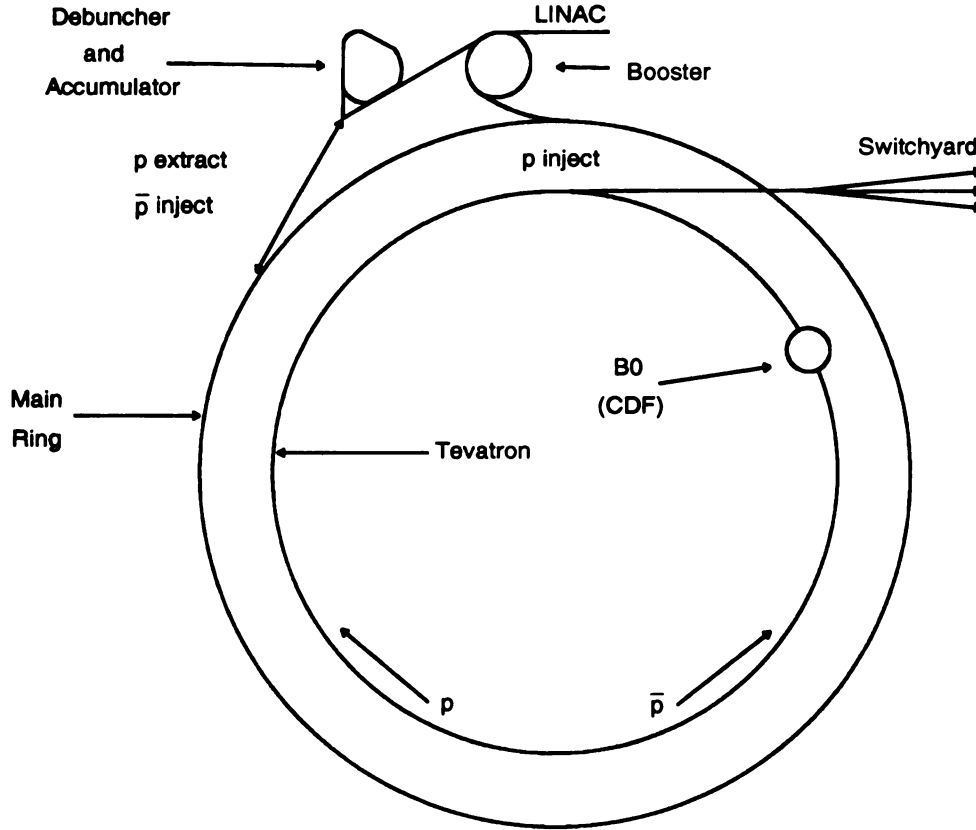


Figure 3.1: Schematic view of the Fermilab Tevatron and the different stages of acceleration for the protons and the antiprotons.

cavities. The next stage of acceleration is through a proton synchrotron (Booster), where the ions go through a carbon foil that strips them of their electrons. The resulting protons are collected in bunches and accelerated to 8 GeV. At this point the protons are injected into the Main Ring. This is a proton synchrotron 2 Km in diameter. The Main Ring serves two purposes. It accelerates a fraction of the protons to 150 GeV and injects them into the Tevatron. Another fraction of the protons are extracted to generate antiprotons when they reach an energy of 120 GeV. Once they exit the Main Ring, they are directed into a nickel-copper target. Among the products of this interactions there are antiprotons. The antiprotons are focused by

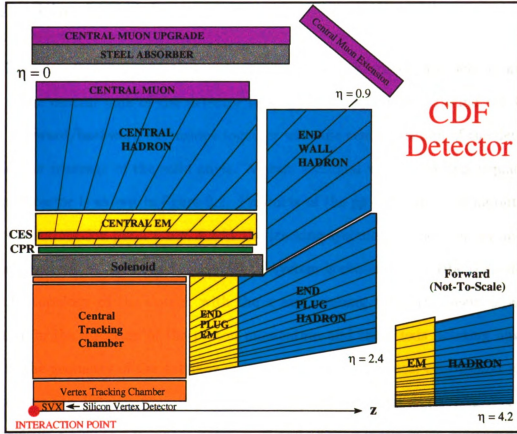


Figure 3.2: Cross section of an upper quarter of the CDF detector.

the means of a lithium lens and sent to a debuncher to reduce the momentum spread of the beam and to combine the bunches. Once this is achieved, the antiprotons are stored in the Accumulator ring, located in the same enclosure as the debuncher, until enough antiprotons are collected (this process is known as “stacking”). Antiprotons are stacked over a period of several hours. When enough antiprotons are collected, the antiprotons are injected in the main ring where they are accelerated to 150 GeV. Both proton and antiproton beams are injected into the Tevatron. The Tevatron is a proton-antiproton synchrotron that lies beneath the Main Ring and has the same diameter. Here the beams are accelerated to 900 GeV. When this energy is reached, the beams are deflected so that they collide in specific points around the accelerator circumference where the D0 and CDF detectors are located.

## 3.2 The CDF Detector

The CDF detector weighs 5000 t and is approximately 30 meters long and 10 meters wide. The central bulk of the detector is cylindrically symmetric around the beam pipe. Forward/backward extensions together with the central section of the detector provide  $4\pi$  coverage of the solid angle. A cross sectional view of an upper quadrant of the detector is shown in figure 3.2. Products of the  $p\bar{p}$  collisions moving outward from the interaction point travel across the tracking systems, the calorimetry and the muon detectors. A right-handed coordinate system is chosen to describe the detector and the topology of the events, with the  $z$  axis running along the beam pipe and pointing in the direction of the proton momentum and the  $y$  axis pointing upward. Due to the geometry of the detector, it is natural to use spherical coordinates  $r, \theta, \phi$ .  $r$  expresses the distance from the origin of the system,  $\theta$  is the angle measured from the positive  $z$  axis and it ranges between  $0^\circ$  and  $180^\circ$ .  $\phi$  is the angle measured from the positive  $x$  axis and it ranges between  $0^\circ$  and  $360^\circ$ .

In addition to these coordinates, it is common to use the rapidity defined as:

$$y = \frac{1}{2} \ln \frac{E + p_z}{E - p_z} \quad (3.1)$$

For boosts along the direction of the  $z$  axis the rapidity transforms as  $y \rightarrow y + \tanh^{-1} \beta$ , where  $\beta$  is the velocity of the boost with respect to the lab frame, and thus differences in rapidity are Lorentz invariant. As a result, the shape of the rapidity distribution  $dN/dy$ , where  $N$  is the number of particles per unit volume, is Lorentz invariant.

In the relativistic limit, the rapidity approaches the limit:

$$\eta = -\ln \tan \frac{\theta}{2} \quad (3.2)$$

This quantity is called pseudorapidity and is often used to describe the angular dis-

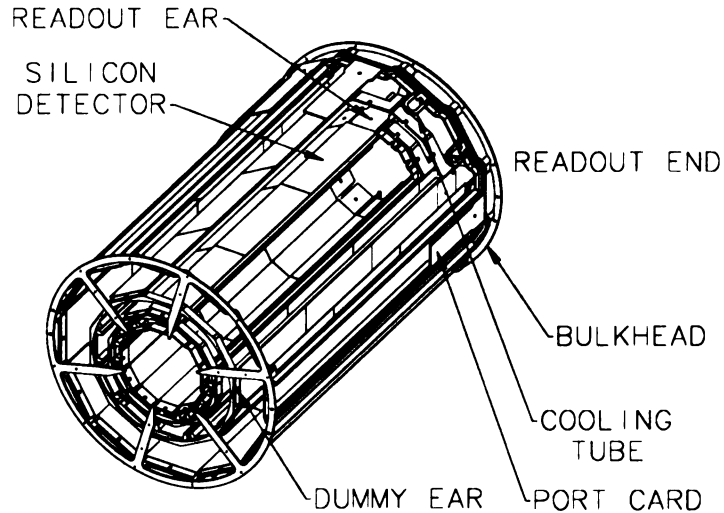


Figure 3.3: Isometric view of one of the SVX barrels.

tribution of particles in a collider detector.

### 3.3 The Tracking System

The tracking system is contained in a uniform 1.4 T magnetic field generated by a superconducting solenoidal coil located just outside the Central Tracking Chamber (CTC).

#### 3.3.1 The SVX

Moving outward from the beam pipe, the first component of the detector we meet is the Silicon Vertex Detector (SVX). The SVX consists of two barrels with an active length of 51 cm (see figure 3.3) and covers a region of pseudorapidity  $|\eta| < 1.9$  (for interactions occurring at  $z = 0$ ). Since the spread of the  $z$  coordinate of the interaction vertices is gaussian in shape around  $z = 0$  with  $\sigma \simeq 30$  cm, only approximately 60% of the  $p\bar{p}$  interaction vertices are in the fiducial volume of the SVX.

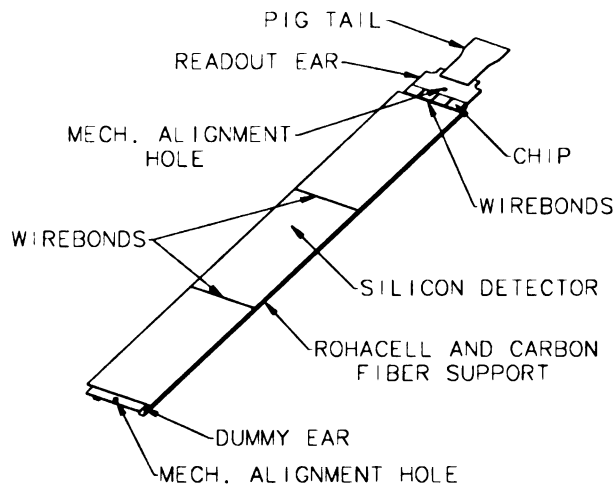


Figure 3.4: SVX ladder.

The two barrels are coaxial around the beam pipe and have a gap between them of 2.15 cm at  $z = 0$ . Each barrel is 25.5 cm long and consists of twelve wedges. Each wedge subtends a  $30^\circ$  angle in azimuth and it contains four layers of silicon strips. The layers run parallel to the beam line. Each layer contains 12 closely spaced silicon microstrips known as *ladders*. Each ladder (figure 3.4) consists of three 8.5 cm long sections. The silicon stripes are interspaced with conducting strips.

When charged particles travel through the SVX, electrons in the semiconductor are excited to the conduction band. Due to a voltage drop between the extremities of the strips, the charges are collected and the current they generated is measured. The SVX provides track measurement in the  $r - \phi$  plane with a resolution of  $\simeq 15\mu\text{m}$ .

### 3.3.2 The VTX

The VTX (Vertex Time Projection Chamber) is a gas drift chamber built around the SVX. The outer radius of the VTX is 22 cm and it covers  $|\eta| < 3.5$ . It consists of 28 separate modules connected end-to-end and parallel to the beam direction, and each 10 cm long. Each of the modules is divided into eight wedges (see figure 3.5), each covering an azimuthal angle of  $45^\circ$ . Each wedge contains in its middle a high

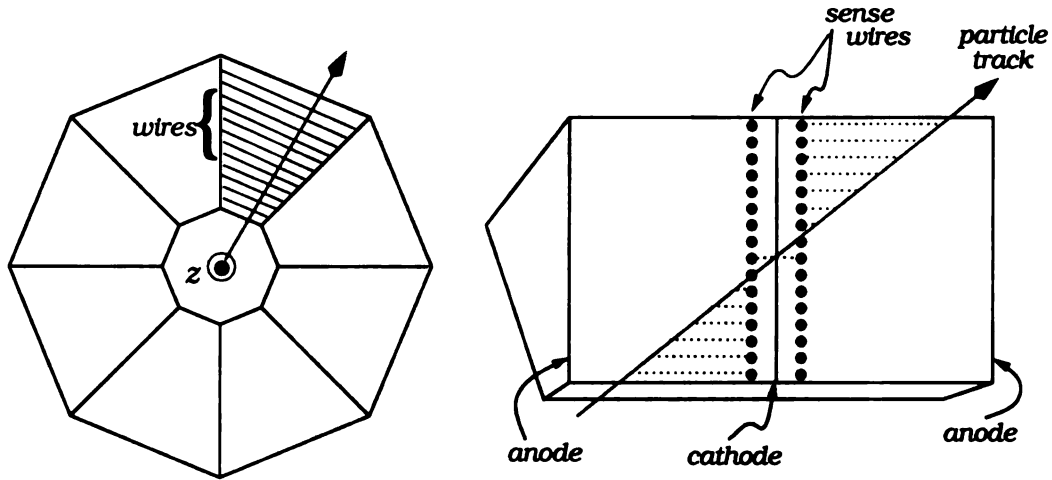


Figure 3.5: Cross sectional view of the VTX (left) and schematic view of one wedge (right).

voltage grid laying on a plane perpendicular to the beam line. On each side of the grid, each wedge contains sense wires running perpendicularly to the beam direction. The chamber is filled with a argon-ethane gas mixture.

Charged particles traveling through the VTX ionize the gas, thus generating a current of charged particles collected at the wires. The drift times plus the  $r$  coordinate of the wire that was hit provide two-dimensional measurement of a track in the  $r, z$  plane. Furthermore, by extrapolating the reconstructed tracks to the beam direction, the VTX provides a measurement of the  $z$  of the vertex with a resolution of 1-2 mm.

### 3.3.3 The CTC

The Central Tracking Chamber is a cylindrically symmetric drift chamber that covers the central region of the detector. It is 3.2 m long with a radius of 1.3 m. 3-D tracks of charged particles passing through it can be reconstructed with a very precise measurement of their transverse momentum. The sign of the charge can be deduced from the curvature of the track. The momentum resolution in the region  $|\eta| < 1$  is

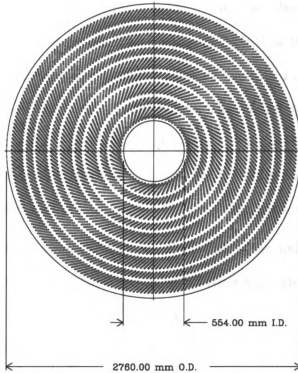


Figure 3.6: Transverse view of the CTC. The superlayers and the tilted cells are shown.

$\delta p_T/p_T^2 \leq 0.002 \text{ (GeV}/c)^{-1}$ . The spatial resolution is 2.5 mm in the axial direction and 200  $\mu\text{m}$  in the azimuthal direction.

The design of the CTC consists of drift cells containing sense wires. The cells are arranged in 84 layers grouped in nine superlayers. There are five axial superlayers alternated with four stereo superlayers. The axial superlayers have cells running parallel to the beam pipe and provide precision measurement of the track in the  $r - \phi$  plane, while the stereo superlayers consist of cells tilted by  $\pm 3^\circ$  with respect to the beam pipe thus providing tracking information in the  $r - z$  plane. Each of the axial cells contains 12 sense wires and each of the stereo cells contains 6 sense wires. The sense wires are alternated with potential wires that control the gas gain on the sense wires. At the borders of each cell, on each side of the sense wires, there are field wires whose purpose is to regulate the strength of the drift field. The field



wires together with the potential wires provide a constant electric field in the drift region of 1350 V/cm inside each cell. The maximum drift time is 800 ns. An electron drifting inside a cell in the argon/ethane gas mixture contained in the chamber in the presence of the crossed electric and magnetic field has a Lorentz angle of  $45^\circ$  with respect to the electric field. In order to compensate for this so that the drift direction is perpendicular to the radial direction the cells are tilted by  $45^\circ$  which ensures that the charged particle will go near at least one of the sense wires (see figure 3.6).

A charged particle traveling through the CTC follows an helical track because of the magnetic field. Tracks are reconstructed by a fitting algorithm that takes the hits in the CTC and fits them to an arc of an helix.

### 3.4 The Central Preradiator

The Central Preradiator (CPR) is a multi-wire proportional drift chamber located right outside the magnet. It measures tracks of charged particles that result from photon conversions in the inner detector. A single high energy photon has a lower probability to convert into an electron-positron pair inside the magnet than the two photons resulting from a decay. The CPR measures the charge that is generated by the crossing of charged particles. This information can be matched to an electromagnetic cluster. It is also used to distinguish  $\gamma \rightarrow e^+e^-$  from single electrons or positrons in the electromagnetic calorimeter.

### 3.5 The Calorimeters

The calorimetry of CDF is located outside the magnet. According to the region of space that it covers, it is divided into 3 different components: central, plug and forward. The central calorimeter covers  $|\eta| < 1.1$ , the plug  $1.1 < |\eta| < 2.4$  and the

forward  
follow  
shown

**3.5.**

The  
with  
segme  
into C  
geom

E.  
toget  
is deg  
happ  
energ  
pair.  
proce  
the ei  
energ

W  
and l  
multi  
curren  
of col  
scintil  
the ca

forward  $2.4 < |\eta| < 4.2$ . Each component consists of an electromagnetic (EM) section followed by a hadronic (HAD) section. The segmentation of the calorimeters is shown in figure 3.7.

### 3.5.1 Central and End Wall Hadron Calorimeter

The central calorimeter is a sampling device with layers of scintillator alternated with sheets of absorbing material. It covers a pseudorapidity region up to 1.1. It is segmented in  $\eta, \phi$  towers. There are 24  $15^\circ$  wedges in  $\phi$  and each wedge is segmented into 0.1  $\eta$  towers. The towers all point back to the nominal interaction point. This geometry is known as projective tower geometry.

Each tower in the EM section consists of layers of scintillating material stacked together with layers of absorbing lead. The energy of electrons passing through matter is degraded via different processes. An important process is bremsstrahlung. This happens when the electron interacts with the nuclei in the material and emits a high energy photon. The photon in the presence of nuclei converts into an electron-positron pair. The electrons and positron in turn emit photons through bremsstrahlung. This process continues, generating an electromagnetic shower. The cascade is halted when the electron (positron) energy falls below a critical energy at which point the primary energy loss mechanism is through atomic collisions.

When the shower crosses the scintillator, the atoms and molecules are excited and light is emitted. Light is collected in wavelength shifters and directed to photomultiplier tubes that collect the light and turn it into photoelectrons. The electric current measured at the output of the photomultiplier is proportional to the number of collected photons and thus provides a measurement of the energy released in the scintillator. An average EM shower is almost entirely contained in the EM section of the calorimeter.

Embedded in the EM section are strip chambers (CES) that provide a high resolution measurement of the shower profile in  $z$  and  $r - \phi$ . The CES is a argon-ethane gas proportional chamber located at a depth where the average shower development reaches its maximum. It consists of anode wires running parallel to the beam direction and cathode strips perpendicular to the beam direction (see figure 3.8). A neutral meson decaying into multiple photons can fake the signature of direct photons produced in the hard scattering. The CES provides a tool to differentiate between these two instances by measuring the transverse width of the shower at shower max. This is then compared to the shower width of a typical test beam electron. The shower generated from a  $\pi^0$  decaying into two photons is in average wider than a shower generated by a direct photon. This method is efficient for photons up to an energy of 35 GeV. Above this energy it becomes more difficult because the photons coming from a decay are boosted to a smaller angular separation and thus more difficult to resolve. The CES provides a measurement of the shower position with a resolution of 2 mm.

The hadronic section (CHA) is larger than the EM and it consists of layers of scintillating tiles alternated with sheets of absorbing steel. Every tower in the HAD section matches a tower in the EM section. The WHA (End Wall Hadron) follows the CHA for  $30^\circ < \theta < 45^\circ$  and  $135^\circ < \theta < 150^\circ$ . It is built in a similar fashion to the CHA, but it has thicker layers of absorbing steel as the particles passing through it have higher energies corresponding to the same  $E_T$ .

The resolution of the EM section is  $13.5\%/\sqrt{E_T} \oplus 1.7\%$ . The resolution of the HAD section is  $75\%/\sqrt{E_T} \oplus 3\%$ , which is considerably worse. The worse resolution is due both to the coarser longitudinal segmentation of the hadronic calorimeters and the larger fluctuations intrinsic to hadronic showers.

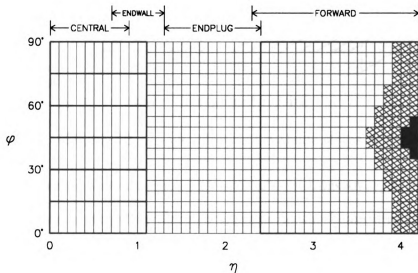


Figure 3.7:  $\eta, \phi$  segmentation of central, plug, end wall and forward calorimeters.

### 3.5.2 Plug Calorimeter

The plug calorimeter used in CDF for Run I was a sampling device with layers of gas proportional tubes interleaved with sheets of absorbing material (lead for the EM section and steel for the HAD section). It was concluded that using the design of the central calorimeter, i.e. scintillator as the active material, would create too many dead spaces/hot regions because of the need to accommodate the light guides necessary to read out the light produced in the scintillator.

Each plug is divided into four quadrants, each  $90^\circ$  in  $\phi$ . Each EM quadrant contains 34 layers. Each layer contains a layer of proportional tubes and a sheet of lead 2.7 mm thick. The proportional tubes have a 7 mm  $\times$  7 mm square cross section.

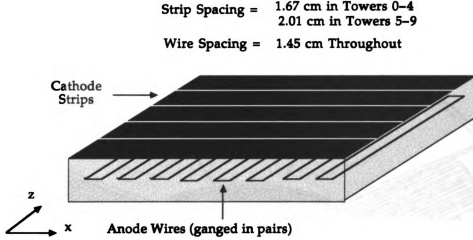


Figure 3.8: Anode wires and cathode strips in the CES.

A wire is strung inside each tube and each tube contains an argon/ethane gas mixture. The tubes are arranged in planes transverse to the beam direction. Each plane of tubes is matched with a plane of cathode pads that are etched in such a way as to reproduce the tower geometry (see figure 3.9). Deep inside the EM calorimeter, at the shower max position, there is a finer segmentation of strips in  $\eta$  and  $\phi$  that provide a more precise measurement of the development of the shower and can distinguish between low energy electrons, low energy photons or a  $\pi^0$  decay into two photons from a high energy hadronic jet. The strips cover up to  $|\eta|=1.84$ .

The hadronic section of the plug is designed in much the same way, but with no strips and with 20 layers of proportional tubes (see figure 3.10) and steel. The layers of absorber are 5.1 cm thick. The plug calorimeter is segmented into  $0.1 \times 5^\circ$  in  $\Delta\eta, \Delta\phi$ .

The resolution of the EM section is  $28\%/\sqrt{E_T} \oplus 2\%$ . The resolution of the HAD section is  $130\%/\sqrt{E_T} \oplus 4\%$ .

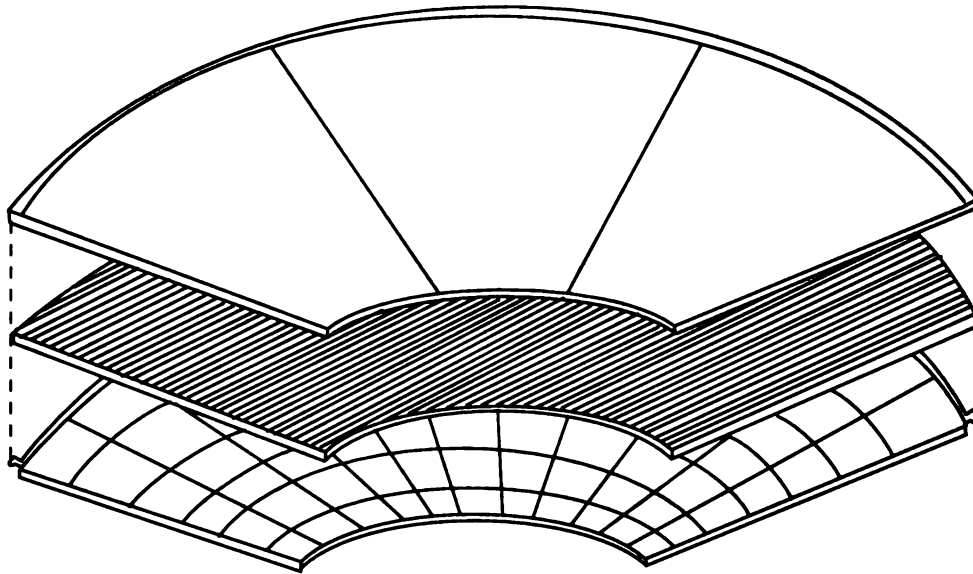


Figure 3.9: Absorber sheet, proportional tubes, and cathode pads in one layer of the PEM.

### 3.5.3 Forward Calorimeter

The forward/backward calorimeters are located around the beam pipe just behind the plugs. Similar to the plugs, they consist of layers of proportional tubes alternating with layers of absorbing material and have the same projective tower geometry incorporated in the rest of the CDF calorimetry ( $0.1 \times 5^\circ$  segmentation in  $\eta, \phi$  and pointing back to the nominal interaction point).

The resolution of the EM section is  $25\%/\sqrt{E_T} \oplus 2\%$ . The resolution of the HAD section is  $130\%/\sqrt{E_T} \oplus 4\%$ .

## 3.6 The Muon Chambers

Muons are more penetrating than electrons. For this reason, the muon chambers are the last components of the detector, farthest away from the beam pipe. The inner

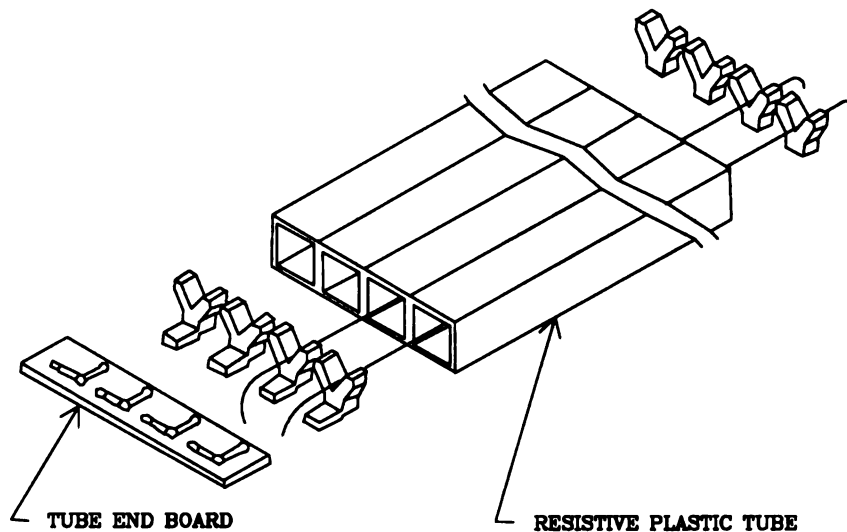


Figure 3.10: Proportional tubes in the PHA.

layers of the detector act as an absorber for particles other than muons (and for low energy muons).

The Muon detector consists of three sections: CMU (Central Muon Chamber), the CMP (Central Muon Upgrade) and the CMX (Central Muon Extension). The CMU and the CMP cover a pseudorapidity region  $|\eta| < 0.6$  and the CMX covers  $0.6 < |\eta| < 1$ . The CMU and CMP consist of single wire proportional drift chambers that are parallel to the beam direction and are filled with an argon/ethane gas mixture. The CMP also contains a layer of 0.6 m thick steel absorber to reduce the hadronic background. The tubes are arranged in modules of  $4 \times 4$  single wire cells that cover  $12.6^\circ$  in  $\phi$  above each wedge of the central hadron calorimeter, leaving  $2.4^\circ$  per wedge non instrumented (see figure 3.11). The track (stub) of the muon is measured in the  $r - \phi$  plane and in the  $r - z$  plane.

The CMX extends the coverage of the muon chambers. It consists of four arches. Each arch is composed of drift chambers similar to the CMU and CMP, but the cham-



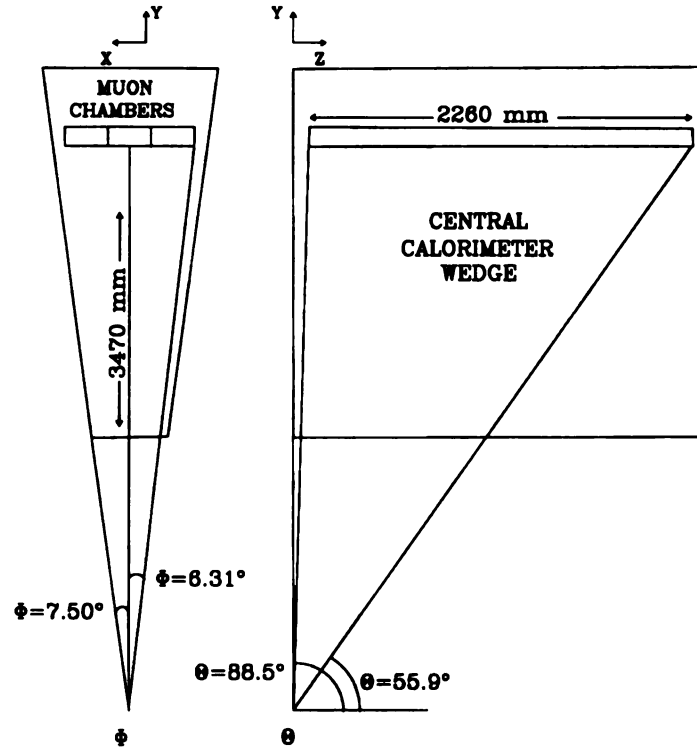


Figure 3.11: Location of the CMU modules with respect to the central calorimeter.

bers are sandwiched in between layers of scintillator that provide trigger information and help to reject background.

### 3.7 Beam-Beam Counters

The beam-beam counters are located in front of the forward-backward calorimeters at approximately 6 m on each side of the interaction point. Each counter consists of a set of scintillating counters arranged around the beam line and covering  $3.24 < |\eta| < 5.90$ . When at least one of the counters in each plane is hit in within a time window of 15 ns of a bunch crossing, the minimum bias trigger is activated. This means that during the bunch crossing there has been at least one interaction. Also, the BBC counters provide a measurement of the instantaneous luminosity.

## 3.8 The Trigger

At the B0 interaction point, there are more than 200000 interactions per second. Most of these interactions produce events that are not especially interesting from a physics point of view. In order to minimize the loss of events due to dead time, and to select events that are potentially more interesting, a trigger system has been implemented at CDF. The trigger system consists of three levels. The decision time of the level one trigger is quite short as it has to fit in the time interval between bunch crossings ( $3.5\mu\text{s}$ ). After the events are processed and have passed the level one requirements, they are sent to the level two trigger. Here the decision time is approximately  $25\mu\text{s}$ . Only a small percentage of events are sent to level 2, resulting in a small dead time. The events that survive this further and more sophisticated selection, are fully read out and promoted to the level 3 trigger. Here a simplified version of the offline analysis software is used, i.e. rough tracking reconstruction and clustering are included. The events that pass level 3 are written to tape and saved for offline physics analyses.

Some triggers are prescaled. This means that not all of the events passing a trigger requirement are promoted to the next level. This is done to minimize the dead time.

# Chapter 4

## The Event Data Sample

### 4.1 Introduction

The event data sample used in the diphoton search for Large Extra Dimensions at CDF consists of events with inclusive diphotons in the final state. In this chapter we will describe the tools used to extract diphoton events from the enormous amount of data collected by CDF in approximately 4 years during CDF Run I (1992-1996). The final data set consists of 479 events. These events are comprised of two distinct subsets, corresponding to two different topologies. One of the subsets, the Central-Central (or CC) diphoton sample, consists of events with both photons in the central region of the detector, while the other, the Central-Plug (or CP) diphoton sample, includes events with at least one central electromagnetic cluster and at least one cluster in the end-plug electromagnetic calorimeter.

The Central-Central diphoton sample will be briefly described as it has been used in previous analyses, while the Central-Plug diphoton sample is my main contribution to the search.

## 4.2 Cluster

A photon is detected by CDF as a cluster of towers localized in the electromagnetic section of the calorimeter with no tracks associated with it. A cluster is defined as a collection of calorimeter towers in which energy is deposited by particles traveling through it. A cluster is reconstructed by an algorithm that loops through all the towers and selects those towers where at least 3 GeV of transverse energy is deposited. These towers are called *seed towers*. Towers adjacent to the seed towers along  $z$  are added to the seed tower to form a cluster if at least 100 MeV of transverse energy is deposited into them. Seed towers cannot be shared among clusters. At this stage different steps are taken according to whether the clusters are in the central or in the end-plug calorimeter. For clusters in the central calorimeter, a maximum of 3 towers, adjacent in  $\eta$ , can be grouped into a cluster. For plug clusters however the cluster stretches both in  $\eta$  and  $\phi$  and can grow to include up to 25 towers or until an energy valley (i.e. towers below the 100 MeV threshold) is reached.

An adoption of different clustering algorithms according to the pseudorapidity of the particle is justified by the fact that, for higher values of  $\eta$ , the size of the towers becomes smaller. As a result, in order to faithfully represent the same energy deposition, more towers must be included in the cluster if the deposition occurs in the plug rather than in the central calorimeter, where towers are larger and hence clusters do not cover more than three towers.

## 4.3 The Central-Central Diphoton Event Sample

There are 287 events in the CC diphoton sample. These events have passed online and offline selections. The online selection occurs at the trigger level during data taking. Offline, the complete reconstruction code is employed and thus more severe

constraints can be applied to extract the events of interest. In this section we will describe both stages of the selection for the CC diphoton sample.

### 4.3.1 Global Selection

First, the events are required to pass the online trigger selection (see section 3.8). The trigger requisite for the Central-Central diphoton sample was to have at least two clusters in the event in the central region of the detector. Each cluster must have  $E_T > 16$  GeV. Isolation is not a requirement. The events that pass the trigger selection are written to tape along with the information coming from all the detector components. Once the events are written to tape, the information contained in them is extracted in the form of variables representing the signature left in the detector by the particles that crossed it. This information includes, for instance, the number of clusters per event, cluster energies, etc. The offline selection consists of a set of constraints on these variables. A fraction of these variables refers to general properties of the events that are not specific to any physics object. These include the quality of the data taking process, the out-of-time energy, and the vertex selection.

Only events contained in good runs are selected. In the CDF jargon, a good run refers to a run during which all detector systems were functioning and online.

The out-of-time energy is measured in the calorimeter towers<sup>1</sup> when the time interval between the nominal interaction time  $t_0$  and the time  $t$  the energy is deposited in the calorimeter is outside a time interval of  $-20 \text{ ns} < t - t_0 < 35 \text{ ns}$ . The total  $E_T$  out-of-time is required to be equal to zero in order to remove background from cosmic rays that occur at random times.

The vertex of the interaction is measured by extrapolating the event tracks to the

---

<sup>1</sup>Timing information associated with the energy deposition is available for the towers in the central hadronic calorimeter.

beam line. The  $z$  coordinate of the vertex has a gaussian spread about the nominal interaction point at  $z = 0$  with  $\sigma=30$  cm. The projective tower geometry is not satisfied outside  $|z_{\text{vertex}}| < 60$  cm and hence only events whose vertex fulfills the requirement  $|z_{\text{vertex}}| < 60$  cm are accepted. Furthermore, the vertex of the interaction is ranked according to the number of hits used to fit the tracks. Only events with the higher classes are accepted.

### 4.3.2 Photon Identification

Additional criteria are employed with the specific purpose of singling out events with two direct photons in the final state. Direct or prompt photons are produced in the hard scattering as opposed to soft (low energy) photons that are the byproduct of jets.

Each event is required to have at least two central electromagnetic clusters, i.e. the pseudorapidity of each of the clusters is  $|\eta| < 1$ . Each cluster is required to have  $E_T > 22$  GeV. For these clusters the trigger efficiency is 100%. For energies closer to the trigger threshold (16 GeV in this case) events are lost for inefficiencies of the trigger even though the energy of the cluster is above the threshold. In addition, the photon candidates are required to be in the fiducial region of the detector. Certain regions of the detector are not instrumented and there is a gap at  $z = 0$  where the two halves of the central calorimeter meet. These regions are excluded.

Further fiducial cuts ensure that the cluster is in the active region of the CEM. We require:

$$|X_{\text{wire}}| < 21\text{cm}, \quad (4.1)$$

where  $X_{\text{wire}}$  is the  $x$  coordinate in the CES coordinate system, that is the weighted

mean of the energy deposition in the CES wires; also:

$$14 < |Z_{\text{strip}}| < 217\text{cm}, \quad (4.2)$$

where  $Z_{\text{strip}}$  represents the weighted mean of the energy deposited by the cluster in the CES strips.

The longitudinal shower development has been extensively studied for test beam electrons. However there was not a photon test beam, thus the results for the electrons are applied to the photons as well. Electrons have the tendency to begin to shower earlier than the photons, but this distinction is negligible for our purposes. This knowledge is used in the photon selection by comparing the shower profiles of the photon candidates collected by CDF to the profiles from the test beam electron study. An average  $\chi^2$  is computed to quantify the differences in energy deposition between electrons and photons both in the  $z$  view ( $\chi_{\text{Wire}}^2$ ) and in the  $r - \phi$  view ( $\chi_{\text{Strip}}^2$ ). The following condition must be satisfied for photons:

$$\chi_{\text{Avg}}^2 = \frac{\chi_{\text{Strip}}^2 + \chi_{\text{Wire}}^2}{2} < 20 \quad (4.3)$$

Furthermore the energy of the cluster measured in the CES (pulse height) is compared to the inferred CES energy from the CEM energy measurement and vertex position. The expected and the measured value are required to be consistent, i.e. in within  $2\sigma$  from each other:

$$|\sigma_{\text{CES Pulse Height}}| < 2 \quad (4.4)$$

Photons deposit most of their energy in the EM section of the calorimeter, unlike jets, which are more likely to deposit their energy in the hadronic partition and whose constituent hadrons begin their shower later in the detector than photons. This important feature is employed as an additional tool to discriminate photons

from jets by requiring that the potential photon cluster has a large fraction of its total energy deposited in the EM section rather than in the hadronic. The size of the fraction depends on the energy of the cluster. In fact most of the background comes from low energy jet fragmentation and hence the cut is designed to be tighter at smaller energies and looser at higher energies, where less background is expected and higher energy photons penetrate into the hadron calorimeter. This requirement has been optimized and it is implemented in the code as:

$$\text{HAD/EM} < 0.055 + 0.045 \times (E/100\text{GeV}) \quad (4.5)$$

At the energies we are considering, the electron and photon signatures in the calorimeter are nearly identical. The only tool to discriminate between the photon and the electron hypothesis relies on the existence of a track pointing to the EM cluster that can then be associated to an electron rather than a photon. Photons are electrically neutral and thus do not ionize the gas in the tracking chambers. As a result, there are no tracks associated with them. To eliminate the background resulting from electrons, only events with at least two clusters with no high  $P_T$  tracks pointing at them are accepted. In practice this is achieved by requiring at least two clusters, each with no more than one track with  $P_T > 1 \text{ GeV}$ , to allow for random tracks dissociated with the cluster:

$$\leq 1 \text{ 3D track with } P_T < 1 \text{ GeV} \quad (4.6)$$

For photon energies below 35 GeV, the CES is an efficient tool in discriminating photons while for energies larger than 35 GeV the multiple photons from neutral mesons decay are very boosted and thus too difficult to resolve in the CES. The CPR is used instead and a cut is applied requiring that there are no tracks pointing at the CPR for clusters with  $E_T > 35 \text{ GeV}$ .



### 4.3.3 Isolation

One important property of direct photons is that they are isolated, i.e. are produced without other particles nearby. On the contrary, neutral mesons decaying into photons, that can fake the signature of a direct photon, originate from jets and therefore are unlikely to be isolated. We determine the isolation for clusters in the central region of the detector by measuring the excess energy of the electromagnetic cluster in a cone of radius 0.4 about that cluster. This is defined as the energy inside the cone of radius 0.4 minus the energy of the cluster. The radius of the cone in  $\eta, \phi$  coordinates is:

$$R = \sqrt{\Delta\eta^2 + \Delta\phi^2} \quad (4.7)$$

The isolation energy is corrected for leakage across wedge boundaries and multiple interactions. In fact, it has been determined that the canonical (i.e. uncorrected for leakage) isolation requirement is less efficient for large energy clusters. If the cluster hits a tower near its edge in  $\phi$ , part of the cluster energy leaks into the adjacent tower that is not part of the cluster and thus it contributes to the isolation energy. If the leakage is large enough, a good photon can be rejected by this requirement. In addition, when multiple interactions occur, extra energy that is not part of the photon might be deposited inside the cone. Again, if this energy exceeds a certain value, a good photon might be rejected. These occurrences have been studied in detail and their effect quantified in parametrized curves that are used to correct the isolation energy[17, 18] . Thus, we require:

$$\text{Excess } E_T \text{ in of cone 0.4 (corrected for leakage)} < 2 \text{ GeV} \quad (4.8)$$

A further isolation requisite is that the total  $P_T$  of the tracks inside the cone is

less than 5 GeV:

$$P_T \text{ of tracks in cone } 0.4 < 5 \text{ GeV} \quad (4.9)$$

In addition, the CES chambers are used as a tool to discriminate direct photons from photons that are the result of the decay of a hadron and thus part of the background. In this latter case, in fact, the multiple photons could be resolved in the CES chambers. A particle crossing the CES deposits its energy in the strips and wires. The corresponding channels are clustered around the seed channel and a CES cluster is built. In addition, the energy in the channels is weighted and the centroid of the cluster is found. If a second CES cluster has an energy larger than the threshold, the event is rejected. This criterion is less efficient for very high energy photons that might mistakenly lead to two nearby CES clusters because of a fluctuation in how the energy is deposited in the CES chambers. Thus we use an energy dependent (or sliding) cut:

$$E_{\text{2nd strip or wire}}^{\text{cluster}} \leq 2.39 + 0.01 \times E_T \quad (4.10)$$

Finally, the separation in the  $\eta, \phi$  space between the two potential photons is required to be larger than 0.5 to avoid some of the energy of one of the photons leaking into the other photon's cone of radius 0.4:

$$\Delta R(\gamma_1 - \gamma_2) > 0.5 \quad (4.11)$$

## 4.4 The Central-Plug Diphoton Event Sample

### 4.4.1 Trigger

Two trigger paths were used to select the Central-Plug diphoton sample. In one case events with at least one isolated central EM cluster with  $E_T > 23$  GeV were selected.

Since the isolation requirement becomes inefficient for high energy photons, events that passed the 50 GeV non-isolated trigger were added. As briefly mentioned in section 3.8, the trigger performs the event selection in 3 steps, ranked accordingly to the complexity of the task they are able to perform. In the trigger hierarchy, the lower rank trigger is a prerequisite for next level. The requirements of each of the levels for the trigger paths used in this analysis are presented in the remainder of this section.

The level 1 trigger requires that at least one central EM trigger tower (i.e.  $0.2$  in  $\eta$  and  $15^\circ$  in  $\phi$ ) has at least 8 GeV of  $E_T$  deposited in it. Level 1 decision making is very fast and relies on basic information at the hardware level. A sufficient energy deposit in the calorimeter towers or a hit in the muon chambers is the first indication that a hard interaction might have occurred.

At level 2, the information on the event is more elaborate and includes approximate 2D tracking information as well as calorimeter clustering, measurement of  $\cancel{E}_T$  and  $\sum E_T$ , and matching of tracks to calorimeter clusters and muon stubs. The level 2 trigger is able to perform a simplified version of the offline clustering algorithm and works by searching for seed trigger towers, i.e. trigger towers with  $E_T$  above 3 GeV, and clustering them with shoulder trigger towers with  $E_T$  above 1 GeV. The events in our sample were required to have  $E_T$  of the CEM cluster larger than 23 GeV and to be in the central rapidity region ( $0 < |\eta| < 1.19$ ). An EM cluster is defined to have  $(\text{total } E_T)/(\text{EM } E_T) < 1.125$ . In addition, a neural net is implemented at level 2 that measures the energy in the  $3 \times 3$  trigger tower array,  $E_{3 \times 3}^{\text{ISO}}$ , which spans 3 towers in  $\eta$  and three towers in  $\phi$  around the seed trigger tower.  $E_{3 \times 3}^{\text{ISO}}$  must be below  $\sim 4$  GeV to select isolated clusters. Furthermore, some energy must be deposited in the CES in correspondence with the CEM cluster.

Table 4.1: Efficiencies for the isolated 23 GeV trigger up to  $E_T=55$  GeV and for the non-isolated 50 GeV trigger for  $E_T > 55$  GeV.

$E_T$ of the photon	Efficiency
25-26	$0.460 \pm 0.020$
26-27	$0.630 \pm 0.023$
27-28	$0.781 \pm 0.023$
28-29	$0.874 \pm 0.021$
29-30	$0.902 \pm 0.024$
30-31	$0.934 \pm 0.024$
31-55	$0.963 \pm 0.008$
$>55$	$0.993 \pm 0.004$

Finally, at level 3, a more precise measurement of the cluster energy is available as the offline calorimeter clustering software is used. This new measurement of  $E_T$  is again required to be above 23 GeV.

The 50 GeV trigger has a 50 GeV  $E_T$  threshold, but no isolation or CES constraints, except for level 3 fiducial cuts on the CES cluster position.

The trigger efficiency depends on the  $E_T$  of the cluster. The 23 GeV trigger is 96% efficient for  $31 \text{ GeV} < E_T < 55 \text{ GeV}$ . The events with  $E_T > 55 \text{ GeV}$  are taken from the 50 GeV non isolated trigger, and in this region the 50 GeV trigger is more than 99% efficient. The trigger efficiencies have been measured in[19]. Table 4.1 summarizes the trigger efficiencies for events that have already satisfied the offline inclusive photon selection.

#### 4.4.2 Offline Selection

The events that have passed the online trigger selection are written to tape. Offline, they are read out and converted into an ntuple format that contains variables to

represent the different physics objects and detector outputs. In order to clean up the sample and to select events with two photons, one central and one plug, we resort to a set of constraints for the variables described henceforth.

The events are required to have at least one central cluster that passes the same offline selection described for the CC diphoton sample but with a tighter  $E_T$  cut of 25 GeV. After the central cluster selection and the global event cuts are applied, there are 11379 events remaining.

Selecting photons in the plug is a more difficult task. In fact, not all of the tools utilized to select central photons are available in this region of the detector. The main reason is that the CTC (Central Tracker) does not cover the plug region and thus the tracking information available in the plug is limited to the VTX and SVX detectors. Tracking information is necessary to discriminate neutral particles, such as photons, from charged particles, like electrons. Electrons deposit energy in the calorimeter in much the same way as photons and thus cannot be distinguished based on calorimeter information. Although the SVX provides a measurement of electron tracks, it is not used in the selection for this analysis as the SVX detector is not instrumented for  $|z| > 30$  cm. Moreover, a precision measurement of the cluster shower profile cannot be achieved for all plug clusters, as the strip chambers in the plug extend only up to a pseudorapidity of 1.8, and there is no preradiator in the plug. Measurements of the shower profile are useful to discriminate between direct photons and the products of neutral meson decays. A plug photon with  $E_T > 22$  GeV, however, corresponds to a total energy that ranges between 37 GeV and 122 GeV for  $\eta$  values of 1.1 to 2.4. At such energies it is very difficult to resolve the photons resulting from the decay of neutral mesons, as they are very boosted. Despite these shortcomings, the Central-Plug diphoton sample serves the purpose of increasing the statistics of the CDF diphoton sample and thus improving the reach of searches involving diphotons.

Plug clusters are required to have  $E_T > 22$  GeV and to be in the plug region of the detector, with  $1.1 < |\eta| < 2.4$ . Portions of the detector that are not instrumented are excluded from the search. This occurs within 5 degrees of the 4 plug cracks, where the 4 quadrants that constitute the plug come together.

Similar to central clusters, the selection for plug clusters consists of constraints on isolation, tracks, and shower profile properties, ensuring that the cluster is consistent with a photon.

In order to reduce the background from charged particles, the ratio of hits in the VTX wires versus the number of expected hits along the road between the CEM cluster and the vertex of the event interaction (this ratio is also known as VTX *occupancy*) must be lower than 0.4:

$$\text{VTX Occupancy} < 0.4. \quad (4.12)$$

For the reasons mentioned at the beginning of this section, we do not use the plug strip chambers to determine the shower profile. Instead, the energy deposited in the  $3 \times 3$  tower array enclosing and including the seed tower is compared to the energy deposit predicted by testbeam electrons. The  $\chi^2$  is measured in the following way:

$$\chi^2(3 \times 3) = \frac{1}{9} \sum_i \frac{(E_i - E_i^{\text{tb}})^2}{(\Delta E_i)^2}, \quad (4.13)$$

where  $E_i$  is the energy in tower  $i$ ,  $\Delta E_i$  is the uncertainty associated with this measurement, and  $E_i^{\text{tb}}$  is the predicted energy from testbeam data. The  $\chi^2(3 \times 3)$  is required to have a maximum value of 5:

$$\chi^2(3 \times 3) < 5. \quad (4.14)$$

Similar to central clusters, a sliding HAD/EM cut is applied to select clusters that have most of their energy deposited in the EM partition of the calorimeter. The

cut has been optimized by studying plug electrons to maximize the rejection of low energy jet fragmentation background, while it is less severe for high energy clusters that are less likely to be part of this background:

$$\text{HAD/EM} < (0.028 + 0.00019 \times E/\text{GeV}) \quad (4.15)$$

Finally, an isolation requirement is applied to suppress the background from jets. The isolation for central clusters relies on the measurement of the excess transverse energy inside a cone of radius 0.4 around the cluster. However, as we will describe in section 4.5, this method is not as efficient in discriminating plug photons. In the plug, we will define the isolation  $E_T$  of the cluster as the  $E_T$  inside an annulus between 0.4 and 0.7 about the photon candidate direction. Plug clusters are subjected to the following constraint:

$$E_T \text{ in annulus between 0.4 and 0.7} < 4 \text{ GeV} \quad (4.16)$$

After the CP selection is applied, there are 192 events in the sample. Table 4.2 summarizes the plug cluster selection and the number of events surviving after each cut.

## 4.5 Plug Photon Isolation

We resort to a data control sample containing  $Z^0 \rightarrow e^+e^-$  events with the purpose of verifying whether there is any unusual behavior of the observables in the Central-Plug diphoton sample (in the next section, we will see how this same data set is used to measure the efficiencies of the selection cuts). If one ignores the tracks associated with them, electrons otherwise behave almost identically to photons. Furthermore, on-shell  $Z^0$ 's decaying into electron-positron pairs provide a potentially clean sample

Table 4.2: Plug cluster selection and events passing.

Plug cluster cuts	Events passing
At least one tight central cluster and a plug cluster ( $1.1 <  \eta  < 2.4$ )	11379
$E_T > 22$ GeV	2762
Fiducial	2365
$\chi^2(3 \times 3) < 5$	810
$\text{HAD/EM} < (0.028 + 0.00019 \times E/\text{GeV})$	528
VTX Occupancy $< 0.4$	242
$E_T$ in annulus between 0.4 and $0.7 < 4$ GeV	192

provided a tight electron selection and a mass window cut are applied. It is thus reasonable to use an electron control sample to gain insight on the photon signal.

There are approximately 2700 events in the electron control sample with at least one central cluster that passes tight electron identification cuts (this is the same selection used in the discovery of the top quark [21]) and a plug cluster, whose invariant mass is between 81 GeV and 101 GeV ( $\sim 10$  GeV about the  $Z^0$  peak). In figure 4.1, the  $\eta$  dependence of the cone isolation energy ( $E_T$  in the cone of 0.4 not including the  $E_T$  of the cluster) is shown for plug electrons in the control sample that passed the same selection (except the no-track requirement) as the plug photon candidates in the Central-Plug diphoton data. The isolation energy is observed to increase with  $\eta$ . Such a feature of the isolation does not occur for central clusters. For central clusters in fact both the cone 0.4 isolation  $E_T$  and annulus isolation  $E_T$  are flat in  $\eta$ . We examine two possible explanations for the increase of the cone 0.4 isolation  $E_T$  with  $\eta$ . First, we look into the possibility that the underlying event contribution to the  $E_T$  inside the cone might be  $\eta$  dependent. The other possibility is that what we observe is an effect of the plug clustering algorithm.



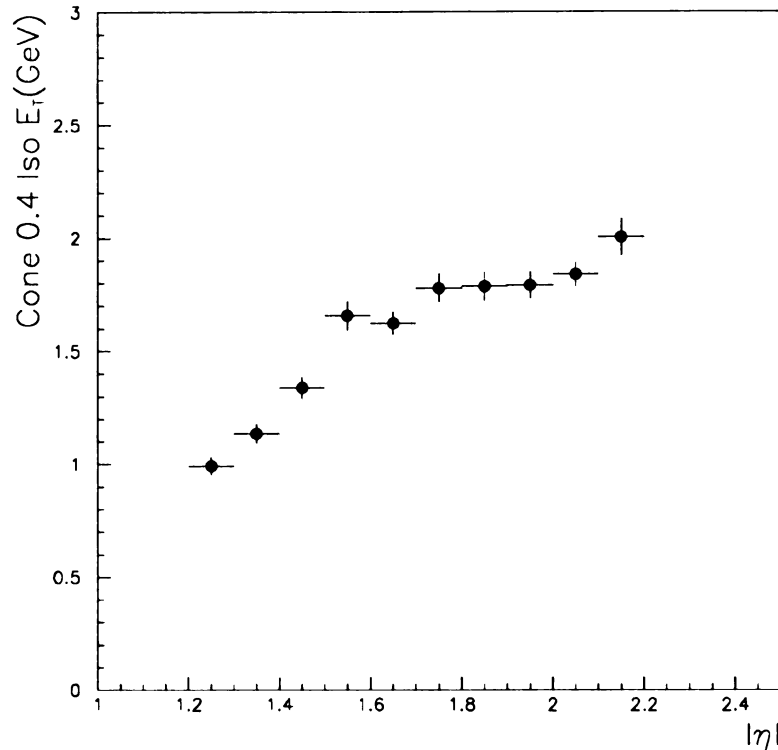


Figure 4.1:  $\eta$  dependence of the cone 0.4 isolation  $E_T$  ( $Z^0 \rightarrow e^+e^-$  events).

#### 4.5.1 Underlying Event in Run 1b Minimum Bias and $Z^0$ Events

Underlying events pertain all the processes that contribute to the energy deposited in the detector not related to the hard scattering, such as the fragments of the original  $p\bar{p}$  system and/or soft spectator interactions. This additional energy would affect the measurement of the cone of 0.4 isolation  $E_T$  if deposited in the calorimeter in an  $\eta$  dependent fashion. Two instances have been considered: underlying events in minimum bias and in  $Z^0 \rightarrow e^+e^-$  events.

## Minimum Bias Events

The sample used in this study consists of about 400,000 Run 1b minimum bias events. Minimum bias interactions occur when some beam-beam interaction has taken place and hence there are coincident hits in the beam-beam counters in within 15 ns around bunch crossing (see section 3.7). For each event, a direction in azimuth and pseudorapidity is randomly chosen. We calculate the transverse energy inside a cone that lies along that direction for three cone sizes (0.4, 0.7, 1.0) and also for an annulus between 0.7 and 0.4 and examine its behavior versus  $\eta$ . Figure 4.2 indicates that there is in fact an overall increase in the underlying event contribution to the  $E_T$  inside the cone, however it is not sufficient to explain the faster rise observed in the data. In addition, we observe dips in the distributions. These dips are aligned with the  $\eta$  boundaries between the different regions of the detector: central, plug and forward. As the cone gets closer to a boundary, in fact, some energy is lost in the crack in the detector, producing the dips. And, since a bigger cone reaches the boundary earlier, the larger the cone size, the wider are the dips.

## $Z^0 \rightarrow e^+e^-$ Control Sample

Since the underlying event contribution may be dependent on the physics of the particular interaction that has taken place, a similar study was carried out using the  $Z^0 \rightarrow e^+e^-$  control sample. Again, a random direction is chosen in space but in this case one first ascertains that the electromagnetic clusters in the event do not fall inside the random cone. The curves in figure 4.3 suggest the same general features observed in the minimum bias case. We conclude that the underlying event energy does not fully explain the increase in isolation energy with  $\eta$ .

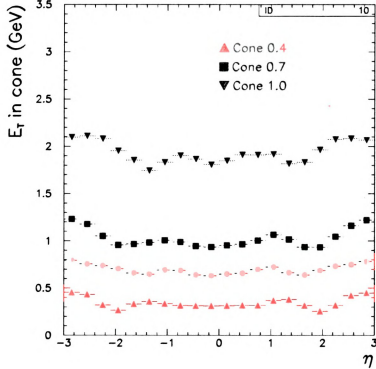


Figure 4.2:  $E_T$  in cone vs  $\eta$  in minimum bias events.

#### 4.5.2 Plug Clustering Algorithm

As explained in section 4.2, the plug clustering algorithm works by sorting the plug towers according to their transverse energy, picking a seed tower and clustering it together with nearby towers. The cluster is complete when an energy valley is found or when the limit of 25 towers is reached. Since the physical size of the towers decreases at higher pseudorapidities, the average number of towers included in plug clusters increases with  $\eta$ . This behavior, exemplified for plug clusters in the  $Z^0$  sample in figure 4.4, can affect the isolation energy. On one hand, the larger the number of towers included in a cluster, the smaller the isolation energy should be. In fact, as

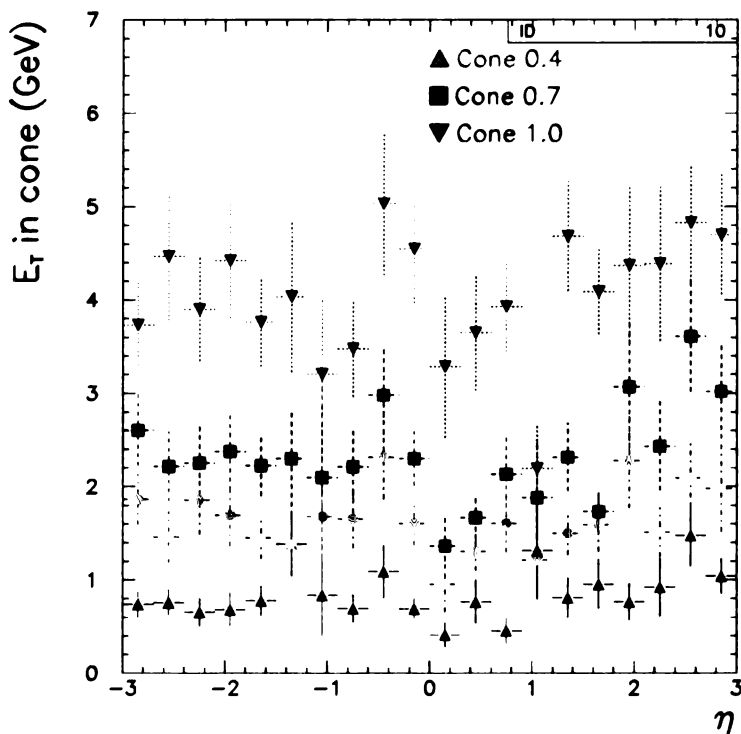


Figure 4.3:  $E_T$  in cone vs  $\eta$  in  $Z^0 \rightarrow e^+e^-$  events.

more towers are included in the cluster, fewer towers are left outside the cluster to contribute to the isolation energy. However, since there is a threshold energy in the clustering algorithm, more towers will fail the threshold cut at higher  $\eta$  where towers are smaller, thus more of the cluster energy leaks outside the cluster increasing the isolation energy.

To avoid these effects, we define the isolation energy of plug clusters as the transverse energy contained in the annulus between 0.4 and 0.7. In fact, with a simple calculation, it is possible to determine that there are approximately 55 EM towers included in a radius of 0.4 (the  $\eta$ ,  $\phi$  segmentation in the plug is  $0.1 \times 5^\circ$ ), ensuring that even the larger clusters are contained inside this radius. As a result, the cluster

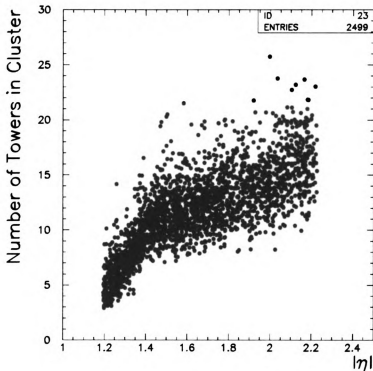


Figure 4.4: Number of towers included in a cluster in  $Z^0 \rightarrow e^+e^-$  events correlated with  $|\eta|$ .

does not leak into the annulus and thus the measurement of the isolation energy is not affected by the clustering algorithm. We choose 4 GeV as the transverse energy threshold inside the annulus for isolated plug clusters. This is motivated by the fact that the area inside the annulus is about twice as large as the area inside a cone of 0.4, where the isolation  $E_T$  was required to be smaller than 2 GeV. Figure 4.5 displays the annulus  $E_T$  distribution plotted with respect to  $\eta$ .

Although the annulus distribution is not flat in  $\eta$ , using the  $Z \rightarrow e^+e^-$  control sample we determine that for plug clusters the efficiency of the annulus isolation cut is approximately 10% larger than the efficiency of the cone 0.4 isolation cut. In addition,

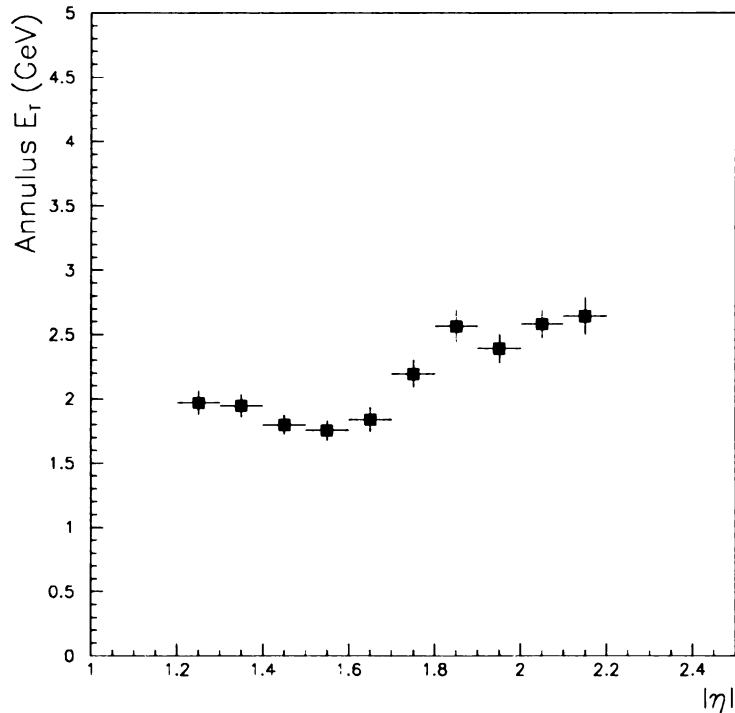


Figure 4.5:  $\eta$  dependence of the annulus  $E_T$  ( $Z^0 \rightarrow e^+e^-$  events).

figure 4.6 indicates that, for higher values of  $\eta$ , the annulus efficiency is larger than the cone 0.4 efficiency and thus the annulus cut does not bias the sample toward lower  $\eta$  clusters as much as the cone 0.4 cut. Figure 4.7 displays the  $E_T$  dependence of the annulus and cone 0.4 isolation  $E_T$  efficiency distributions.

Since we plan to use the Central-Plug diphoton data sample for searches, we conclude that the annulus isolation is a more appropriate selection for a search than the cone 0.4 isolation because it retains more of the signal.

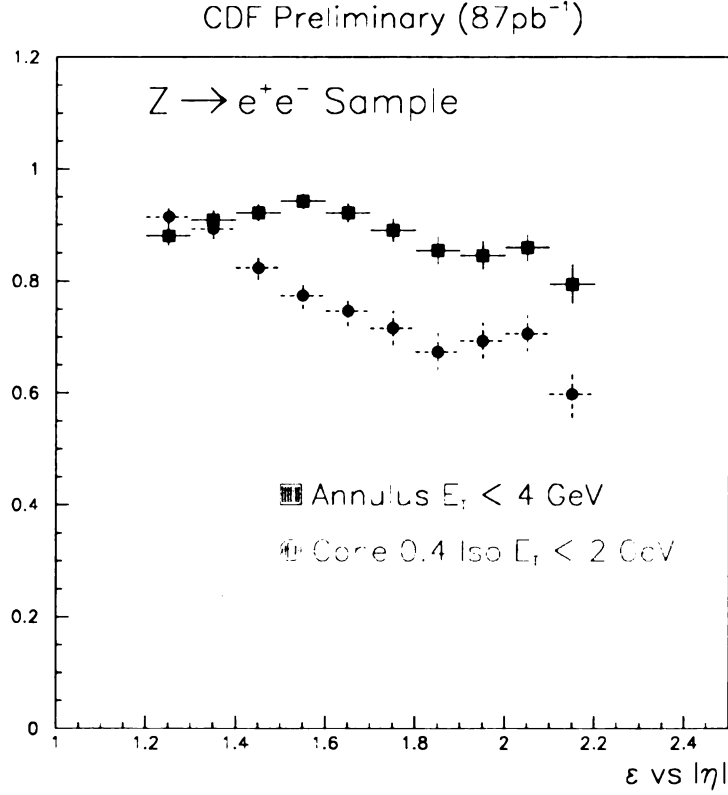


Figure 4.6:  $\eta$  dependence of the efficiency for annulus (squares) and cone 0.4 isolation (circles)  $E_T$  ( $Z^0 \rightarrow e^+e^-$  events).

## 4.6 Efficiencies

The efficiencies for the Central-Central and Central-Plug selections are computed by using the  $Z^0 \rightarrow e^+e^-$  control data sample. In addition, we generate simulated  $Z^0 \rightarrow e^+e^-$  events using Pythia and QFL to quantify the differences between the Monte Carlo simulation and the real detector. This is necessary because some features of the detector are not included in the simulation.

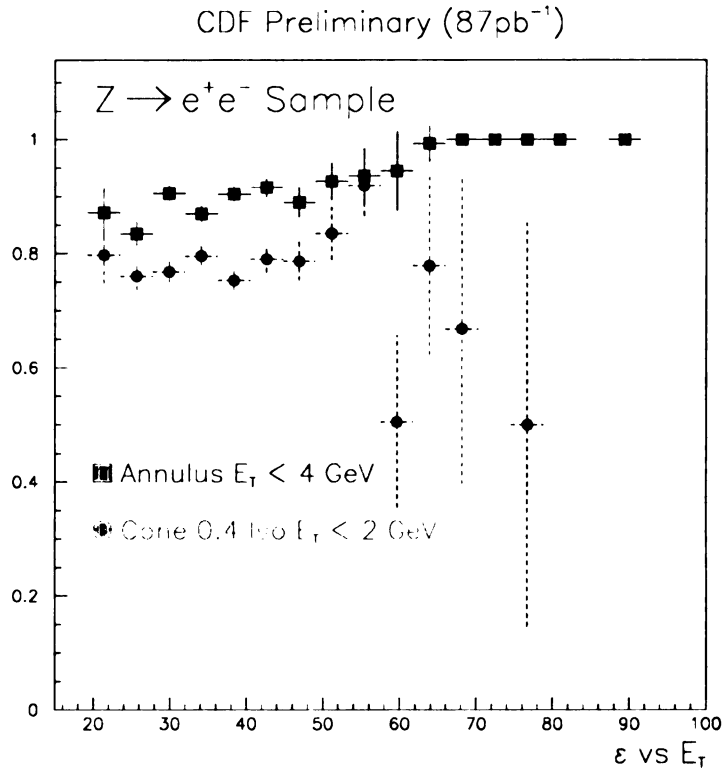


Figure 4.7: Efficiency of the Annulus  $E_T$  (circles) and Cone 0.4 (triangles) isolation versus  $E_T$  ( $Z^0 \rightarrow e^+e^-$  events).

#### 4.6.1 Central-Central Diphoton Selection Efficiency

The efficiency for the cuts used in selecting the Central-Central diphoton sample have been computed in previous CDF analyses and are referenced in [18, 27]. The overall efficiency is  $63 \pm 6\%$ .



Table 4.3: Efficiencies and correction factors for global event selection and central photon identification cuts. In the table, ETOUT means out-of-time energy.

Cuts	Efficiency	Correction Factor
Z Vertex	$94.9 \pm 2.3\%$	$0.965 \pm 0.008$
ETOUT=0.0	$97.5 \pm 0.4\%$	$0.975 \pm 0.004$
Central Photon Selection	$83.2 \pm 1.5\%$	$0.896 \pm 0.047$

## 4.6.2 Central-Plug Diphoton Selection Efficiency

### Efficiencies for Global and Central Leg Cuts

The efficiencies of the  $z$  vertex, out-of-time energy and central photon cuts have been determined in previous Central-Central diphoton analyses [18, 27] and are listed in table 4.3. The trigger efficiency has been measured in [19] and depends on the the  $E_T$  of the photon. This dependence is summarized in table 4.1.

In order to directly compare the data to the MC, one must take into account the fact that some of the detector features (as for example multiple interactions and shower leakage) are not modeled in QFL. Thus it is necessary to multiply the MC by a correction factor defined as the ratio between the efficiency in the  $Z$  data sample and the efficiency in the  $Z$  MC sample. Out-of-time energy and trigger requirements are not simulated in QFL, thus their correction factors are simply the efficiencies measured in the data. The correction factors for global and central leg cuts are listed in table 4.3.

## Efficiencies for Plug Leg Cuts

The efficiencies of the  $\chi^2(3 \times 3)$ , HAD/EM and annulus isolation cuts applied to the plug clusters are evaluated using the  $Z^0$  data control sample.

This is achieved by selecting events with the requirement that the central electron candidate passes the tight electron selection[21]. In addition, the plug electron candidate in the event is required to be in the fiducial region of the PEM and to have  $E_T > 22$  GeV. Finally, the invariant mass of the central-plug electron pair is constrained to be within 10 GeV about the  $Z^0$  mass peak, i.e.  $81 \text{ GeV} < M_{ee} < 101 \text{ GeV}$ . To further increase the purity of the  $Z^0$  sample, we perform a side bin subtraction<sup>2</sup>.

The efficiency for a plug cut ( $\chi^2(3 \times 3)$ , HAD/EM or annulus isolation cut) is defined as the ratio between the number of events in the  $Z$  data sample selected above that survive after the  $\chi^2(3 \times 3)$ , HAD/EM and annulus isolation cuts are applied and the number of events that pass two of these requirements with the exception of the cut whose efficiency is being computed. The efficiency for each of the cuts as well as their total efficiency are listed in table 4.4.

The efficiency of the VTX occupancy cut cannot be determined by using the  $Z^0$  sample as electrons have tracks associated with them. Instead, we use minimum bias events and determine the ratio between the number of events with a VTX occupancy of 0.4 or less and the total number of events. For each event, the VTX occupancy is calculated along a random road in  $\eta$ ,  $\phi$  originating from the vertex in the event. The ratio represents the efficiency for rejecting events with prompt photons that have a track associated originating from underlying events. This is the efficiency of the VTX

---

<sup>2</sup>In the  $Z^0$  control sample in addition to real  $Z^0$ 's, there is a contribution from off-shell photons producing  $e^+e^-$  pairs. We reduce this background by fitting the side bins ( $56 \text{ GeV} < M_{ee} < 76 \text{ GeV}$  and  $106 \text{ GeV} < M_{ee} < 126 \text{ GeV}$ ) in the invariant mass distribution of the electron pair with an exponential and then extrapolate this shape underneath the  $Z^0$  peak to estimate the background contribution in the signal region. This contribution is of the order 5% and it is subtracted from the events in the peak.

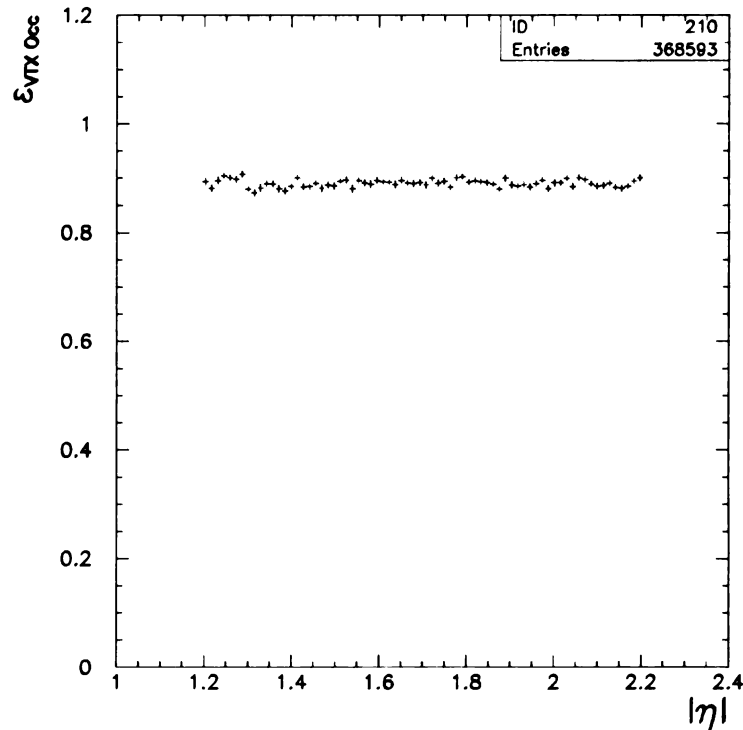


Figure 4.8:  $\eta$  dependence of the efficiency for the VTX occupancy cut (minimum bias events).

cut and it is measured to be  $89.06 \pm 0.07$  %. Figure 4.8 indicates that the VTX efficiency is flat in  $\eta$ .

The total efficiency for the plug cuts is obtained by multiplying the VTX occupancy cut efficiency by the efficiency of the additional plug cuts and is listed in table 4.4. The  $\eta$  and  $E_T$  dependences of the efficiency for the plug cluster cuts are shown in figures 4.9 and 4.10.

The total efficiency for the Central-Plug selection is calculated by multiplying the following pieces:

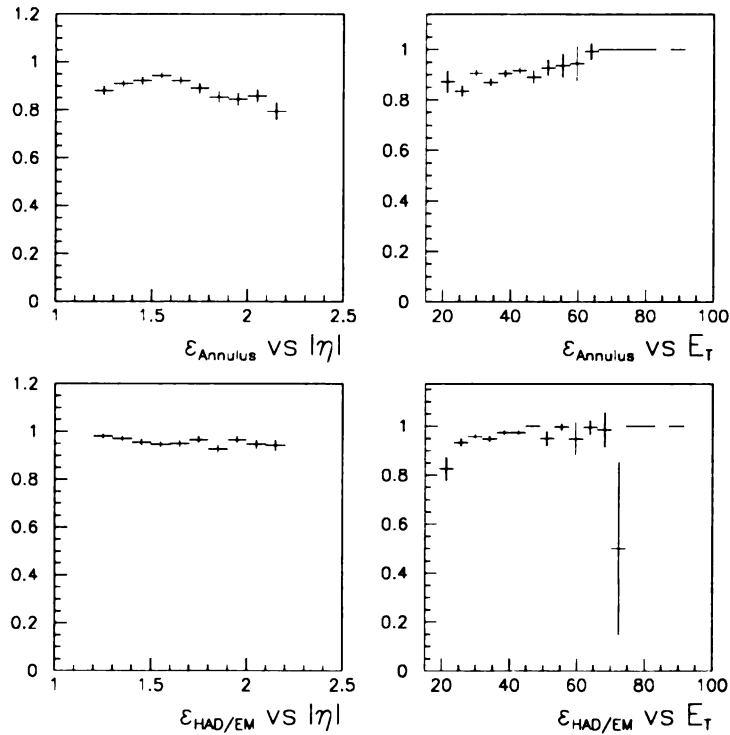


Figure 4.9:  $\eta$  and  $E_T$  dependence of the efficiency for the plug cuts ( $Z^0 \rightarrow e^+e^-$  events).

- $\epsilon_{\text{central}} = 0.832 \pm 0.015$  (efficiency for the central-leg cuts from table 4.3 with statistical and systematic uncertainties included [18]);
- $\epsilon_{\text{plug}} = 0.742 \pm 0.094$  (efficiency for the plug-leg cuts from table 4.4 with statistical and systematic uncertainties included. The main contribution to the systematic uncertainty is the systematic uncertainty associated with the annulus isolation cut. Varying the annulus isolation cut by  $\pm 1\text{GeV}$ , consistently with the observed range of the annulus values in the  $\eta$  dependence, produces a 10% shift in the annulus cut efficiency. Other systematic uncertainties are measured by the difference between the data and MC efficiency );

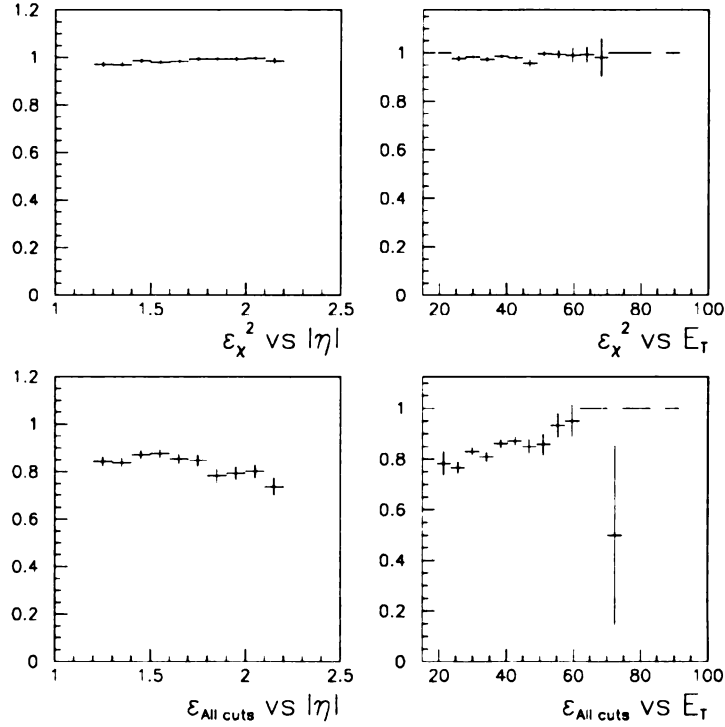


Figure 4.10:  $\eta$  and  $E_T$  dependence of the efficiency for the plug cuts ( $Z^0 \rightarrow e^+e^-$  events).

- $\epsilon_{\text{global}} (31 \text{ GeV} < E_T < 55 \text{ GeV} \text{ bin only}) = \epsilon_{\text{trigger}} \times \epsilon_{z_{\text{vert}}} \times \epsilon_{\text{ETOUT}} = 0.963 \times 0.949 \times 0.975$  (efficiency for the trigger, out-of-time energy (ETOUT),  $z_{\text{vert}}$  global cuts; the values are from table 4.3 for the ETOUT and  $z_{\text{vert}}$  cuts and from table 4.1 for the trigger efficiency).

We find (statistical and systematic uncertainties combined):

$$\begin{aligned}
 \epsilon_{\text{CP}} &= \epsilon_{\text{central}} \times \epsilon_{\text{plug}} \times \epsilon_{\text{global}} \\
 &= 0.550 \pm 0.065
 \end{aligned}
 \tag{4.17}$$

In the plug region, QFL incorrectly models the electromagnetic shower in the

Table 4.4: Efficiencies for the plug photon identification cuts (statistical uncertainty only).

Cuts	Efficiency
$\chi^2(3 \times 3) < 5$	$98.3 \pm 0.3\%$
$\text{HAD/EM} < (0.028 + 0.00019 \times E/\text{GeV})$	$95.7 \pm 0.4\%$
$E_T$ in annulus between $0.4$ and $0.7 < 4 \text{ GeV}$	$89.1 \pm 0.6\%$
Total efficiency from $Z^0$ sample	$83.3 \pm 0.7\%$
VTX Occupancy $< 0.4$	$89.06 \pm 0.07\%$
Total efficiency for the Plug Photon Selection	$74.2 \pm 0.6\%$

PEM [20]. Based on this, we do not rely on the QFL simulation for the plug cuts and we use the efficiency from the data (Minimum Bias data for the VTX efficiency and  $Z^0 \rightarrow e^+e^-$  for the remaining cuts) as the correction factor for the plug cuts. We determine the overall correction factor for the Central-Plug sample by multiplying the following factors:

- $\text{CF}_{\text{central}} = 0.896 \pm 0.047$  (correction factor for the central-leg cuts from table 4.3 with statistical and systematic uncertainties included [18]);
- $\epsilon_{\text{plug}} = 0.742 \pm 0.094$  (efficiency for the plug-leg cuts from table 4.4);
- $\text{CF}_{\text{global}}$  (the result is shown for the  $31 \text{ GeV} < E_T < 55 \text{ GeV}$  bin only) =  $\epsilon_{\text{trigger}} \times \text{CF}_{z_{\text{vert}}} \times \epsilon_{\text{ETOUT}} = 0.963 \times 0.965 \times 0.975$  (efficiency for the trigger, ETOUT,  $z$  vertex global cuts; the values are from table 4.3 for the ETOUT and  $z$  vertex cuts are from table 4.1 for the trigger efficiency).

This yields (the uncertainty is statistical and systematic combined):

$$CF_{CP} = CF_{\text{central}} \times \epsilon_{\text{plug}} \times CF_{\text{global}} = 0.602 \pm 0.090 \quad (4.18)$$

## 4.7 Summary

The data selection described in this chapter has been carried out to select diphotons that are produced in a pseudorapidity region that covers the plug portion of the CDF detector. The CDF diphoton data sample consists of 479 events. The invariant mass spectrum of these events is shown in figure 4.12. The Central-Plug sample corresponds to an integrated luminosity of  $87\text{pb}^{-1}$  and contributes 192 events to the CDF diphoton sample. The invariant mass distribution of the events in the Central-Plug sample is shown in figure 4.11. The Central-Central diphoton sample includes 287 events corresponding to an integrated luminosity of  $100\text{pb}^{-1}$ .

## 4.8 Acceptance $\times$ Efficiency for a Higgs decaying to $\gamma\gamma$

An interesting way to determine the performance of the CC+CP diphoton sample compared to the CC sample alone is to calculate the acceptance for a narrow resonant state for the CC+CP sample and compare it to the CC sample. This study is carried out by using a MC sample of Higgs decaying into two photons.

We generate 5000 events for 20 different Higgs masses (between 60 and 200 GeV) using Pythia[22]. The acceptance  $\times$  efficiency is calculated for each mass by dividing the number of events left after the diphoton selection used in the data (and with an invariant mass within a  $3\sigma$  window around the generated mass) by the number of generated events:

$$\text{Acceptance} \times \epsilon = \frac{N_{\gamma\gamma}(M_{H^0} \text{ in } 3\sigma \text{ window})}{5000} \quad (4.19)$$

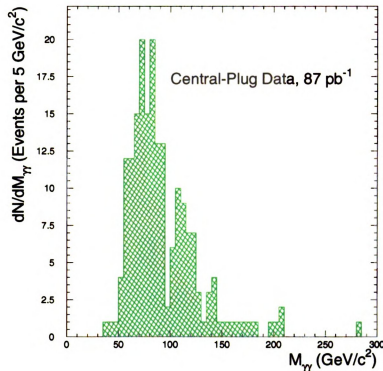


Figure 4.11: Invariant mass distribution of the events in the Central-Plug diphoton sample.

The plot in the upper left corner of figure 4.13 shows the acceptance  $\times$  efficiency for the events in the Central-Central sample only and for the Central-Central and Central-Plug combined samples for events that have passed the diphoton selection. The same study is carried out for events that, in addition to at least two photons passing the diphoton selection, have a  $W^\pm$  or a  $Z^0$  in the final state. In order to include both hadronic or leptonic decays of the  $W^\pm$  and  $Z^0$  bosons, we accept events that have:

- at least one tight<sup>3</sup> central electron with  $E_T > 20$  GeV, or

---

<sup>3</sup>This is the same selection used in the top lepton plus jets analyses[21].



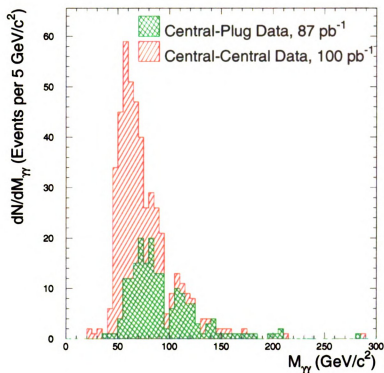


Figure 4.12: Invariant mass distribution of the events in the CDF diphoton sample. The contributions from the Central-Plug sample and Central-Central sample are also shown.

- at least one tight central muon with  $P_T > 20$  GeV/c, or
- $E_T > 20$  GeV and  $\Delta\phi(E_T\text{-jets}, \gamma) > 25^\circ$ ,  $\Delta\phi(E_T\text{-lepton}) > 10^\circ$ , or
- 2 jets with:
  - $E_T > 15$  GeV
  - $|\eta| < 2$
  - $\Delta R(\text{jet-}\gamma), \Delta R(\text{jet-}e) > 0.4$
  - $40 < M_{JJ} < 140$  GeV

The plot in the upper right corner of figure 4.13 displays the acceptance  $\times$  efficiency for these events. The bottom plots in figure 4.13 display the acceptance  $\times$  efficiency for events that, in addition to the two photons, have respectively 1 or more jets (left) and two or more jets (right). The jets pass the following the selection:

- $E_T > 15 \text{ GeV}$
- $|\eta| < 2$
- $\Delta R(\text{jet} - \gamma) > 0.4$

We conclude that by including the plug we improve the diphoton acceptance by about 50% or more.

The invariant mass distributions for the events in the Central-Plug and Central-Central data samples that, in addition to the diphoton selection, pass the 1 or more jets and 2 or more jets requirements are shown in figures 4.14 and 4.15.

In the Central-Plug data sample there are 7 events passing the diphoton selection and the  $W^\pm/Z^0$  selection; all 7 pass the missing  $E_T$  selection, including one event that passed the two jet selection also (Run 67634, Event 302137,  $M_{JJ} = 99.6 \text{ GeV}$ ,  $M_{\gamma\gamma} = 143.8 \text{ GeV}$ ,  $E_T = 23 \text{ GeV}$ ). Run and event number as well as other properties of these events are summarized in table 4.5.

In the Central-Central diphoton sample there are six events passing the  $W^\pm/Z^0$  selection. A summary of these events can be found in [18]. The invariant mass distribution for the events passing the diphoton +  $W^\pm/Z^0$  selection for both the Central-Plug sample and Central-Central, Central-Plug samples combined is shown in figure 4.16.

Table 4.5: Events in the Central-Plug diphoton sample that pass the  $W^\pm/Z^0$  selection.

Run	Event	Selection	$M_{\gamma\gamma}$	Properties
66315	168717	$E_T$	64.7	$E_T=21.4$ GeV
63972	6537	$E_T$	49.6	$E_T=20.1$ GeV
66450	162196	$E_T$	35.8	$E_T=24.8$ GeV
67634	302137	$E_T$ , jet-jet	143.8	$E_T=23.0$ GeV, $M_{JJ}=99.6$ GeV/c <sup>2</sup>
67561	239882	$E_T$	74.2	$E_T=20.2$ GeV
70606	104896	$E_T$	112.8	$E_T=23.5$ GeV
61528	32100	$E_T$	169.9	$E_T=28.4$ GeV

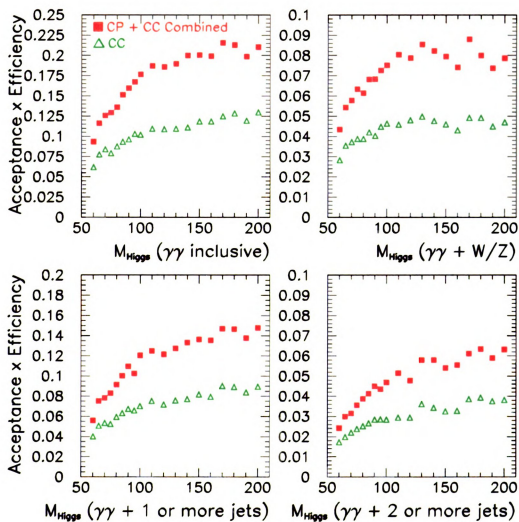


Figure 4.13: Acceptance  $\times$  efficiency for Pythia Higgses of different masses. The triangles show the acceptance  $\times$  efficiency for Central-Central diphotons and the squares for the Central-Central and Central-Plug combined.

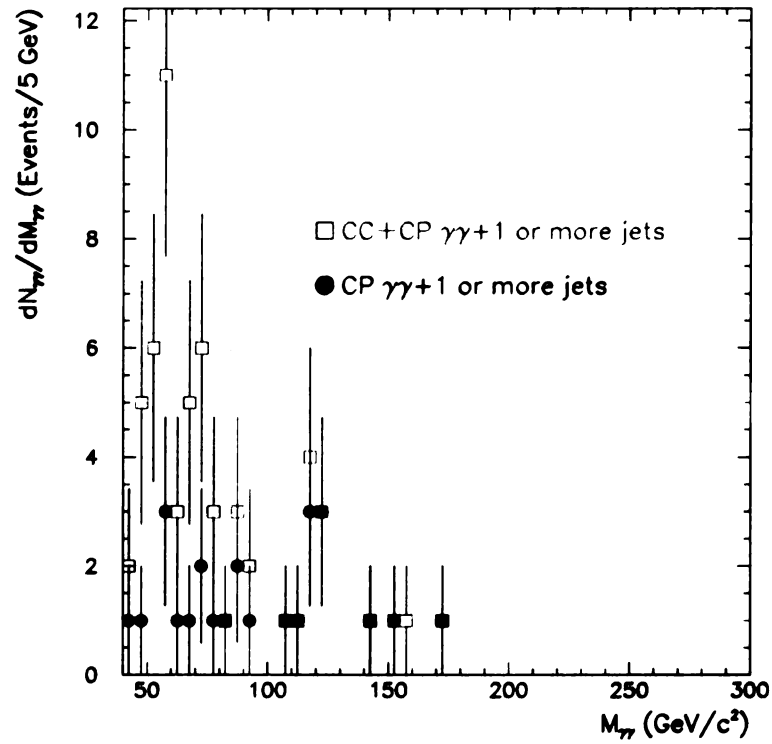


Figure 4.14: Invariant mass distribution for events with one or more jets in addition to two photons for the Central-Plug diphoton selection (circles) and for the CC and CP samples combined (squares).

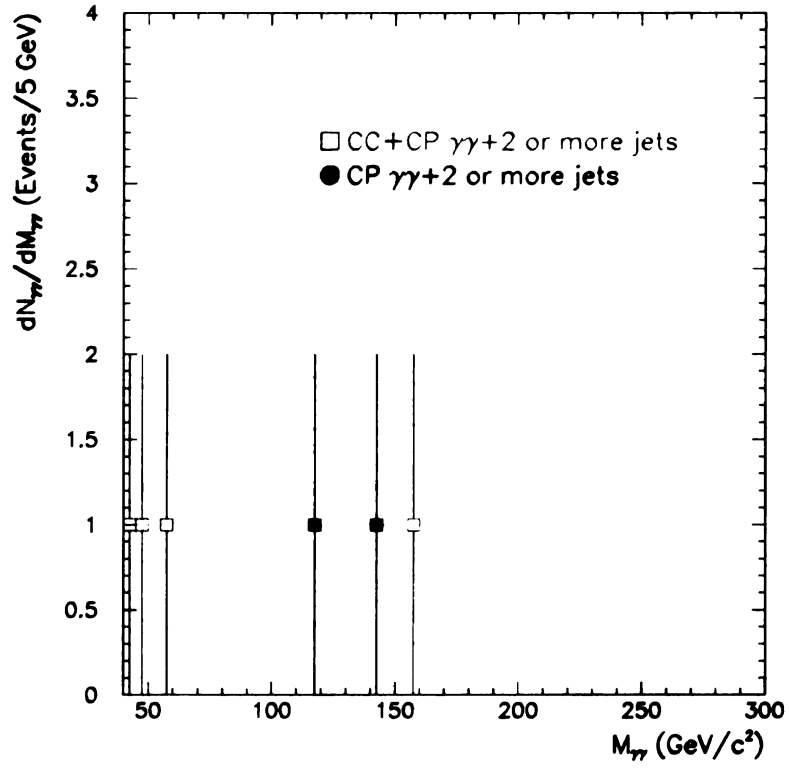


Figure 4.15: Invariant mass distribution for events with two or more jets in addition to two photons for the Central-Plug diphoton selection (circles) and for the CC and CP samples combined (squares).

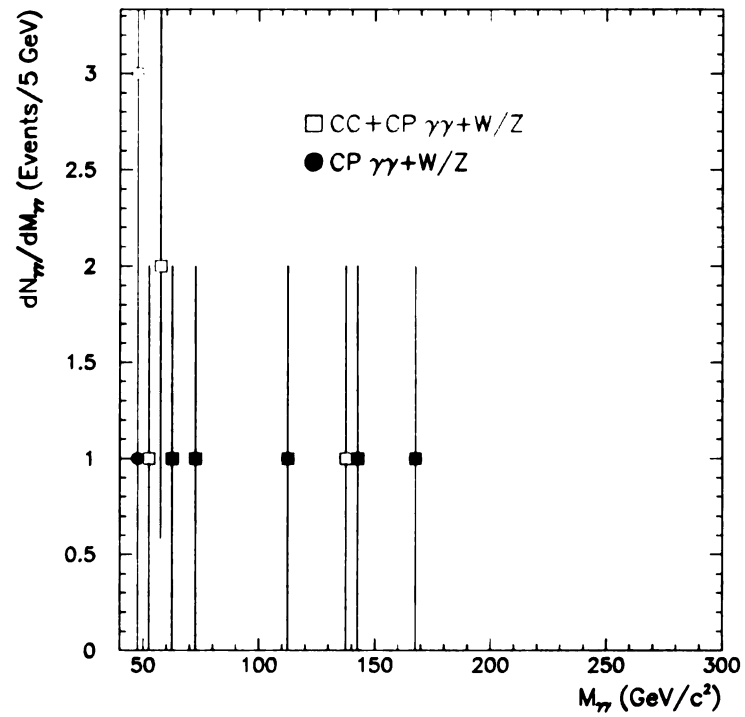


Figure 4.16: Invariant mass distribution for events passing the  $W^{\pm}/Z^0$  requirements in addition to the diphoton selection for the Central-Plug diphoton selection (circles) and for the CC and CP samples combined (squares).

# Chapter 5

## Background Study

### 5.1 Introduction

The selection described in chapter 4 is optimized to preserve most of the direct diphoton signal while suppressing the background. Nevertheless, some background events survive the selection and make it into the Central-Plug and Central-Central diphoton samples. The bulk of the samples consists in fact of events with one or more jets in the final state that fake the direct photon signature. In section 5.3 the purity of the CP sample will be evaluated by employing tools that include data control samples, Monte Carlo simulations and, at times, a combination of both.

In section 5.2 the contribution from SM sources that produce prompt diphotons in the Central-Plug data sample will be estimated. An overview of prompt diphoton production in the Standard Model can be found in chapter 1.

The background study for the Central-Central diphoton sample has been carried out in [18, 27]. A brief overview of this study can be found in section 5.5.



## 5.2 Standard Model $\gamma\gamma$ Contribution in the Central-Plug Diphoton Sample

The Standard Model processes that primarily contribute to prompt diphoton production are:  $q\bar{q} \rightarrow \gamma\gamma$  and  $gg \rightarrow \gamma\gamma$ .

These contributions are evaluated with Pythia by generating  $q\bar{q} \rightarrow \gamma\gamma$  and  $gg \rightarrow \gamma\gamma$  Standard Model events using CTEQ5M structure functions and subsequently simulating the CDF detector response with QFL. The integrated luminosity of the SM  $\gamma\gamma$  Monte Carlo sample is  $\sim 6396\text{pb}^{-1}$ . The QFL output is converted into the same ntuple format as the data and, in principle, the same selection that was applied to the data can be applied to the Monte Carlo. In practice, as we mentioned in the previous chapter, some of the detector features, for instance shower development, are not well simulated and thus the corresponding cuts are not applied.

There are  $N_{\gamma\gamma} \sim 10000$  events in the MC sample that pass the central cuts and have at least one fiducial plug cluster with  $E_T > 22$  GeV. In order to extract the number of diphoton events from leading order Standard Model sources expected in the CP data sample,  $N_{\gamma\gamma}$  must be rescaled to the luminosity of the data,  $87\text{pb}^{-1}$ , and multiplied by the data/MC correction factor. This yields:

$$N_{\gamma\gamma}^{\text{CP}} = \text{CF}_{\text{CP}} \times N_{\gamma\gamma} \times \frac{\mathcal{L}_{\text{data}}}{\mathcal{L}_{\text{MC}}} = 76 \pm 14. \quad (5.1)$$

The uncertainty includes statistical and systematic uncertainties in the luminosity of the data, luminosity of the MC samples and correction factor.

Since the information on the initial state partons is available at the generator level, it is possible to access it and thus determine that 67 events are produced from the  $q\bar{q}$  initial state and 9 events from the  $gg$  initial state. The contribution to the invariant mass from each of the subprocesses separately and the fractional contribution with

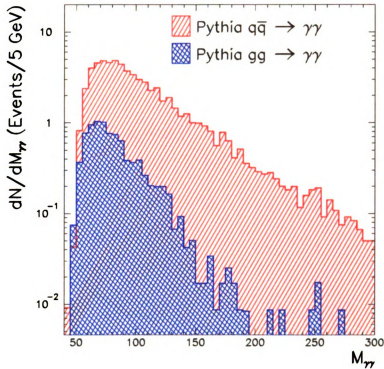


Figure 5.1:  $\gamma\gamma$  contribution from  $q\bar{q} \rightarrow \gamma\gamma$  and  $gg \rightarrow \gamma\gamma$  in the Central-Plug diphoton sample.

respect to the invariant mass are shown in figures 5.1 and 5.2. We observe that the magnitude of the  $gg$  subprocess is comparable to the  $q\bar{q}$  subprocess at low mass but falls off more steeply at large mass due to the rapidly decreasing  $gg$  parton-parton luminosity.

### 5.3 Purity of the Central-Plug Diphoton Sample

The majority of photon candidates in the CP diphoton sample are neutral mesons ( $\pi^0, \eta, K_S^0$ ) decaying to multiple photons that fake the direct photon signature. One approach to evaluate the fake contribution is to rely on the Pythia+QFL simulation

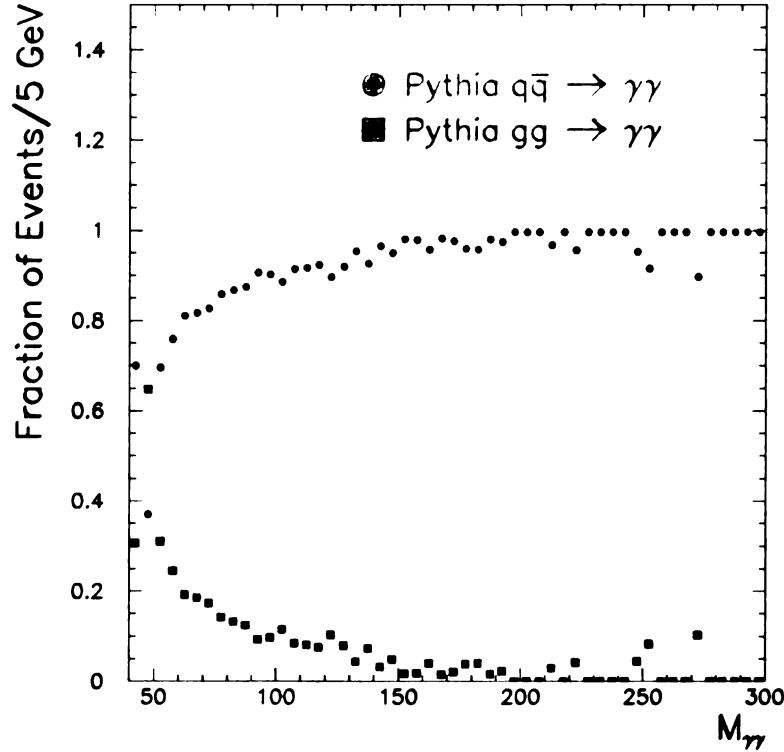


Figure 5.2: Fractional contribution from  $q\bar{q} \rightarrow \gamma\gamma$  and  $gg \rightarrow \gamma\gamma$  in the Central-Plug diphoton sample.

and generate events with  $\gamma + jet$  and  $jet + jet$  in the final state and apply the diphoton selection to the Monte Carlo samples, following the same method described in section 5.2. However it is very unlikely for jets to fake high energy photons and hence a large number of jets must be generated to collect a statistically significant jet background sample (jet background is nevertheless very large due to the very large production cross section). This is especially true for the  $jet + jet$  background, where both jets fake a photon. In this case generator and detector level simulations are very time consuming and hence it is unrealistic to rely on simulation alone. Alternatively, the fake contribution can be estimated by using the *conversion* and *profile methods* [23].

These methods rely on the CPR and CES chambers and, on statistical grounds, can discriminate between jets and photons. However these chambers do not extend to the plug, thus conversion and profile methods alone do not provide the necessary tools to discriminate photons in the plug. In the rest of this section, after a brief overview on the conversion and profile methods, we explain how the purity of the Central-Plug sample is determined.

The conversion and profile methods (also referred to as CPR and CES methods) rely on the property of the photon shower profile and conversion probability and how these differ from jets. The CPR or conversion method relies on the probability of a particle to convert in the solenoid magnet. Prompt photons have a lower probability to convert than photons from the decay of a neutral meson. The average conversion probability for photons is  $\sim 60\%$ , while for  $\pi^0 \rightarrow \gamma\gamma$  the probability is  $\sim 84\%$ . The CES or profile method uses the transverse shower profile of test beam electrons and compares it to the shower profile of the photon candidate. Since electrons and photons produce narrower showers than neutral mesons, a fit is performed to quantify the difference between the test beam electron shower and the shower of the photon candidate. If the fit yields a poor  $\chi^2$ , then the conclusion is that most likely the photon candidate is a neutral meson, otherwise a good  $\chi^2$  favors the photon hypothesis. The profile method is a very good discriminator of the background however is less powerful at high  $E_T$  where it is more difficult to resolve photons from a decay. This method is used up to  $E_T = 35$  GeV. At higher energies, the conversion method is employed. The advantage of the conversion method is the unlimited energy range in which it can be used and the low systematic uncertainty associated with it.

These techniques provide a probability or *weight* for each events that quantifies how consistent the candidate signature is with the photon or background hypothesis. Since the CES and CPR methods only provide statistical information it is not possible

to discriminate on an event by event basis which event constitutes signal and which belongs to the background.

The method used to extract the purity of the sample is explained in the rest of this section.

Accordingly to whether the central or plug cluster or both are direct photons or fakes, for each event in the CP sample there are four possible outcomes:

1. both clusters are photons ( $N_{\gamma\gamma}^{CP}$ )
2. the central cluster is a photon and the plug cluster is a fake ( $N_{\gamma f}^{CP}$ )
3. the central cluster is a fake and the plug cluster is a photon ( $N_{f\gamma}^{CP}$ )
4. both clusters are fakes ( $N_{ff}^{CP}$ )

$N_{\gamma\gamma}^{CP}$  is the Standard Model diphoton contribution to the sample and has been evaluated in section 5.2.  $N_{ff}^{CP} + N_{f\gamma}^{CP} + N_{\gamma f}^{CP}$  is the fake contribution to the sample.

### 5.3.1 $N_{ff}^{CP} + N_{f\gamma}^{CP}$ Estimate

The CES and CPR chambers do not extend to the plug and thus these techniques cannot be used to discriminate the case in which the plug cluster is a fake. However, by applying the conversion and profile techniques described above to the central cluster (we refer to this method as single arm weighting), one can compute (statistical error only):

1.  $N_{\gamma}^{CP} = N_{\gamma\gamma}^{CP} + N_{\gamma f}^{CP}$  (central cluster is a photon) =  $108 \pm 27$
2.  $N_f^{CP} = N_{ff}^{CP} + N_{f\gamma}^{CP}$  (central cluster is a fake) =  $84 \pm 26$

Table 5.1: Systematic uncertainties from CES and CPR weighting. The total systematic error is determined by adding the contributions in quadrature.

Source of Systematic	Events	Shift from Nominal
Nominal	$84 \pm 26$	-
CPR Hit Rate	$82 \pm 26$	2
CPR Backscattered Showers	$96 \pm 25$	12
CPR $\eta, \pi^0$	$86 \pm 27$	2
CES	$81 \pm 25$	3
Total Systematic		13

where  $N_f^{CP}=84$  correspond to a fraction of  $0.44 \pm 0.11$  of the CP data sample. The systematic error on  $N_f^{CP}$  is obtained by varying the CES and CPR efficiencies by  $1\sigma$  and determining the shift from the nominal value of the number of fakes. The sources of the systematic uncertainties and the respective values as well as the total combined systematic uncertainty are listed in table 5.1.

### 5.3.2 $N_{\gamma f}^{CP}$ Estimate

To complete the fake estimate, the remaining piece yet to be evaluated is  $N_{\gamma f}^{CP}$ . The procedure used in this case differs from the method described above as the plug cluster cannot be sorted by the CES and CPR methods. We resort instead to a different methodology that relies on the assumption that the ratio between isolated and non-isolated jets is the same for jets both in dijet and diphoton samples. Since it is possible to derive the number of non-isolated jets from the data diphoton sample, one multiplies this last number by the ratio mentioned above to extract  $N_{\gamma f}^{CP}$ . It is fair to assume that the ratio between isolated to non-isolated jets is, for our purposes, independent on the physics process that produced the jets.

We use the University of Chicago dijet data sample [24]. The events in the sample are further required to have at least two jets with  $E_T > 10$  GeV,  $|\eta| < 2.2$ , and to have  $\Delta\phi_{jj} > 160^\circ$  with the purpose of cleaning up the sample to avoid, for instance, the energy of one of the jets affecting energy and isolation measurements of the other jet. Furthermore, one jet is required to be fiducial in the central region of the detector, with  $E_T > 22$  GeV, and have VTX occupancy and  $\chi^2$  consistent with a photon.

For jets in the dijet sample, one can measure:

$$R = \frac{N_J^{\text{iso}}}{N_J^{\text{non-iso}}} \quad (5.2)$$

where:

- $N_J^{\text{iso}}$  = number of events with plug clusters passing all plug cuts, including annulus isolation.
- $N_J^{\text{non-iso}}$  = number of events passing the plug selection, but failing the annulus isolation

We find that 102 events pass and 43 events fail the annulus isolation in the dijet sample. However, in addition to jets, there is a contribution coming from photons included in these subsets. We assume that the photon contamination in the non-isolated sample is negligible. The fraction of jets in the isolated sample is estimated by plotting the cone 0.4 isolation distribution and by assuming that the objects in the tail of the distribution are mostly jets. We fit the tail to a straight line using Minuit [25](see figure 5.3). As a cross-check that this assumption is reasonably correct, the isolation  $E_T$  in the cone of 0.4 for the plug jet candidates that failed the annulus cut (they are expected to be mostly jets) is plotted together with the straight line. These events are represented by circles in figure 5.3. We observe that the circles overlap fairly well along the straight line.

The number of events in the area underneath the straight line represents the number of jets in the isolated sample. We find that  $N_J^{\text{iso}} = 52 \pm 11$  (the uncertainty is from the fit). This yields:

$$R = \frac{N_J^{\text{iso}}}{N_J^{\text{non-iso}}} = \frac{52}{43} = 1.21 \pm 0.22. \quad (5.3)$$

Before we can compute  $N_{\gamma f}^{\text{CP}}$ , we need to estimate one more piece, i.e. the number of events in the diphoton sample in which the central cluster is a real photon while the plug cluster is a non-isolated jet. We first determine the number of events in the diphoton sample that pass the complete Central-Plug selection except the annulus isolation cut for the plug cluster. In this subset, there are 49 events in which the plug cluster fails the annulus isolation. However, among these 49 events there are events whose plug cluster is a real prompt photon even though it failed the annulus cut. We estimate the number of events with a plug photon in the non-isolated subset by using the following formula:

$$N_{\gamma}^{\text{non-iso}} = \frac{1 - \epsilon_{\gamma}}{\epsilon_{\gamma}} \times N_{\gamma}^{\text{iso}}, \quad (5.4)$$

that can be easily derived from the definition of efficiency:

$$\epsilon_{\gamma} = \frac{N_{\gamma}^{\text{iso}}}{N_{\gamma}^{\text{iso}} + N_{\gamma}^{\text{non-iso}}}, \quad (5.5)$$

where  $\epsilon_{\gamma}$  is the efficiency for a plug photon to pass the annulus isolation cut,  $\epsilon_{\gamma} = (0.891 \pm 0.006)$ ,  $N_{\gamma}^{\text{iso}}$  is the number of  $\gamma\gamma$  events passing the annulus isolation cut and  $N_{\gamma}^{\text{non-iso}}$  is the number of  $\gamma\gamma$  events failing the annulus isolation cut.  $N_{\gamma}^{\text{iso}}$  was estimated in section 5.2 ( $N_{\gamma}^{\text{iso}} = 76$  events) and thus  $N_{\gamma}^{\text{non-iso}} = 9 \pm 1$  events. This yields  $N_{\gamma f \text{ non-iso}}^{\text{CP}} = 49 - 9 = 40 \pm 7$ .  $N_{\gamma f}^{\text{CP}}$  can now be determined:

$$N_{\gamma f}^{\text{CP}} = N_{\gamma f \text{ iso}}^{\text{CP}} = R \times N_{\gamma f \text{ non-iso}}^{\text{CP}} = 48 \pm 12 \quad (5.6)$$

Finally, we determine the efficiency for the annulus isolation cut in rejecting jets:

$$\epsilon = \frac{N_J^{\text{non-iso}}}{N_J^{\text{non-iso}} + N_J^{\text{iso}}} = \frac{43}{43 + 52} = 45.3\% \quad (5.7)$$



### 5.3.3 Central-Plug Fake Estimate-Summary

We have evaluated the different pieces that together make up the contribution from fakes in the Central-Plug sample. This yields the total fake contribution:

$$(N_{\text{ff}}^{\text{CP}} + N_{f\gamma}^{\text{CP}}) + N_{\gamma f}^{\text{CP}} = (84) + 48 = 132 \pm 31. \quad (5.8)$$

The uncertainties have been added in quadrature.

By employing the  $\gamma + \text{jet}$  Monte Carlo sample introduced in section 5.3.4, one can estimate  $N_{f\gamma}^{\text{CP}} \sim 16$  events. Thus:

$$N_{f\gamma}^{\text{CP}} + N_{\gamma f}^{\text{CP}} \sim 16 + 48 = 64 \text{ events} \quad (5.9)$$

$$N_{\text{ff}}^{\text{CP}} = (N_{ff}^{\text{CP}} + N_{f\gamma}^{\text{CP}}) - N_{f\gamma}^{\text{CP}} \sim (84) - 16 = 68 \text{ events} \quad (5.10)$$

Therefore the fake contribution in the CP diphoton sample consists approximately of a 50%-50% mixture of  $\gamma + \text{jet}$  and  $\text{jet} + \text{jet}$  events.

### 5.3.4 Shape of the Fake Invariant Mass Distribution

Finally, we shall determine the shape of the invariant mass distribution for the fakes. The shape of the invariant mass for the  $N_{\gamma f}^{\text{CP}} + N_{f\gamma}^{\text{CP}}$  contribution is simulated with Pythia+QFL. The 2 $\rightarrow$ 2 Standard Model processes that generate one prompt photon and one jet in the final state at leading order are:

- $q\bar{q} \rightarrow g\gamma$
- $qg \rightarrow q\gamma$
- $gg \rightarrow g\gamma$

We generate  $800\text{pb}^{-1}$  of  $\gamma + \text{jet}$  events with Pythia choosing CTEQ5M structure functions and pass them through the detector simulation. We apply the central cuts

to  
in  
of  
  
fa  
at  
of  
by  
be  
th  
in  
Si  
sh

## 5.

In  
5.3  
ce  
Ce  
de  
cas

to these events and require at least one fiducial plug cluster with  $E_T > 22$  GeV. The invariant mass distribution of the MC events that survive the selection is the shape of the  $N_{\gamma f}^{CP} + N_{f\gamma}^{CP}$  fake contribution.

The shape of the invariant mass spectrum for events in which both clusters are fakes is not determined by simulating Monte Carlo *jet+jet* events. As it was discussed at the beginning of this section, it turns out that it would take an unrealistic amount of time to generate a sample with a good statistical significance. Instead, we proceed by multiplying the  $\gamma + jet$  shape by a mass dependent factor. This factor is the ratio between the  $\pi^0\pi^0$  and the  $\gamma\pi^0$  cross sections calculated at leading order [26] where the same cuts, including the isolation, that we use to select the events are reproduced in the code. This ratio as a function of the invariant mass is shown in figure 5.4. Since  $\pi^0$ 's are the main contribution to the fakes, we take this rescaled shape as the shape of the *jet + jet* contribution to the fakes.

### 5.3.5 Performance of the Single Arm Weighting Method for Central Diphotons

In order to test the validity of the single arm subtraction method described in section 5.3, we apply it to determine the fake background in a data control sample containing central diphotons. This sample is selected from the same initial data set as the Central-Plug sample and should not be confused with the Central-Central sample described in chapter 4. We proceed in the same way as we did in the Central-Plug case with the following correspondence:

- Lower  $\eta$  cluster in CC sample  $\rightarrow$  central cluster in CP sample.
- Higher  $\eta$  cluster in CC sample  $\rightarrow$  plug cluster in CP sample.

There are 248 events passing the central and the appropriate plug-like selection <sup>1</sup>.

As in the CP case, the contributions to the sample are:

1. QCD  $\gamma\gamma$ : SM processes that produce direct diphoton events ( $q\bar{q} \rightarrow \gamma\gamma$  and  $gg \rightarrow \gamma\gamma$ ).
2. Fakes: the background coming from neutral mesons ( $\pi^0, \eta, K_S^0$ ) decaying to multiple photons.

The QCD  $\gamma\gamma$  contribution is determined by using the same MC sample described in section 5.2, accepting only events where the low  $\eta$  cluster passes the same central selection as in the CP case and the high  $\eta$  cluster passes a plug-like selection. Rescaling to the luminosity of the data and multiplying by the appropriate correction factor, we find that the SM  $\gamma\gamma$  contribution is 76 events.

Consistently with the CP case, the fake background is broken into two components:

- $N_f^{CC} = N_{f\gamma}^{CC} + N_{ff}^{CC}$ : the low eta cluster is a fake, regardless to whether the high eta cluster is a fake or a real photon.
- $N_{\gamma f}^{CC}$ : the low eta cluster is a real photon and the high eta cluster is a fake.

The number of events whose low eta cluster is a fake is determined with the CES and CPR weighting techniques (to be consistent with what is done in the Central-Plug case, the CES/CPR method is only applied to one leg). This yields:

1.  $N_\gamma^{CC} = 151 \pm 26$

2.  $N_f^{CC} = 97 \pm 25$

---

<sup>1</sup>The  $\chi_{avg}^2$  cut is used in place of the  $3 \times 3 \chi^2$  cut and the central HAD/EM sliding cut in place of the plug HAD/EM sliding cut.

where  $N_f^{CC} = N_{f\gamma}^{CC} + N_{ff}^{CC}$ .  $N_f^{CC}$  corresponds to a fraction of 0.39 of the sample.

Finally, to determine  $N_{\gamma f}^{CC}$ , we use the dijet sample to determine the ratio of isolated/non-isolated jets, in the same way as it was done in the CP case and, from there, we can estimate the isolated jet contribution in the central diphoton sample. In the dijet sample, we select a central cluster passing the plug-like selection, except for the annulus isolation. There are 318 events left, among which 241 pass the annulus isolation cut and 104 fail. Out of the 241 events, we determine that there are  $135.5 \pm 14$  jet events (the fit is shown in figure 5.5). Thus the ratio isolated/non-isolated jets in the central case is:

$$R = \frac{N_j^{\text{iso}}}{N_j^{\text{non-iso}}} = \frac{135.5}{104} = 1.3 \pm 0.2 \quad (5.11)$$

Assuming the same ratio isolated/non-isolated jets in the  $\gamma\gamma$  sample yields:

$$N_{\gamma f}^{CC} = N_{\gamma f^{\text{iso}}}^{CC} = R \times N_{\gamma f^{\text{non-iso}}}^{CC} \quad (5.12)$$

There are 78 non-isolated events in the CC diphoton sample. Among these events, 9 are non-isolated photons and thus are subtract. One finds:

$$N_{\gamma f^{\text{non-iso}}}^{CC} = 69 \Rightarrow N_{\gamma f}^{CC} = 90 \pm 18 \quad (5.13)$$

In summary, the single arm subtraction yields the following contributions:

1.  $N_{\gamma\gamma}^{CC} = 79 \pm 9$
2.  $N_f^{CC} = N_{f\gamma}^{CC} + N_{ff}^{CC} = 97 \pm 25$
3.  $N_{\gamma f}^{CC} = 90 \pm 18$

As both clusters are central, the CES/CPR techniques can be used as an independent method to determine  $N_{\gamma\gamma}^{CC}$  (double arm weighting). We find:

1.  $N_{\gamma\gamma}^{CC} = 70.6 \pm 40.7$
2.  $N_f^{CC} = N_{f\gamma}^{CC} + N_{ff}^{CC} = 99.5 \pm 54.71$
3.  $N_{\gamma f}^{CC} = 77.9 \pm 41.8$

These numbers are in good agreement with the single arm weighting estimates.

For completeness, in figure 5.6 the data sample (248 events) invariant mass distribution overlapped to the SM  $\gamma\gamma$  and fakes (from single arm weighting) contributions are shown. We find good agreement between the data and the SM  $\gamma\gamma$  + fakes prediction.

Since single and double arm weighting yield the same fake prediction, we conclude that the method used to extract the fraction of fakes in the CP diphoton sample is reliable.

## 5.4 Central-Plug Background Summary

In table 5.2 we summarize the predicted number of events from SM  $\gamma\gamma$  and fake sources and their combined value. In figure 5.7 the SM  $\gamma\gamma$  and fake contributions are superimposed to the data. We observe good agreement between the data and the estimate of the background.

## 5.5 Background in the Central-Central Diphoton Sample

The background study for the CC diphoton sample is referenced in [18, 27].

The authors employ the conversion and profile methods to measure the purity of the sample. The result is that  $64 \pm 11 \pm 19\%$  of the sample, which corresponds

Table 5.2: Summary of predicted and observed events in the Central-Plug diphoton sample.

Contribution	Events
$N_{\gamma\gamma}^{CP}$	$76 \pm 14$
$N_{ff}^{CP} + N_{f\gamma}^{CP}$	$84 \pm 29$
$N_{\gamma f}^{CP}$	$48 \pm 12$
Total predicted	$208 \pm 34$
CP data	192

to  $183 \pm 54 \pm 32$  events, consists of fake background. The invariant mass spectrum of these events is determined by the invariant mass distribution of events in the diphoton data sample that have one of both photon candidates failing the isolation cut while surviving the other selection criteria. Since isolation is a highly efficient criteria in discriminating photons from jets, the non-isolated sample is expected to contain mostly jets. This method is not employed in the CP background study as corresponding CP non-isolated sample has very low statistics.

The SM contribution to diphoton production in the CC diphoton sample is measured by using Pythia+QFL simulation. This study predicts  $96 \pm 31$  SM prompt diphotons in the CC diphoton sample.

In summary, the prediction for fakes plus SM prompt diphotons in the Central-Central diphoton sample consists of  $280 \pm 66$  events. This result is in good agreement with the 287 events observed in the data sample.

## 5.6 Combined CC+CP Diphoton Sample - Background

The invariant mass distribution for the 479 events in the CC+CP diphoton sample together with the fake and SM diphoton contributions are displayed in figure 5.8.

We conclude that the measured diphoton data is well-modeled by the fakes plus SM diphoton predictions and no excess is observed.



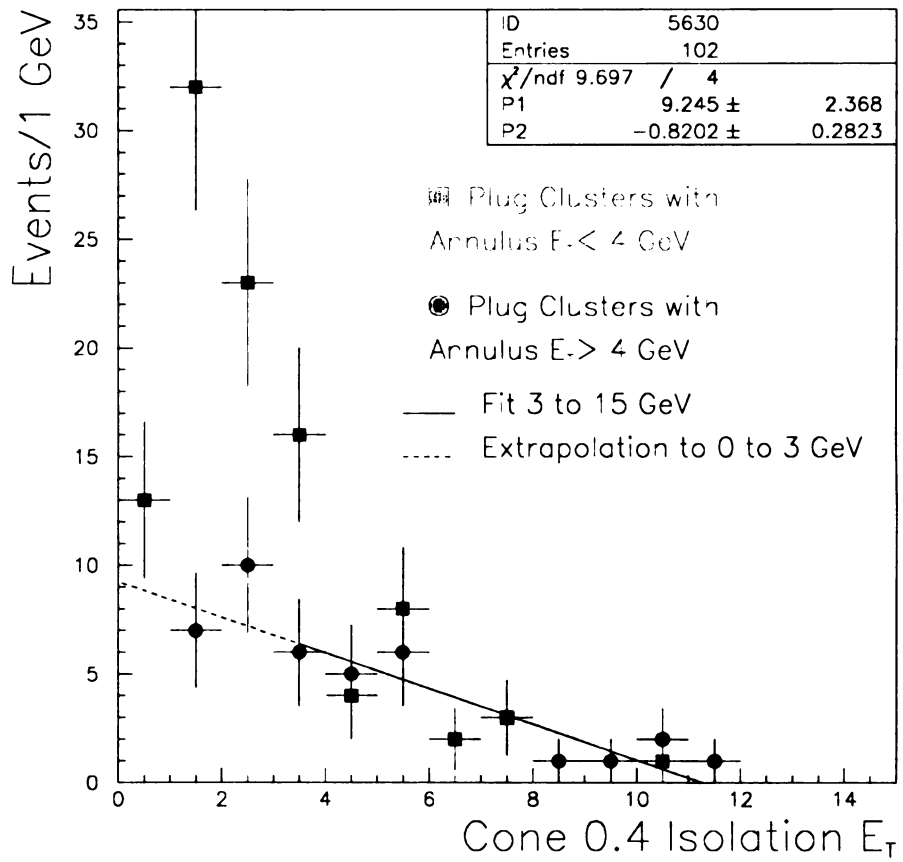


**Figure 5.3:** Cone 0.4 isolation distribution for jets in the dijet sample that pass the annulus isolation cut in the Central-Plug diphoton sample.

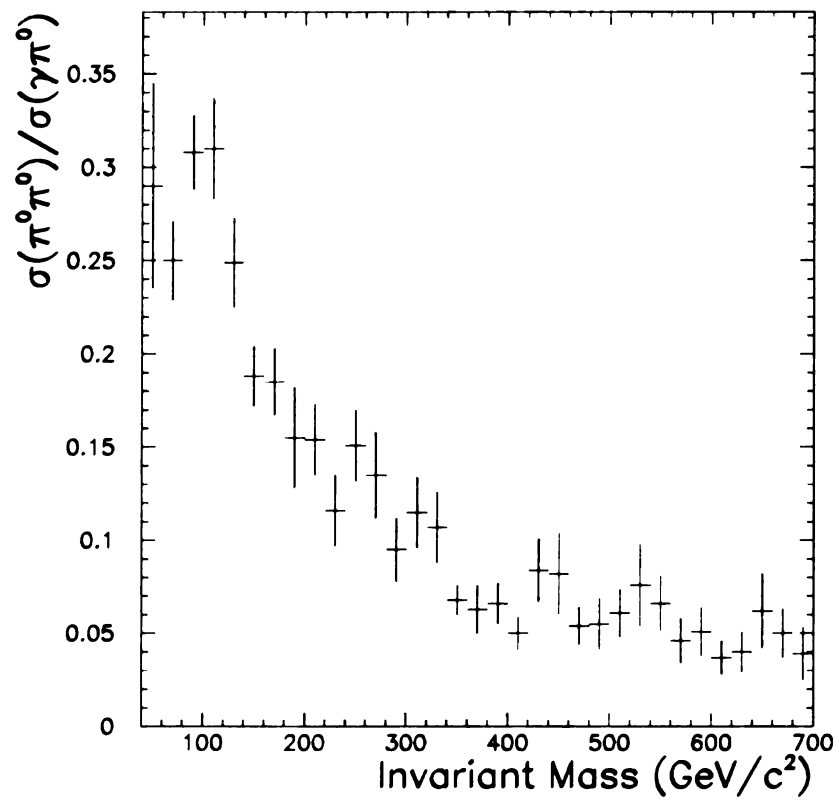


**Figure 5.4:** Ratio between the  $\pi^0\pi^0$  and  $\gamma\pi^0$  cross sections versus the invariant mass of the pair.

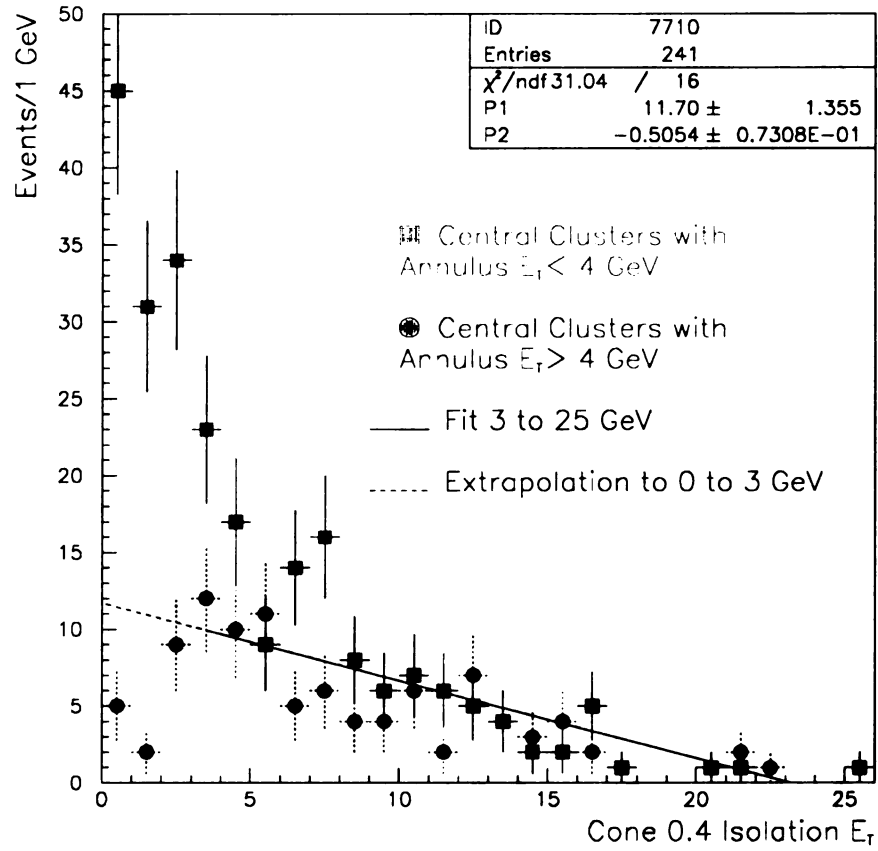


**Figure 5.5:** Cone 0.4 isolation distribution for jets in the dijet sample that pass the **annulus** isolation cut in the sample containing central diphotons.

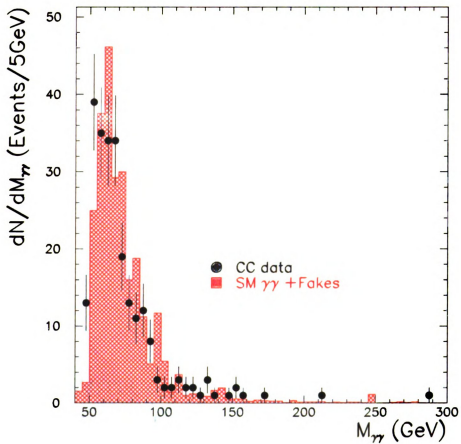


**Figure 5.6:** Combined SM  $\gamma\gamma$ +fake contribution in the control diphoton sample.

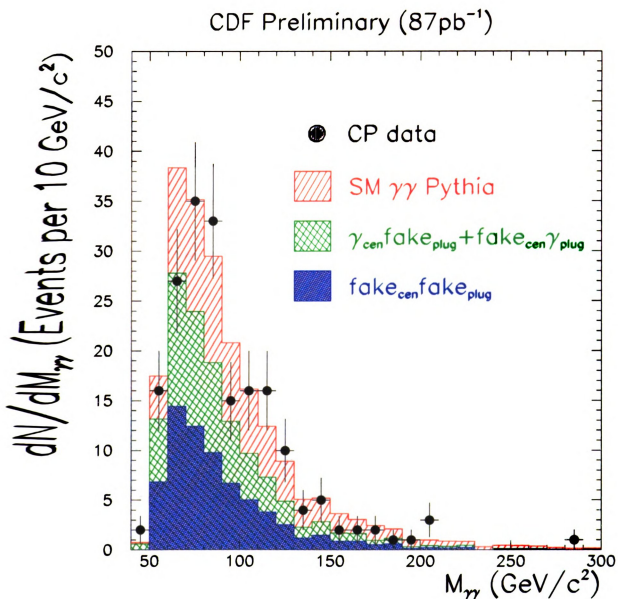


**Figure 5.7:** SM  $\gamma\gamma$  and fake contributions in the Central-Plug diphoton sample.

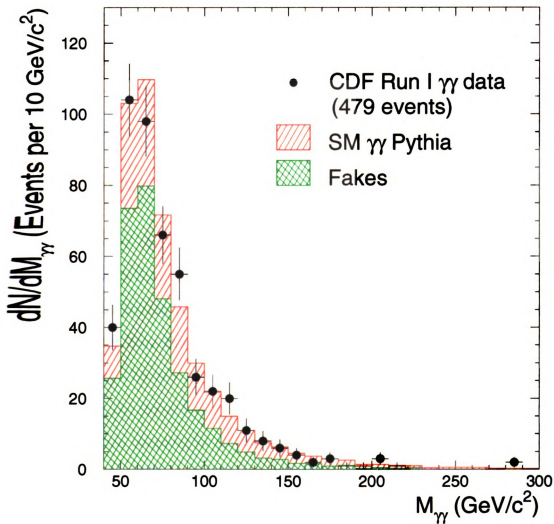


**Figure 5.8:** SM  $\gamma\gamma$  and fake contributions in the combined Central-Plug and Central-Central diphoton sample.

# Chapter 6

## Limit on Large Extra Dimensions with Central-Plug Diphotons

### 6.1 Introduction

**In** the previous chapter we concluded that the inclusive diphoton data is in good **agreement** with Standard Model diphoton and fake predictions and hence no excess **that** could be attributed to LED diphoton production is observed. However, there is **much** to learn from this result. In particular, it is possible to exclude LED up to a **certain** scale. The next step is, in fact, to set a limit on Large Extra Dimensions by **determining** the lower bound on the parameter  $M_S$  that characterizes the strength **of** the graviton coupling to all particles (see chapter 2). Since the magnitude of  $M_S$  **determines** the number of predicted diphotons from LED graviton exchange processes (**the** larger is  $M_S$ , the fewer are the events expected from LED sources) it is possible **to** set a limit on  $M_S$  by comparing the invariant mass shape of the CDF diphoton **data** to the the background (this includes fakes as well as diphoton events from **Standard** Model processes) plus LED signal invariant mass spectrum with constraints **on** the predicted number of diphoton and fake events and on the total number of **events** observed. This is achieved by constructing a likelihood function. This function **calculates** how consistent the existing CDF data is with LED diphoton production

by fitting the LED+background shapes to the data. In this chapter we will describe the method in detail.

## 6.2 $p\bar{p} \rightarrow \gamma\gamma X$ Differential Cross Section

As already mentioned in chapter 2, the differential cross section for inclusive diphoton production  $p\bar{p} \rightarrow \gamma\gamma X$  in the presence of large extra dimensions can be written as:

$$\frac{d^2\sigma}{dM_{\gamma\gamma}} = \left. \frac{d^2\sigma}{dM_{\gamma\gamma}} \right|_{SM} + \eta \left. \frac{d^2\sigma}{dM_{\gamma\gamma}} \right|_{INT} + \eta^2 \left. \frac{d^2\sigma}{dM_{\gamma\gamma}} \right|_{KK}, \quad (6.1)$$

where  $\eta = \lambda/M_S^4$ . In chapter 2 it was also pointed out that  $\lambda$  is a parameter of order one and its value depends on the choice of the notation, and so does the value of  $M_S$ . Conversely,  $\eta$  is convention independent. We proceed by first setting a limit on  $\eta$  and eventually translating it into a limit on  $M_S$  in the more popular conventions. It has been demonstrated that the method yields the same result whether the likelihood function is written as a function of  $\eta$  or as a function of  $M_S$ .

A very important feature of equation 6.1 is that the  $\eta$  dependence in the cross section can be factored out, thus the shape of the different components - SM, interference, and direct KK - are fixed while their relative normalization varies according to powers of  $\eta$ . These curves are part of the input in the unbinned likelihood function described in section 6.3, thus the next step is to parameterize these shapes.

### 6.2.1 SM $\gamma\gamma$ and Fakes Mass Spectra

The SM  $\gamma\gamma$  and fake contributions to the Central-Plug sample have been determined in chapter 5. The  $\gamma\gamma$  contribution is fitted with a function that is the product of a turn-on curve and the sum of two exponentials:

$$SM(M_{\gamma\gamma}) = \frac{1}{4} \times \left[ \tanh \frac{(M_{\gamma\gamma} - a_1)}{a_2} + 1 \right] \times \left[ \tanh \frac{(M_{\gamma\gamma} - a_3)}{a_4} + 1 \right] \times (b_1 \times \exp^{b_2 M_{\gamma\gamma}} + b_3 \times \exp^{b_4 M_{\gamma\gamma}}), \quad (6.2)$$



where the parameters of the turn-on curve are:

- $a_1 = 76 \pm 13$
- $a_2 = 29 \pm 31$
- $a_3 = 55 \pm 15$
- $a_4 = 5 \pm 13$

and the parameters in the two exponentials are displayed in figure 6.2. The turn-on curve mimics the  $E_T$  threshold that yields the cutoff at the low end of the invariant mass distribution, while the exponentials provide a functional form suitable to describe the falling tail at higher mass. The turn-on parameterization is determined by fitting the ratio between the diphoton invariant mass spectrum for events that pass the diphoton selection and the diphoton invariant mass spectrum for the events that pass the same selection but with a looser  $E_T$  cut of 10 GeV (see figure 6.1). In figure 6.2 the overall fit to the SM  $\gamma\gamma$  mass spectrum is shown.

The shape of the mass spectrum for  $\gamma + jet$  events is obtained by fitting the invariant mass distribution of the  $\gamma + jet$  Monte Carlo events described in section 5.3. The functional form of the curve is the same as for the  $\gamma\gamma$  case, i.e. the product of the same turn-on curve and two exponentials. In figure 6.3 the fit as well as the fit parameters for the two exponentials are displayed. Finally, the  $jet + jet$  contribution is extracted by simply multiplying the  $\gamma + jet$  parameterization by the ratio between the  $\pi^0\pi^0$  and the  $\gamma\pi^0$  cross sections calculated at leading order (see section 5.3).

### 6.2.2 The LED Monte Carlo Samples

In order to generate LED events, we use the Monte Carlo program VDEC-ED, written by Ulrich Baur and implemented in Pythia by D. Gerdes and D. Berebitsky [27].

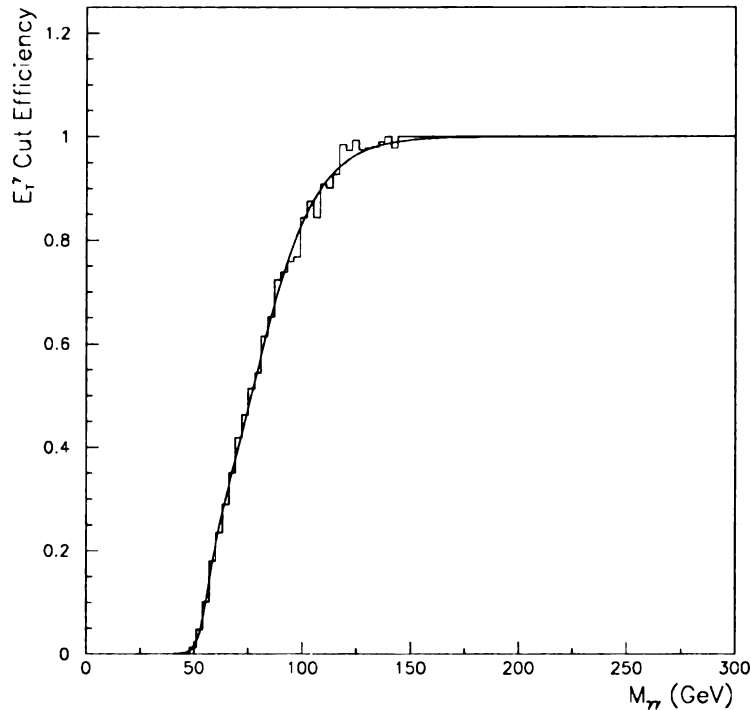


Figure 6.1: Turn-on curve.

**C**urrently this program includes the matrix elements for direct SM diphoton production with  $q\bar{q}$  in the initial state, direct KK graviton exchange diphoton production at leading order with  $q\bar{q}$  and  $gg$  initial states, as well as the matrix element for the interference between the SM and LED diphoton production processes with  $q\bar{q}$  in the initial state but it does not include the interference between the  $gg$  SM and LED initial states. However the overlap between LED and SM processes is expected to be small (see section 2.4) and so is the contribution to the cross section. Nevertheless a conservative estimate of this contribution will be given while discussing uncertainties and will be incorporated into the limit as a systematic effect.

We generate 200000 events for the interference and direct KK terms separately

and simulate the detector response with QFL. These events are generated by choosing  $\eta = 10^{-12} \text{ GeV}^{-4}$ . Subsequently, the same selection used to select the Central-Plug diphoton Monte Carlo events is applied, that is the same selection used in the data except for cuts on the variables that are poorly modeled by QFL.

The invariant mass distributions of these events are shown in figure 6.4 for the interference and in figure 6.5 for the KK contribution. As we mentioned in section 6.2, the shape of the invariant mass distribution for both the KK and the interference components is independent of  $\eta$ . In light of this, we fit these shapes and factor out the  $\eta$  dependence by dividing the interference component by  $\eta$  and the KK component by  $\eta^2$ , where  $\eta = 10^{-12} \text{ GeV}^{-4}$ , corresponding to the choice  $M_S = 1000 \text{ GeV}$  (in Hewett convention) with which the events were generated. The resulting curves, when multiplied by a different value of the parameter  $\eta$  for the interference and  $\eta^2$  for the KK component, reproduce the appropriate invariant mass distributions corresponding to this new choice.

We proceed by fitting the interference term with a function that is the product of the turn-on curve introduced in 6.2.1, an additional turn-on curve and one exponential. Similarly, the KK mass spectrum is fitted by the product of two turn-on curves and the sum of three gaussians. The fits are displayed in figures 6.4 and 6.5. We observe that the shape of the KK term falls off at high mass due to the decreasing parton luminosities.

## 6.3 Likelihood Function

To determine how consistent the data is with the LED hypothesis and hence set a limit on  $\eta$ , the following unbinned likelihood function is employed:

$$L = \frac{1}{\sqrt{2\pi}\sigma_b} e^{-\frac{(N_b - n_b)^2}{2\sigma_b^2}} \times \frac{1}{\sqrt{2\pi}\sigma_{SM}} e^{-\frac{(N_{SM} - n_{SM})^2}{2\sigma_{SM}^2}} \times$$

$$\frac{(n_{SM} + n_{INT}(\eta) + n_{KK}(\eta) + n_b)^{N_0} e^{-(n_{SM} + n_{INT}(\eta) + n_{KK}(\eta) + n_b)}}{N_0!} \times \prod_{i=1}^{N_0} \frac{n_{SM} f_{SM}(M_i) + n_{INT}(\eta) f_{INT}(M_i) + n_{KK}(\eta) f_{KK}(M_i) + n_b f_b(M_i)}{n_{SM} + n_{INT}(\eta) + n_{KK}(\eta) + n_b} \quad (6.3)$$

There are three free parameters in the fit:  $\eta = \lambda/M_S^4$ ,  $n_{SM}$  and  $n_b$ .  $n_{SM}$  and  $n_b$  are fit parameters respectively for the number of SM  $\gamma\gamma$  events and for the number of fakes. The other parameters are:

- $N_0 = 192$  is the total number of events in the Central-Plug data sample.
- $N_{SM} = 76$  is the predicted number of SM  $\gamma\gamma$  events;  $\sigma_{SM} = 14$  is the uncertainty on the SM  $\gamma\gamma$  estimate (see equation 5.1).
- $N_b = 132$  is the predicted number of fakes;  $\sigma_b = 31$  is the uncertainty on the fake estimate (see equation 5.8).
- $n_{INT}(\eta)$  and  $n_{KK}(\eta)$  are the predicted number of LED  $\gamma\gamma$  events for a given  $\eta$ .

The  $\eta$  dependence is displayed in the next equation:

$$n_{LED}(\eta) = n_{INT}(\eta) + n_{KK}(\eta) = C_{INT} \times \eta + C_{KK} \times \eta^2, \quad (6.4)$$

where  $C_{INT}$  and  $C_{KK}$  are constants. These constants are computed by first evaluating the number of interference (KK) LED events for a chosen value of  $\eta$ ,  $\eta_{gen} = 10^{-12} \text{GeV}^{-4}$ , and subsequently dividing it by  $\eta_{gen}$  ( $\eta_{gen}^2$ ) to factor out the  $\eta$  dependence:

$$C_{INT} = \mathcal{L} \times \sigma_{INT}(\eta_{gen}) \times \text{CF}_{CP} \times \text{ACC}_{INT} \times \frac{1}{\eta_{gen}} \quad (6.5)$$

$$C_{KK} = \mathcal{L} \times \sigma_{KK}(\eta_{gen}) \times \text{CF}_{CP} \times \text{ACC}_{KK} \times \frac{1}{\eta_{gen}^2} \quad (6.6)$$

where:

- $\mathcal{L} = 87\text{pb}^{-1}$  is the luminosity of the data.
  - $\text{CF}_{\text{CP}} = 0.602$  is the correction factor for the CP selection from equation 4.18.
  - $\sigma_{\text{INT}}(\eta_{\text{gen}}) = 0.08278\text{pb}$  is the cross section for the interference component evaluated by VDEC\_ED for  $\eta = \eta_{\text{gen}} = 10^{-12}\text{GeV}^{-4}$ .
  - $\sigma_{\text{KK}}(\eta_{\text{gen}}) = 0.02225\text{pb}$  is the cross section for the KK component evaluated by VDEC\_ED for  $\eta = \eta_{\text{gen}} = 10^{-12}\text{GeV}^{-4}$ .
  - $\text{ACC}_{\text{INT}} = 0.16$  is the acceptance $\times$ efficiency for LED events from the interference component for  $\eta = \eta_{\text{gen}} = 10^{-12}\text{GeV}^{-4}$ .
  - $\text{ACC}_{\text{KK}} = 0.09$  is the acceptance $\times$ efficiency for LED events from the KK component for  $\eta = \eta_{\text{gen}} = 10^{-12}\text{GeV}^{-4}$ .
- $M_i$  is the invariant mass value for the  $i$ th event in the Central-Plug data sample.
  - $f_b(M_i)$  is the function representing the shape of the invariant mass distribution for fakes. The parameterization was determined in section 6.2.1 and has been divided by a normalizing factor.
  - $f_{\text{SM}}(M_i)$ ,  $f_{\text{INT}}(M_i)$ ,  $f_{\text{KK}}(M_i)$  are the shapes of the  $\gamma\gamma$  components, SM and LED. The parameterizations were determined in sections 6.2.1 and 6.2.2 and have been divided by a normalizing factor.

**The** first two terms in the likelihood provide constraints on the predicted number of **SM** events in the data sample: the first term is a gaussian constraint on the number of **fakes**; the second term is a gaussian constraint on the number of predicted  $\gamma\gamma$  events. **The** third term is a Poisson constraint on the total number of events observed. **The** last term in the equation is a shape factor and is evaluated for each of the 192 values **of** the invariant mass for the events in the CP data. By minimizing the likelihood

function via Minuit in presence of extra dimensions, the fitter searches for the value of  $\eta$  that best incorporates LED events into the data consistently with the predicted shapes.

In section 6.4 the performance of the likelihood fit is tested by assuming the existence of extra dimensions leading to graviton mediated diphoton production. Since no excess is observed in the diphoton data sample, the likelihood fit provides a tool to set a limit on  $\eta$  as it will be explained in section 6.5.

## 6.4 Performance of the Fitter

In order to test the performance of the likelihood fit, we generate 5000 pseudoexperiments assuming extra dimensions with  $\eta^{true}=7.716\times 10^{-12}\text{GeV}^{-4}$ , corresponding to  $M_S^{true} = 600 \text{ GeV}$  in Hewett convention. Each pseudoexperiment is simulated by generating fakes as well as SM+LED  $\gamma\gamma$  events according to the shapes determined by the fits discussed in section 6.2. For each pseudoexperiment, the number of events for each contribution is randomly generated according to a Poisson distribution. The mean of the Poisson distribution is also randomly generated with a gaussian distribution whose mean is the predicted number of events and is smeared with the uncertainty of the prediction. The invariant mass distributions for some of the pseudoexperiments are shown in figure 6.6 for  $\lambda = -1$  and figure 6.7 for  $\lambda = +1$ .

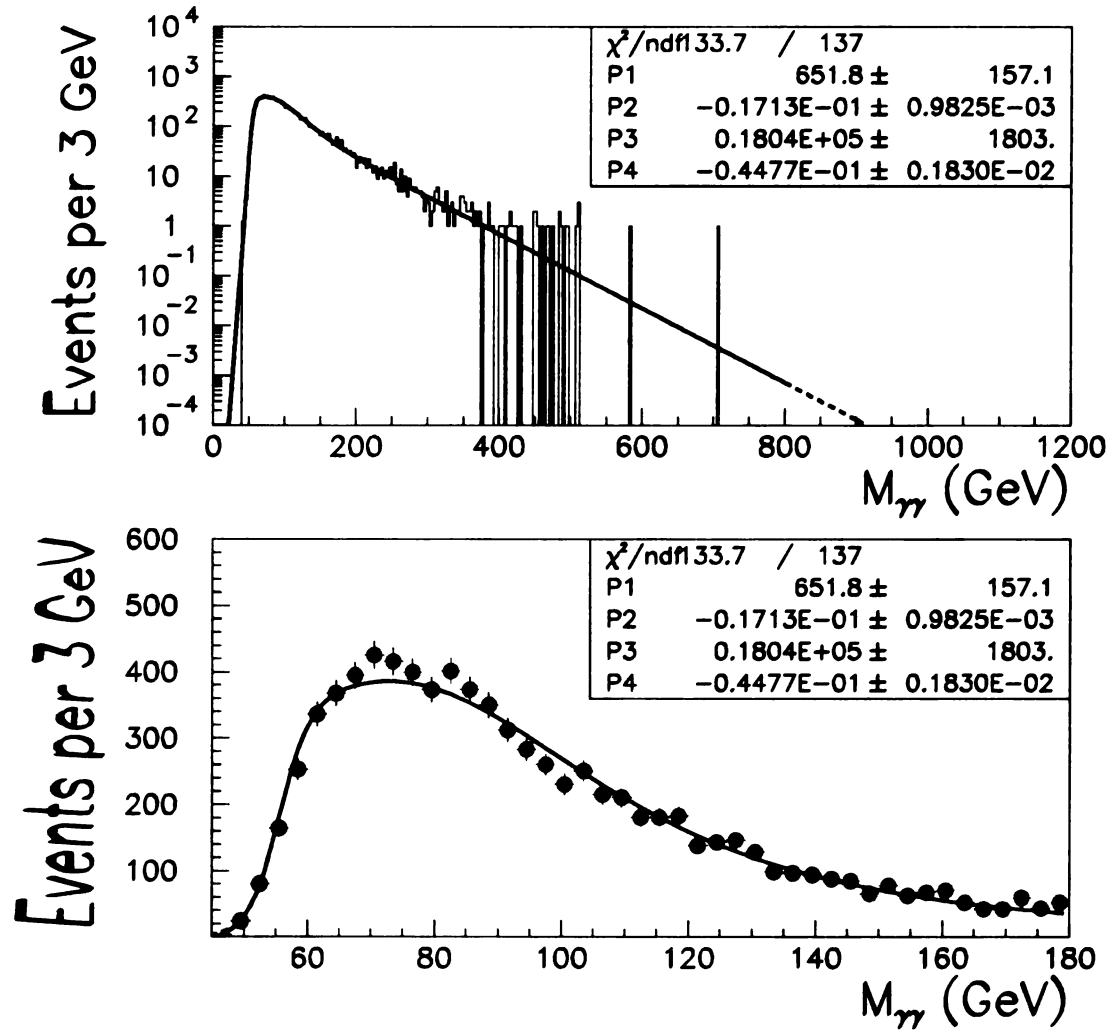


**Figure 6.2:** Top: Invariant mass distribution for the Monte Carlo SM  $\gamma\gamma$  events after the CP selection has been applied. The solid line is a fit of the distribution. Bottom: close up in linear scale of the peak region of the picture on top. The fit parameters are displayed in the legend.

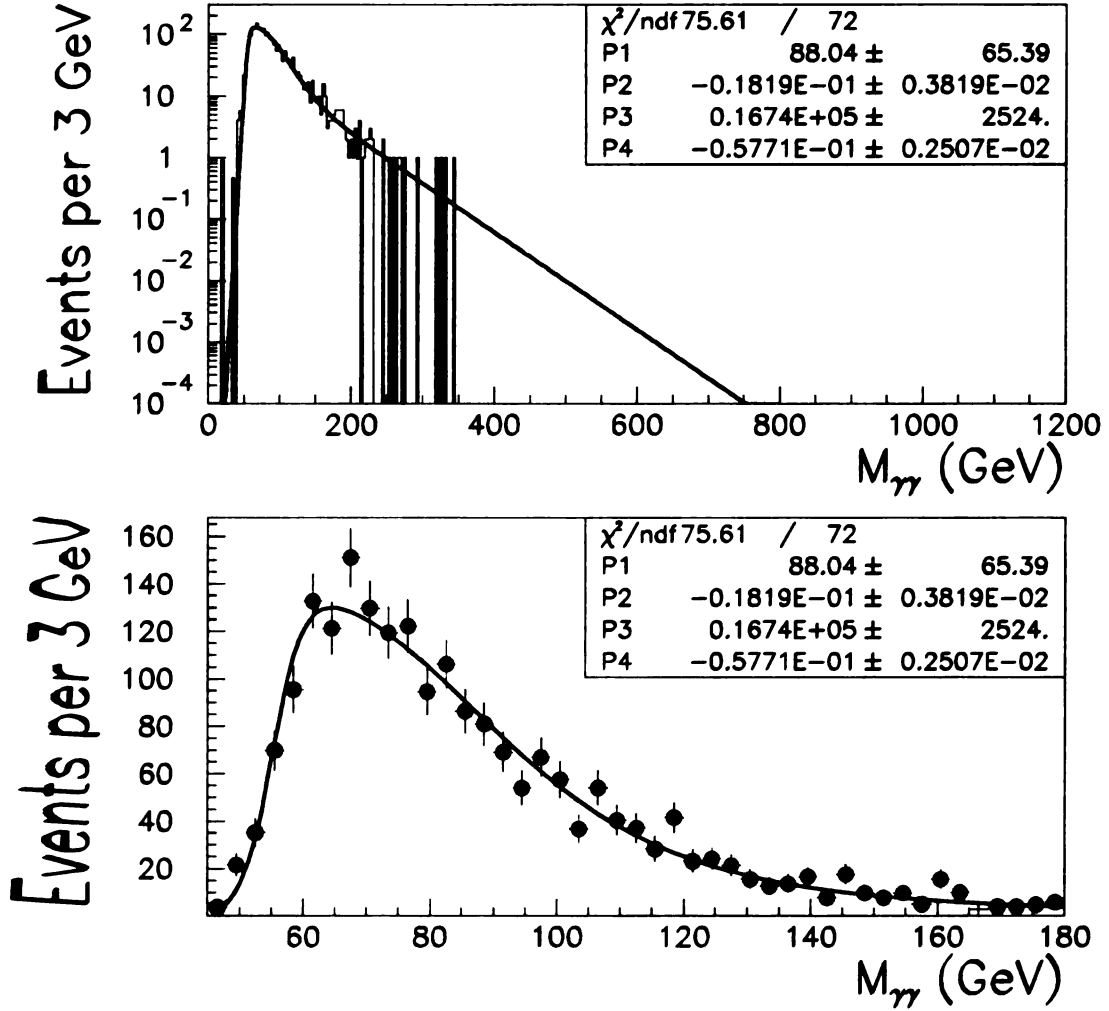


**Figure 6.3:** Top: Invariant mass distribution for the Monte Carlo SM  $\gamma + jet$  events after the CP selection has been applied. The solid line is a fit of the distribution. Bottom: close up in linear scale of the peak region of the picture on top. The fit parameters are displayed in the legend.



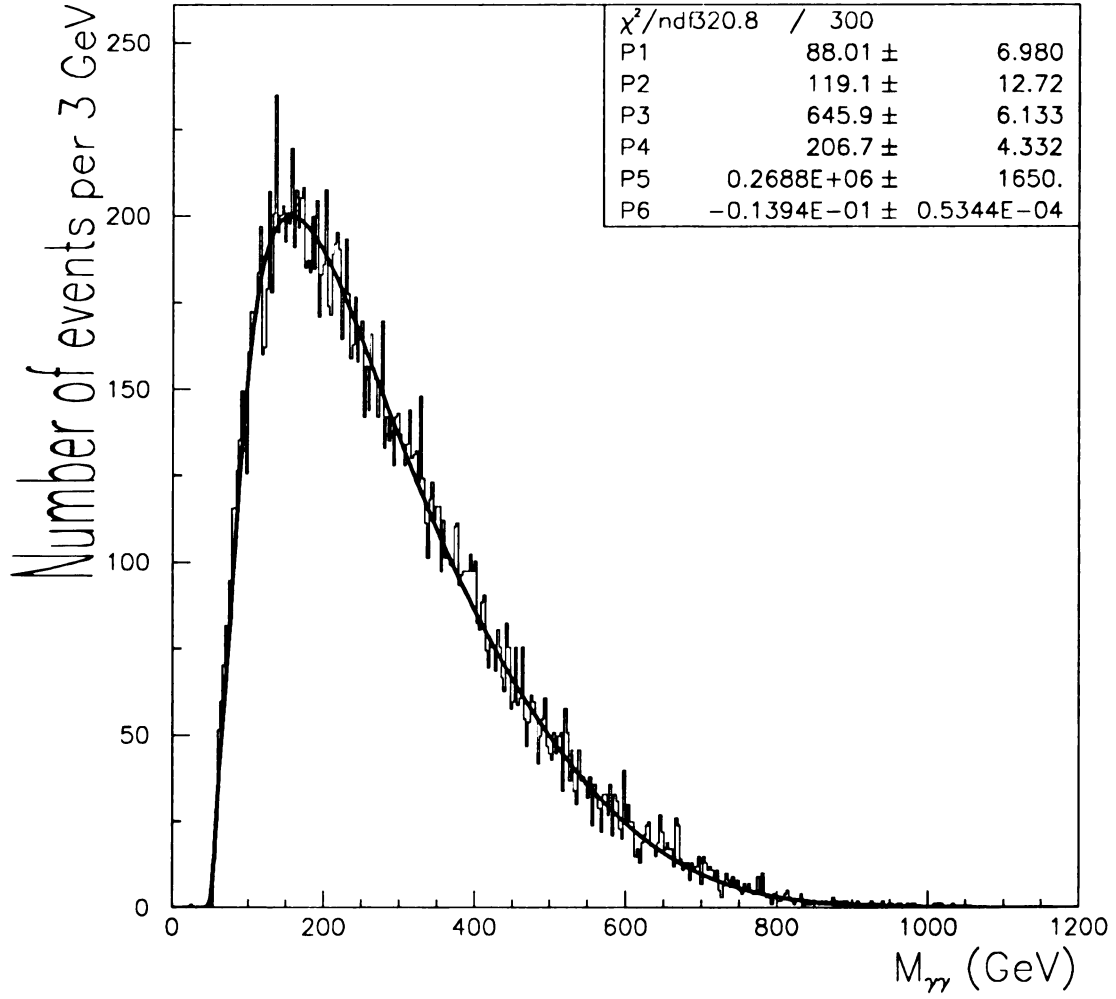


**Figure 6.4:** Invariant mass distribution for the Monte Carlo events resulting from the interference between the SM and LED processes after the CP selection has been applied. The solid line is a fit of the distribution. The fit parameters are displayed in the legend.

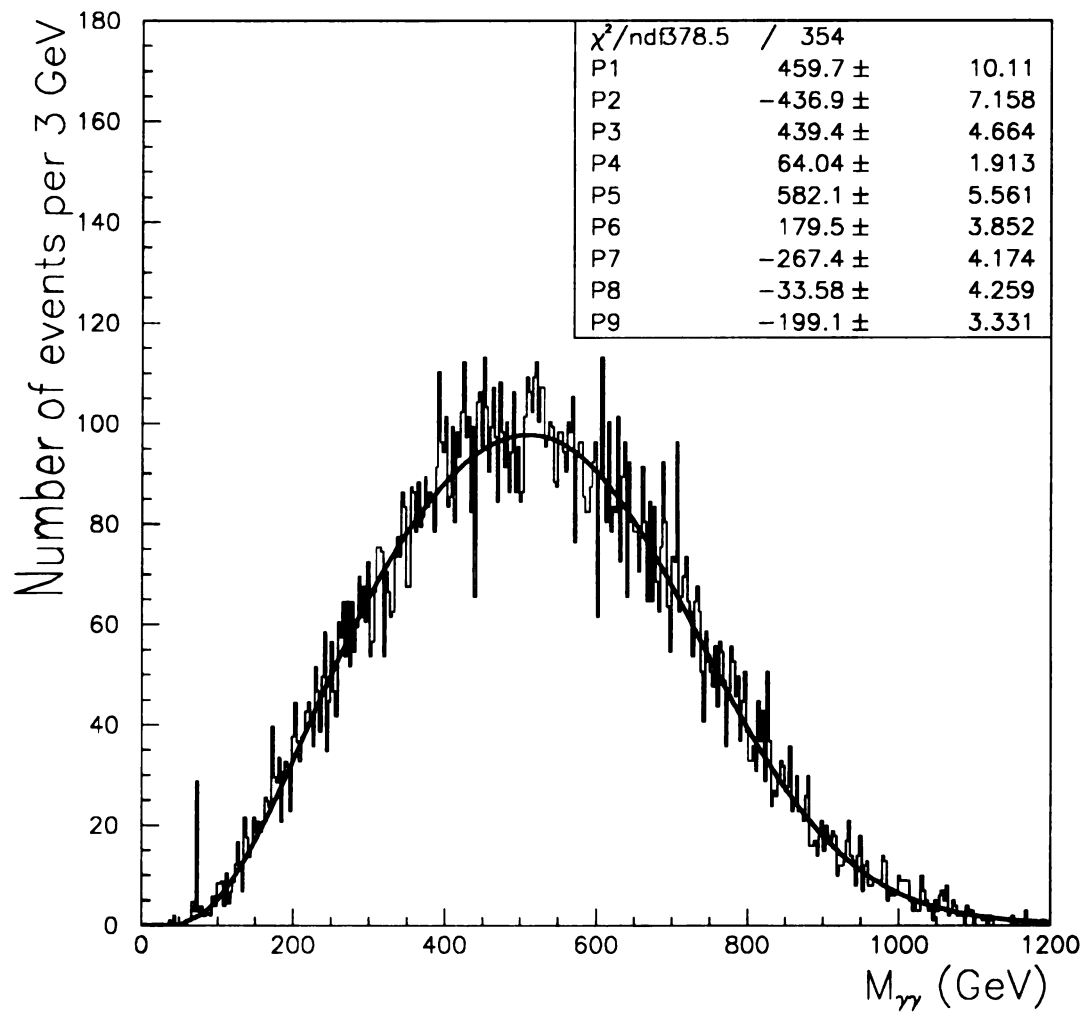


**Figure 6.5:** Invariant mass distribution for the Monte Carlo direct KK events after the CP selection has been applied. The solid line is a fit of the distribution. The fit parameters are displayed in the legend.

Pseudoexperiments with  $\lambda = -1$ ,  $M_S \text{ true} = 600 \text{ GeV}$

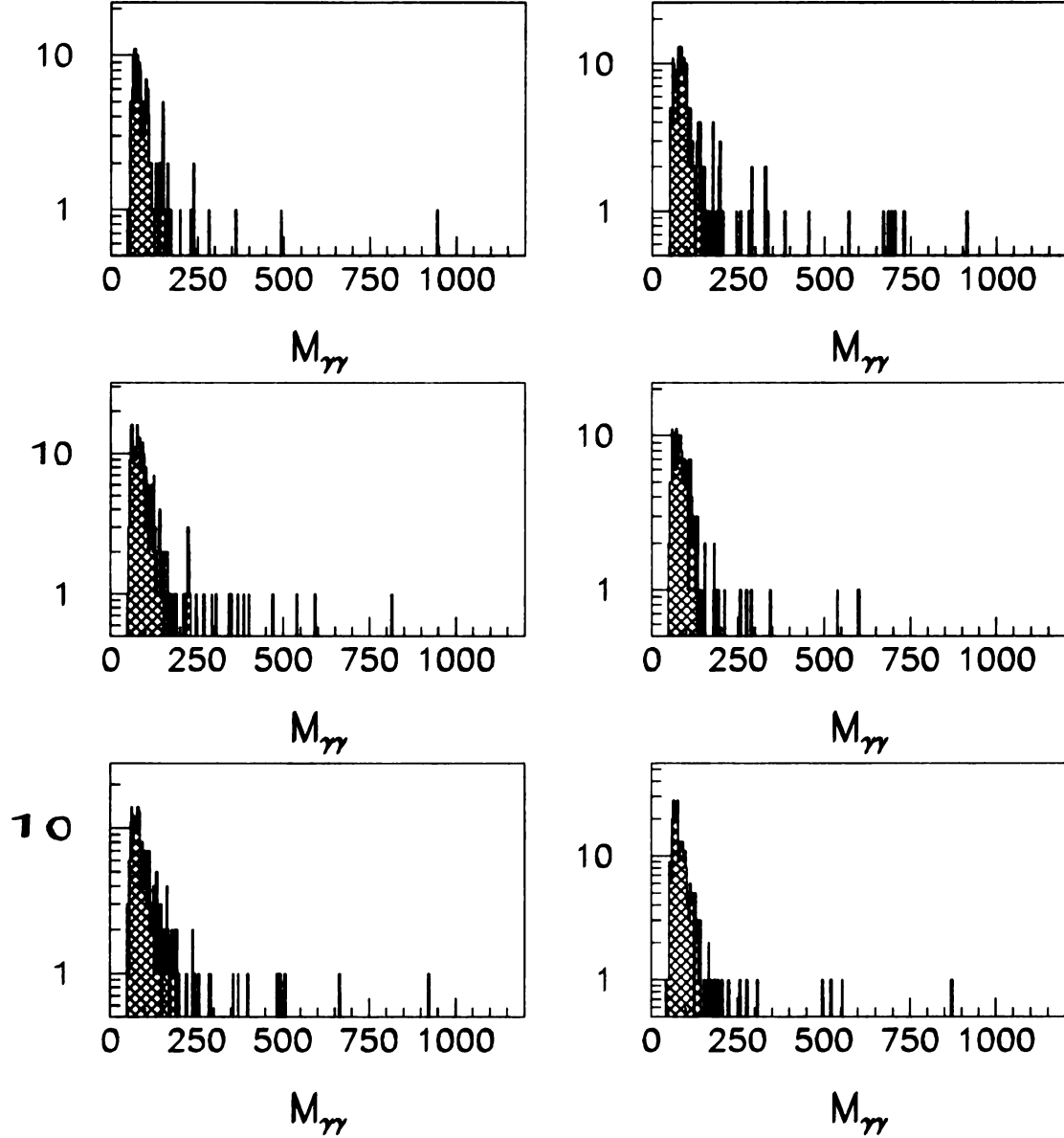


**Figure 6.6:** Invariant mass distribution for pseudoexperiments in presence of extra dimensions generated with  $\lambda = -1$  and  $M_S = 600 \text{ GeV}$ .

Pseudoexperiments with  $\lambda=+1$ ,  $M_S$  true=600 GeV

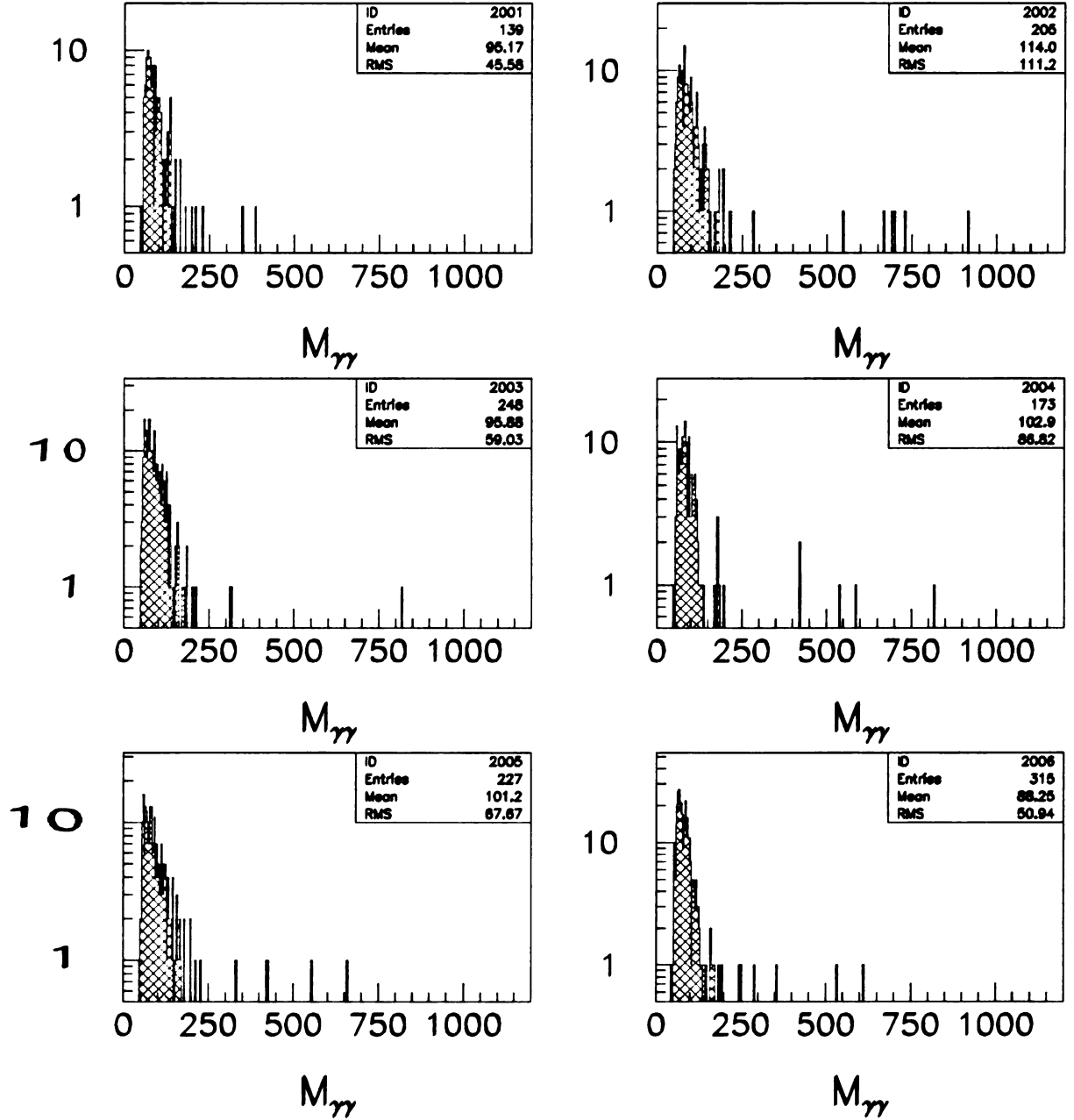


**Figure 6.7:** Invariant mass distribution for pseudoexperiments in presence of extra dimensions generated with  $\lambda = +1$  and  $M_S=600$  GeV.

Next,  $-\ln(L)$  is minimized for each pseudoexperiment with respect to the three parameters,  $n_{SM}$ ,  $n_b$  and  $\eta$ . The values of  $\eta$  as well as the corresponding  $M_S$ 's that minimize the likelihood function for each pseudoexperiments are plotted in figure 6.8. By fitting these distributions with a gaussian, we find that the mean is approximately 600 GeV in very good agreement with  $M_S^{true}$  used to generate the events. In figure 6.9 the results of the fit for the other two fit parameters,  $n_{SM}$  and  $n_b$ , are shown. Their fitted values are also consistent with the predicted values in the data.

## 6.5 Monte Carlo Sensitivity

To test the performance of the fitter in absence of extra dimension, we generate 1000 pseudoexperiments with  $\eta=0$ . The invariant mass distributions for a random sample of pseudoexperiments is shown in figure 6.10. The pseudoexperiments are simulated just as described in section 6.4 but without LED diphotons as  $\eta=0$  is assumed in this case.

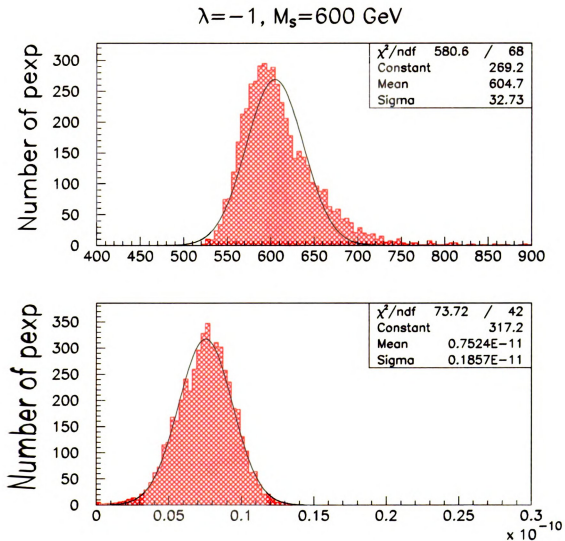


**Figure 6.8:** Fitted values of  $M_S$  (top plot) and  $\eta$  (bottom plot) for  $\lambda=-1$ . The gaussian fit is shown. The mean value of the distribution agrees well with value of  $M_S^{\text{true}}$  used to generate the pseudoexperiments.

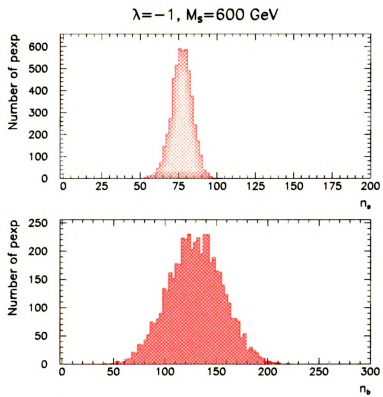
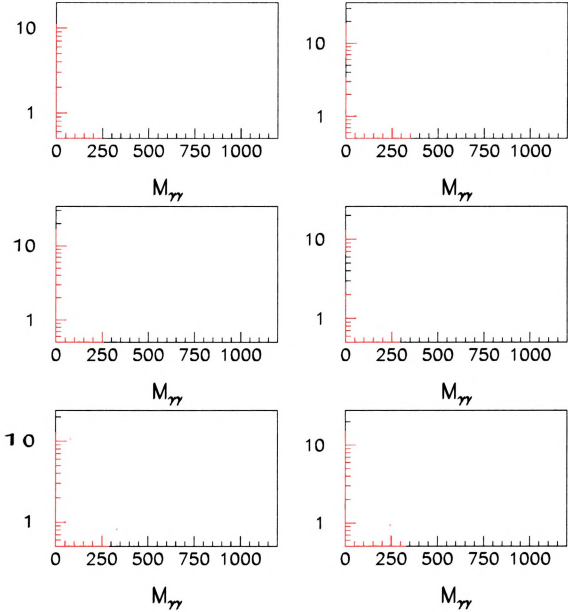


Figure 6.9: Fitted values of  $n_{SM}$  (top plot) and  $n_b$  (bottom plot) for  $\lambda = -1$ .

### Pseudoexperiments with no LED



**Figure 6.10:** Invariant mass distribution for pseudoexperiments in absence of extra dimensions ( $\eta = 0$ ).



We minimize the likelihood function by fixing  $\eta$  and leaving  $n_{SM}$  and  $n_b$  free to vary. We do it for a range of  $\eta$  between 0 and  $1.25 \times 10^{-11}$ . We then calculate the 95% C.L. limit on  $\eta$ ,  $\eta_{95}$ , by performing the integral of the normalized likelihood function. The value of  $\eta$  for which the following expression is satisfied:

$$\frac{\int_0^{\eta_{95}} L(\eta) d\eta}{\int_0^\infty L(\eta) d\eta} = 0.95 \quad (6.7)$$

is the 95% C.L. limit on  $\eta$ . The same is done for negative values of  $\eta$  in the same interval. The  $\eta_{95}$ 's for each of the pseudoexperiments are shown in figure 6.11. In the same plot, the 95% C.L. limits from the data, discussed in the next section, are displayed. The sensitivity for each value of  $\lambda$  is defined as the median of these distributions. We find (in Hewett convention):

- $\lambda = -1 \Rightarrow \eta_{95}^{median} = 4.062 \times 10^{-12} \text{ GeV}^{-4}$ ,  $M_S = 704 \text{ GeV}$
- $\lambda = +1 \Rightarrow \eta_{95}^{median} = 5.674 \times 10^{-12} \text{ GeV}^{-4}$ ,  $M_S = 648 \text{ GeV}$

## 6.6 Limits

The same procedure described in the previous section is used to set a limit on  $\eta$  with the CP data. The minimization procedure yields:

- $\lambda = -1 \Rightarrow \eta_{95} = 3.467 \times 10^{-12} \text{ GeV}^{-4}$ ,  $M_S = 733 \text{ GeV}$
- $\lambda = +1 \Rightarrow \eta_{95} = 5.728 \times 10^{-12} \text{ GeV}^{-4}$ ,  $M_S = 646 \text{ GeV}$

The values of the normalized likelihood function for the scanned values of  $\eta$  are shown in figure 6.12 for both signs of  $\lambda$ , and the limits are indicated with an arrow.

## 6.7 Systematics

We consider the effects from the following sources:

- Different choice of PDF. We consider CTEQ5HJ and MRST(h-g) versus the default CTEQ5M. MRST (h-g) increases the gluon fractions and CTEQ5HJ provides a better fit to high  $E_T$  jet measurements at the Tevatron.
- Initial state radiation (ISR). This includes radiation given off by the partons in the initial state and is simulated by Pythia. The default is to have this option active. As a systematic effect, we turn ISR off.
- Shape of the fakes. We fit the fake distribution with 1 exponential (instead of two as in the default). As an additional variation, we fit the invariant mass distribution for non-isolated events in the CP data sample (figure 6.13).
- Shape of  $\frac{\sigma(\pi^0\pi^0)}{\sigma(\gamma\pi^0)}$ . We shift the shape of the fit to include the maximum variation allowed by each point (figure 6.14).
- Relative normalization between  $jet + jet$  and  $\gamma + jet$  contributions.  $jet + jet$  events account for  $\approx 50\%$  of the fakes while the  $jet + \gamma$  events account for the remaining 50%. As a systematic variation, the ratio is varied to 70%/30% and 30%/70% respectively, according to the 30% uncertainty associated with the prediction.
- The interference between SM and LED  $gg$  initial state is not included in the Monte Carlo. We include this uncertainty in the systematics by varying the interference cross section for  $q\bar{q}$  initial states by  $\pm 100\%$ . This is an overestimate as the  $gg$  interference is certainly smaller than the  $q\bar{q}$ .
- Systematic uncertainties on efficiencies, acceptance, luminosity and background estimates. These uncertainties are already included in the width of the gaussian constraints incorporated in the likelihood function.

Table  
into t

<u><math>\eta</math></u>
0.
1.
1.
2.
2.
3.
3
4
4
5
5
6
6
7
7
8
8
9
=

For  
val  
and  
of  
the  
ad  
and

Table 6.1:  $\delta\eta_{95}$  in  $TeV^{-4}$  corresponding to the systematic uncertainties incorporated into the limit for  $\lambda = -1$ .

$\eta$	PDF $\delta\eta_{95}$	ISR $\delta\eta_{95}$	$\pm 100\%$ INT $\delta\eta_{95}$	Fake shape $\delta\eta_{95}$	Shift $\frac{\sigma(\pi^0\pi^0)}{\sigma(\gamma\pi^0)}$ $\delta\eta_{95}$	$\frac{jet+jet}{\gamma+jet}$ $\delta\eta_{95}$	Total $\Delta\eta_{95}$
0.5	0.0655	0.152	0.156	0.525	0.0546	0.127	0.588
1.0	0.0484	0.165	0.317	0.532	0.0867	0.141	0.665
1.5	0.0960	0.178	0.549	0.494	0.0915	0.133	0.782
2.0	0.0418	0.129	0.607	0.523	0.163	0.204	0.854
2.5	0.0272	0.123	0.789	0.544	0.143	0.137	0.986
3.0	0.202	0.108	0.919	0.475	0.107	0.134	1.07
3.5	0.302	0.174	1.05	0.608	0.192	0.293	1.31
4.0	0.257	0.120	1.10	0.549	0.192	0.162	1.29
4.5	0.316	0.0976	1.33	0.601	0.190	0.234	1.53
5.0	0.377	0.117	1.33	0.596	0.197	0.305	1.55
5.5	0.444	0.0734	1.48	0.695	0.179	0.385	1.75
6.0	0.462	0.0709	1.60	0.690	0.253	0.226	1.83
6.5	0.413	0.0680	1.45	0.628	0.152	0.190	1.65
7.0	0.742	0.157	1.42	0.832	0.394	0.182	1.86
7.5	0.725	0.00868	1.49	0.709	0.167	0.231	1.82
8.0	0.445	0.0217	1.62	0.518	0.106	0.162	1.77
8.5	0.487	0.0611	1.40	0.604	0.0844	0.206	1.62
9.0	0.406	0.0135	1.44	0.656	0.126	0.0639	1.64

For each of the systematics, we generate 200 pseudoexperiments for a range of  $\eta$  values in the region of sensitivity. The shift  $\delta\eta_{95}$  between the default average  $\eta_{95}$  and the average  $\eta_{95}$  from the systematic in question is calculated. The  $\delta\eta_{95}$  for each of the systematics are then added in quadrature for each of the  $\eta$  points. Although the systematic uncertainties on the background are correlated, they are nevertheless added in quadrature and thus will yield a conservative result. The  $\delta\eta_{95}$ 's for  $\lambda = -1$  and  $\lambda = +1$  are tabulated in tables 6.1 and 6.2 respectively.

Table 6.2:  $\delta\eta_{95}$  in  $TeV^{-4}$  corresponding to the systematic uncertainties incorporated into the limit for  $\lambda = +1$ .

$\eta$	PDF $\delta\eta_{95}$	ISR $\delta\eta_{95}$	$\pm 100\%$ INT $\delta\eta_{95}$	Fake shape $\delta\eta_{95}$	Shift $\frac{\sigma(\pi^0\pi^0)}{\sigma(\gamma\pi^0)}$ $\delta\eta_{95}$	$\frac{jet+jet}{\gamma+jet}$ $\delta\eta_{95}$	Total $\Delta\eta_{95}$
0.5	0.0915	0.0776	0.165	0.659	0.213	0.172	0.741
1.0	0.110	0.0962	0.144	0.636	0.180	0.253	0.737
1.5	0.0781	0.0331	0.165	0.633	0.112	0.205	0.699
2.0	0.0907	0.0423	0.369	0.575	0.113	0.0901	0.705
2.5	0.224	0.0794	0.213	0.639	0.248	0.276	0.805
3.0	0.0498	0.0230	0.371	0.547	0.0717	0.115	0.677
3.5	0.0788	0.136	0.616	0.681	0.106	0.354	1.00
4.0	0.166	0.0826	0.854	0.633	0.318	0.315	1.17
4.5	0.0924	0.0959	0.639	0.579	0.141	0.441	0.983
5.0	0.330	0.0870	0.915	0.703	0.192	0.570	1.34
5.5	0.717	0.391	1.22	0.436	0.480	0.622	1.72
6.0	0.551	0.453	2.41	0.243	0.136	0.181	2.54
6.5	0.235	0.345	1.97	0.414	0.585	1.32	2.51
7.0	1.56	0.0923	2.45	0.379	0.239	1.09	3.14
7.5	0.131	0.0769	3.09	0.394	0.236	0.607	3.18
8.0	0.457	0.317	2.64	1.10	1.22	1.24	3.39
8.5	0.746	0.282	3.91	0.981	0.612	2.13	4.67
9.0	1.50	0.779	3.81	0.220	0.615	1.55	4.50

## 6.8 Limits with Systematics Included

The likelihood function is reevaluated by replacing each  $\eta$  bin by a gaussian with width  $\Delta\eta$ , given by the  $\delta\eta_{95}$ 's added in quadrature (the numerical values of the  $\Delta\eta$ 's are in the last column of table 6.1 for  $\lambda = -1$  and table 6.2 for  $\lambda = +1$ ):

$$L_{smeared}(\eta) = \int_0^\infty L(\eta') \frac{1}{\sqrt{2\pi}\Delta\eta} e^{-\frac{(\eta-\eta')^2}{2\Delta\eta^2}} d\eta'$$

The results of the minimization procedure are (in Hewett convention):

- $\lambda = -1 \Rightarrow \eta_{95}=3.755 \times 10^{-12} \text{ GeV}^{-4}, M_S=718 \text{ GeV}$
- $\lambda = +1 \Rightarrow \eta_{95}=5.991 \times 10^{-12} \text{ GeV}^{-4}, M_S=639 \text{ GeV}$

The corresponding smeared likelihood functions are shown in figure 6.15.

## 6.9 Conclusions

We have set limits on Large Extra Dimensions with Run I Central-Plug diphotons, corresponding to  $87 \text{ pb}^{-1}$ . The limits in Hewett convention are:

- $\lambda=-1 \Rightarrow \eta_{95}=3.755 \times 10^{-12} \text{ GeV}^{-4}, M_S=718 \text{ GeV}$
- $\lambda=+1 \Rightarrow \eta_{95}=5.991 \times 10^{-12} \text{ GeV}^{-4}, M_S=639 \text{ GeV}$

The CP diphoton data superimposed to the excluded LED signal is shown in figure 6.16. In GRW notation (see section 2.5) the limit is:

- $M_S(\text{GRW})=804 \text{ GeV}$

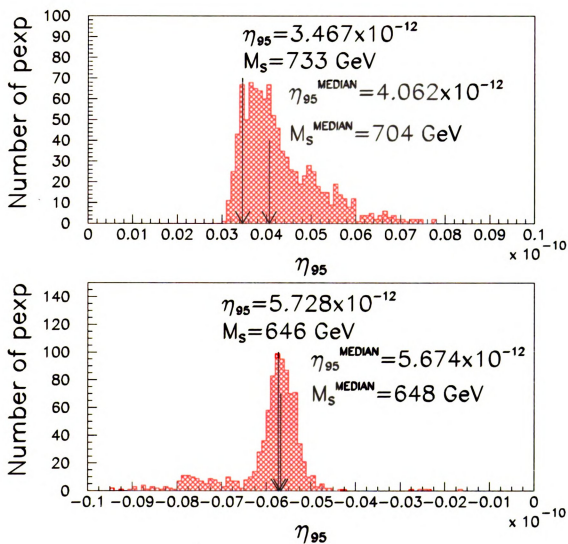


Figure 6.11: Top: distribution of  $\eta_{95}$  for the 1000 pseudoexperiments and median for  $\lambda = -1$ . Bottom: same as in the top plot but for  $\lambda = +1$ .

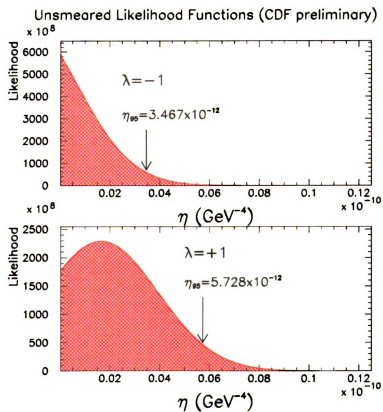


Figure 6.12: Top: Likelihood function for equally spaced values of  $\eta$  for the events in the CP data sample ( $\lambda = -1$ ). Bottom: same as in the top plot but for  $\lambda = +1$ .



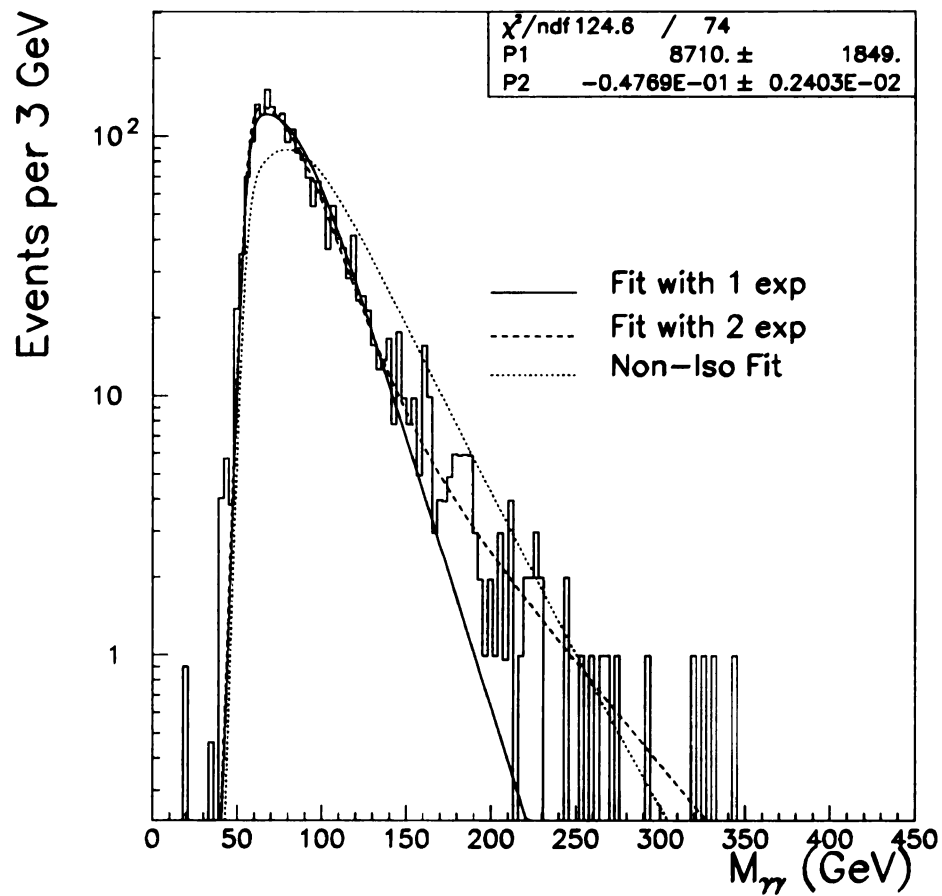


Figure 6.13: Default fit to the  $\gamma + jet$  invariant mass distribution for Pythia events (dashed line). The two variation of the shape included in the limit as a systematic uncertainty are also displayed.

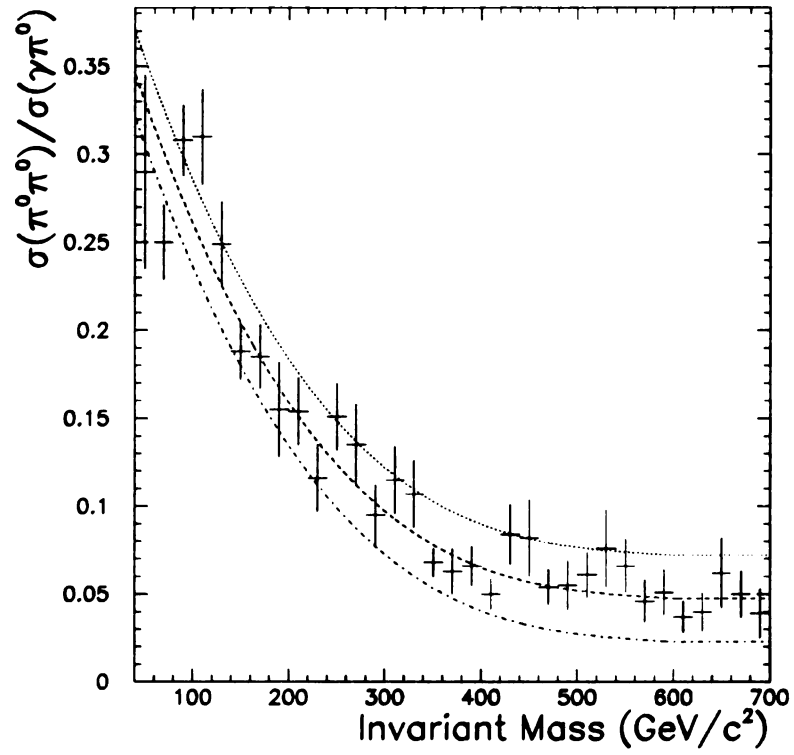


Figure 6.14: Ratio between the  $\pi^0\pi^0$  and  $\gamma\pi^0$  cross sections versus the invariant mass of the pair. Fit with a polynomial (dashed line).  $\pm 1\sigma$  shift (dotted and dash-dotted lines).

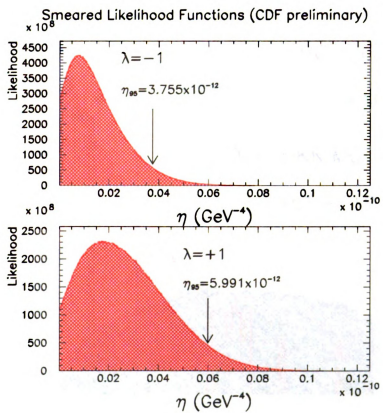


Figure 6.15: Top: Smeared likelihood function for  $\lambda = -1$  for the events in the CP data sample. Bottom: same as in the top plot but for  $\lambda = +1$ .

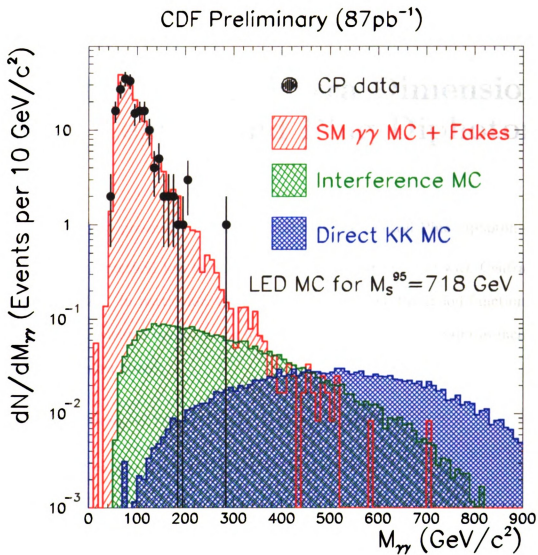


Figure 6.16: The circles represent the Central-Plug data. The LED signal corresponding to the  $\lambda = -1$  limit is superimposed.

## Chapter 7

# Limit on Large Extra Dimensions with Central and Plug Diphotons

In chapter 6 we presented a limit on LED with the Central-Plug diphoton sample.

The same method has been applied to set a limit on LED with Central-Central diphotons [27]. In particular, the same structure of the likelihood function was employed. This yielded the following limits on  $\eta$  (systematic uncertainties included,  $M_S$  in Hewett convention):

- $\lambda=-1 \Rightarrow \eta_{95}=1.74 \times 10^{-12} \text{ GeV}^{-4}, M_S=870 \text{ GeV}$
- $\lambda=+1 \Rightarrow \eta_{95}=2.34 \times 10^{-12} \text{ GeV}^{-4}, M_S=808 \text{ GeV}$

In this chapter, we proceed by setting a limit on LED by combining the Central-Central and Central-Plug diphotons. This is achieved by simply taking the same likelihood functions used in each case and multiplying them together.

### 7.1 Combined Likelihood Function

The likelihood function used to set a limit on LED with Central-Plug diphotons has been shown in equation 6.8. In order to set the combined limit on LED, we multiply

the CP likelihood by its CC counterpart:

$$L = \prod_{i=CC,CP} \left\{ \frac{1}{\sqrt{2\pi}\sigma_{b,i}} e^{-\frac{(N_{b,i}-n_{b,i})^2}{2\sigma_{b,i}^2}} \times \frac{1}{\sqrt{2\pi}\sigma_{SM,i}} e^{-\frac{(N_{SM,i}-n_{SM,i})^2}{2\sigma_{SM,i}^2}} \times \right. \\ \left. \frac{(n_{SM,i} + n_{INT,i}(\eta) + n_{KK,i}(\eta) + n_{b,i})^{N_i} e^{-(n_{SM,i}+n_{INT,i}(\eta)+n_{KK,i}(\eta)+n_{b,i})}}{N_i!} \times \right. \\ \left. \prod_{j=1}^{N_i} \frac{n_{SM,i}f_{SM,i}(M_j) + n_{INT,i}(\eta)f_{INT,i}(M_j) + n_{KK,i}(\eta)f_{KK,i}(M_j) + n_{b,i}f_{b,i}(M_j)}{n_{SM,i} + n_{INT,i}(\eta) + n_{KK,i}(\eta) + n_{b,i}} \right\} \quad (7.1)$$

There are five free fit parameters in the combined likelihood function:

- $\eta = \frac{\lambda}{M_S^4}$ . This parameter is common to the CC and the CP factors.
- $n_{SM,CP}$  and  $n_{b,CP}$  are fit parameters respectively for the number of SM  $\gamma\gamma$  events and for the number of fakes in the Central-Plug sample.
- $n_{SM,CC}$  and  $n_{b,CC}$  are fit parameters respectively for the number of SM  $\gamma\gamma$  events and for the number of fakes in the Central-Central sample.

The other parameters are:

- $N_i$  is the total number of events observed, 287 (i=CC), 192 (i=CP).
- $N_{b,i}$  is the predicted number of fakes, 184 (i=CC), 132 (i=CP).
- $N_{SM,i}$  is the predicted number of SM  $\gamma\gamma$  events, 96 (i=CC), 76 (i=CP).
- $\sigma_{b,i}$  is the uncertainty on the fake estimate, 63 (i=CC), 31 (i=CP).
- $\sigma_{SM,i}$  is the uncertainty on the SM  $\gamma\gamma$  estimate, 31 (i=CC), 14 (i=CP).
- $n_{INT,i}(\eta)$  and  $n_{KK,i}(\eta)$  are the predicted number of LED  $\gamma\gamma$  events, calculated as follows:

$$n_{LED,i}(\eta) = n_{INT,i}(\eta) + n_{KK,i}(\eta) = C_{INT,i} \times \eta + C_{KK,i} \times \eta^2 \quad (7.2)$$

$$\begin{aligned}
C_{\text{INT},i} &= \mathcal{L}_i \times \sigma_{\text{INT}}(\eta_{\text{gen}}) \times \text{CF}_i \times \text{ACC}_{\text{INT},i} \times \frac{1}{\eta_{\text{gen}}} \\
C_{\text{KK},i} &= \mathcal{L}_i \times \sigma_{\text{KK}}(\eta_{\text{gen}}) \times \text{CF}_i \times \text{ACC}_{\text{KK},i} \times \frac{1}{\eta_{\text{gen}}^2}
\end{aligned} \tag{7.3}$$

where, in the CC case, the parameters are (the parameters in the CP case have been listed in section 6.3):

- $\mathcal{L}_{\text{CC}} = 100\text{pb}^{-1}$  is the luminosity of the CC data.
  - $\text{CF}_{\text{CC}} = 0.724 \pm 0.081$  is the correction factor for the CC selection [18, 27].
  - $\sigma_{\text{INT}}(\eta_{\text{gen}}) = 0.05090\text{pb}$  is the cross section for the interference component evaluated by VDEC\_ED for  $\eta = \eta_{\text{gen}} = 10^{-12}\text{GeV}^{-4}$ .
  - $\sigma_{\text{KK}}(\eta_{\text{gen}}) = 0.02002\text{pb}$  is the cross section for the KK component evaluated by VDEC\_ED for  $\eta = \eta_{\text{gen}} = 10^{-12}\text{GeV}^{-4}$ .
  - $\text{ACC}_{\text{INT,CC}} = 0.298$  is the acceptance $\times$ efficiency for LED events from the interference component for  $\eta = \eta_{\text{gen}} = 10^{-12}\text{GeV}^{-4}$  [27].
  - $\text{ACC}_{\text{KK,CC}} = 0.382$  is the acceptance $\times$ efficiency for LED events from the KK component for  $\eta = \eta_{\text{gen}} = 10^{-12}\text{GeV}^{-4}$  [27].
- $f_{b,i}(M_j)$  are the normalized shapes of the fakes. In the CP case, the  $\gamma + \text{jet}$  and  $\text{jet} + \text{jet}$  components are determined separately, as discussed in 5.3.4. In the CC case, the shape of the fakes is measured from the data ([18, 27]; see also section 5.5).
  - $f_{\text{SM},i}(M_j), f_{\text{INT},i}(M_j), f_{\text{KK},i}(M_j)$  are the normalized shapes of the  $\gamma\gamma$  components, SM and LED. In the CP case, these are the same shapes used in the CP likelihood and discussed in sections 6.2.1 and 6.2.2. In the CC case, the normalized shapes have been determined following the same procedure as in the

CP case, i.e. by generating Monte Carlo samples for LED and SM diphoton production. The CC fits are discussed in [27].

Similarly to the CP case (see section 6.3), the combined likelihood consists of gaussian constraints on the number of predicted SM  $\gamma\gamma$  and fake events for the CP and CC case for a total of 4 gaussian constraints, smeared according to the uncertainty of the prediction (first line in equation 7.1); a Poisson constraint on the observed number of CP diphoton events and an additional Poisson constraint on the observed number of CC diphotons (second line in equation 7.1); a shape factor for the CP case and an additional shape factor for the CC case (third line in equation 7.1).

In order to set a limit on  $\eta$ , we minimize  $-\ln(L)$  with MINUIT.

## 7.2 Performance of the Fit

We perform pseudoexperiments with  $\eta \neq 0$  to verify that the likelihood function correctly predicts the value of  $\eta$  given in input. The pseudoexperiments are generated in a fashion similar to the CP case (see section 6.4) by adding the contribution of Central-Central diphotons. We generate pseudoexperiments for a range of values of  $\eta_{true}$ . The resulting fitted  $\eta$  ( $\eta_{fit}$ ) is plotted versus the input in figure 7.1. We observe very good agreement between the input  $\eta$  and the fitted  $\eta$  for a wide range of values of  $\eta$ . Each point in the plot corresponds to 5000 pseudoexperiments generated for a specific  $\eta_{true}$  for  $\lambda = -1$ .

## 7.3 Monte Carlo Sensitivity for the Central-Central and Central-Plug Combined Sample

We generate pseudoexperiments with  $\eta=0$  and determine the 95% C.L. limit on  $\eta$  ( $\eta_{95}$ ) for each pseudoexperiment by minimizing the combined likelihood for a fixed  $\eta$



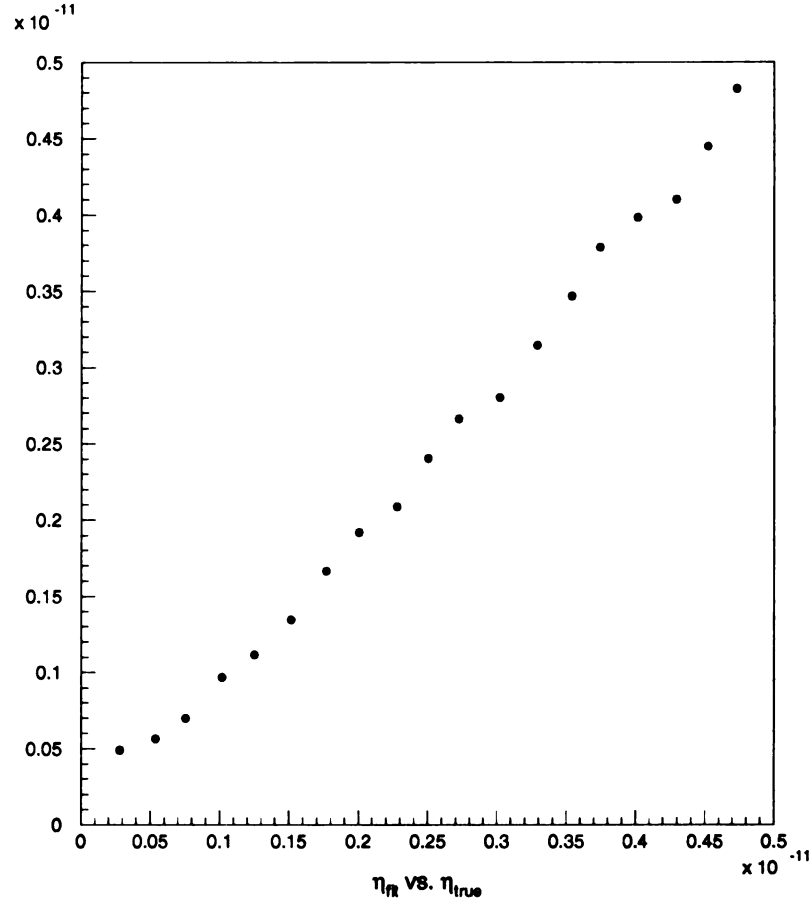


Figure 7.1:  $\eta_{fit}$  ( $\eta$  that minimizes the likelihood function) versus  $\eta_{true}$  ( $\eta$  used to generate pseudoexperiments). The linear correspondence exemplifies the fact that the likelihood function correctly interprets the data in the presence of extra dimensions.

and leaving  $n_{SM,i}$  and  $n_{b,i}$  free to vary ( $i=CC,CP$ ). This is done for a range of values of  $\eta$ . As mentioned in the previous chapter, the value of  $\eta$  for which the following expression is satisfied:

$$\frac{\int_0^{\eta_{95}} L(\eta) d\eta}{\int_0^{\infty} L(\eta) d\eta} = 0.95 \quad (7.4)$$

is the 95% C.L. limit on  $\eta$ . The sensitivity is defined as the median of the  $\eta_{95}$  distribution for the pseudoexperiments (see figure 7.2). We find (Hewett convention):

- $\lambda=-1$ ,  $M_S^{95}=893$  GeV (879 GeV CC only; 704 GeV CP only)

### Null Pseudo-Experiments, $\lambda=-1$

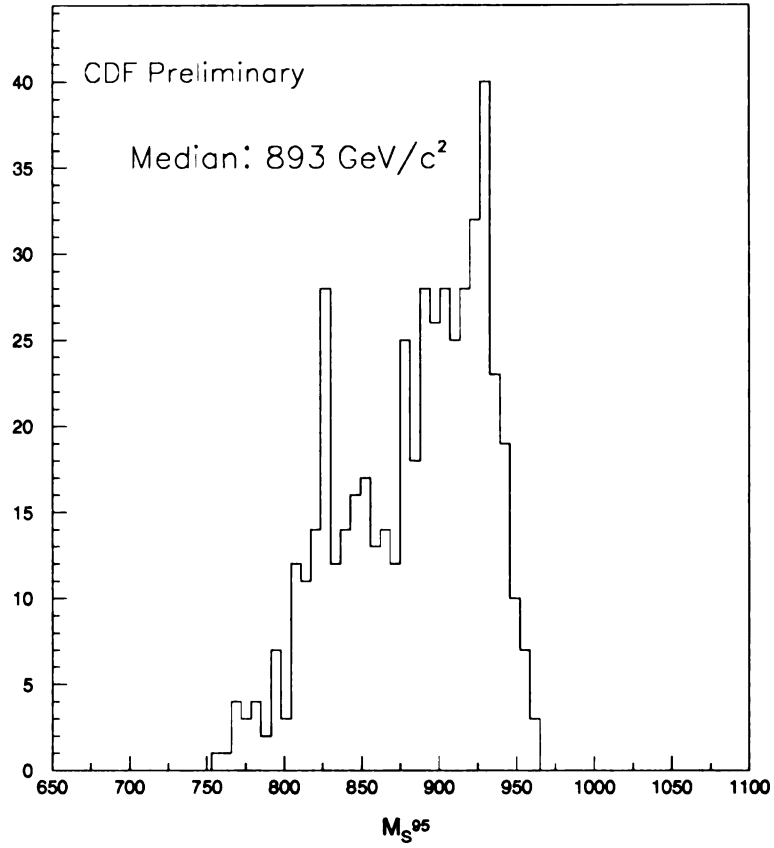


Figure 7.2:  $\eta_{95}$  for the pseudoexperiments. One entry per pseudoexperiment.

- $\lambda=+1$ ,  $M_S^{95}=822$  GeV (812 GeV CC only; 648 GeV CP only)

## 7.4 Data $\eta_{95}$

The same procedure is applied to the CC+CP data and yields (Hewett convention):

- $\lambda=-1$ ,  $M_S^{95}=926$  GeV
- $\lambda=+1$ ,  $M_S^{95}=823$  GeV

## 7.5 Systematic Effects

The sources of systematic uncertainty included in the limit are listed below:

- Different choice of PDF. We consider CTEQ5HJ and MRST(h-g) vs the default CTEQ5M.
- Turn off ISR in Pythia.
- Uncertainty in the CP fakes (shape of fakes and relative fraction of  $jet + jet$  vs  $\gamma + jet$  events. See section 6.7 for more details).
- The interference between SM and LED  $gg$  initial state is not included in the Monte Carlo. We include this uncertainty in the systematics by varying the interference cross section by  $\pm 20\%$ . This choice is the result of the following estimate. In the SM diphoton production, the  $gg$  processes account for  $\sim 30\%$  of the diphoton cross section at leading order. We assume a similar contribution of the  $gg$  processes to LED diphoton production. This yields  $(0.30)^2 \sim 0.10$ , thus the  $gg$  contribution to the interference is about 10% of the  $q\bar{q}$  counterpart. In order to be conservative, we vary the interference contribution by  $\pm 20\%$ .
- Systematic uncertainties on efficiencies, acceptance, luminosity and background estimates. These uncertainties are already included in the width of the gaussian constraints incorporated in the likelihood function.

We smear the likelihood function by convolving it with a gaussian of width  $\delta\eta_{fit}$  determined in the following way:

- We generate 100 pseudoexperiments for a range of values of  $\eta$  with  $100\times$  the statistic in the data and for each of the systematics. The large statistics (larger

Table 7.1:  $\delta\eta_{95}$  in  $TeV^{-4}$  corresponding to the systematic uncertainties incorporated into the combined limit for  $\lambda = -1$  and  $\lambda = +1$ .

$\eta$	$\delta\eta(\lambda = -1)$	$\delta\eta(\lambda = +1)$
0.3	0.34	0.36
0.6	0.30	0.42
0.9	0.28	0.48
1.2	0.30	0.67
1.5	0.28	0.41
1.8	0.23	0.61
2.1	0.28	0.53
2.4	0.24	0.45
2.7	0.28	0.69
3.0	0.27	0.62

than in the CP case) is employed to reduce statistical fluctuations in the fits.

This is repeated for a range of  $\eta$  values.

- The  $\eta_{fit}$  that minimizes the likelihood function is calculated.
- The shifts between the default average  $\eta_{fit}$  and the average  $\eta_{fit}$  from different sources of systematics are then added in quadrature for each of the  $\eta$  points. The  $\delta\eta_{fit}$  in  $TeV^{-4}$  corresponding to the systematic uncertainties incorporated into the limit for  $\lambda = \pm 1$  are tabulated in table 7.1.

The unsmeared (i.e. without systematics) and smeared likelihood functions are shown in figures 7.3 and 7.4.

## 7.6 Combined Limits

The results with systematic uncertainties included are (in Hewett convention):

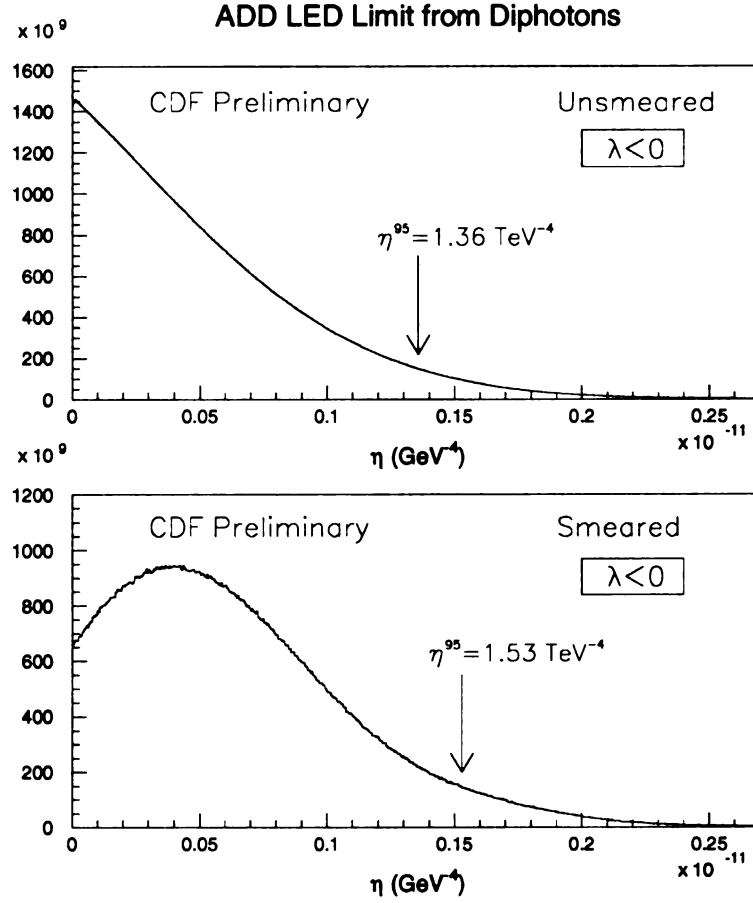


Figure 7.3: Unsmeared (top) and smeared (bottom) likelihood function for the combined CC+CP diphoton data sample for  $\lambda = -1$ .

- $M_S^{95} = 899 \text{ GeV}$  (870 GeV CC only)
- $M_S^{95} = 797 \text{ GeV}$  (808 GeV CC only)

The CP sample improves the CC limit by approximately 30 GeV in the case of constructive interference. In GRW notation, the limit is:

- $M_S(\text{GRW}) = 1006 \text{ GeV}$

In figures 7.5 and 7.6 the excluded signal is superimposed to the data. The plots also include the SM  $\gamma\gamma$ +fakes prediction and good agreement with the data is observed.

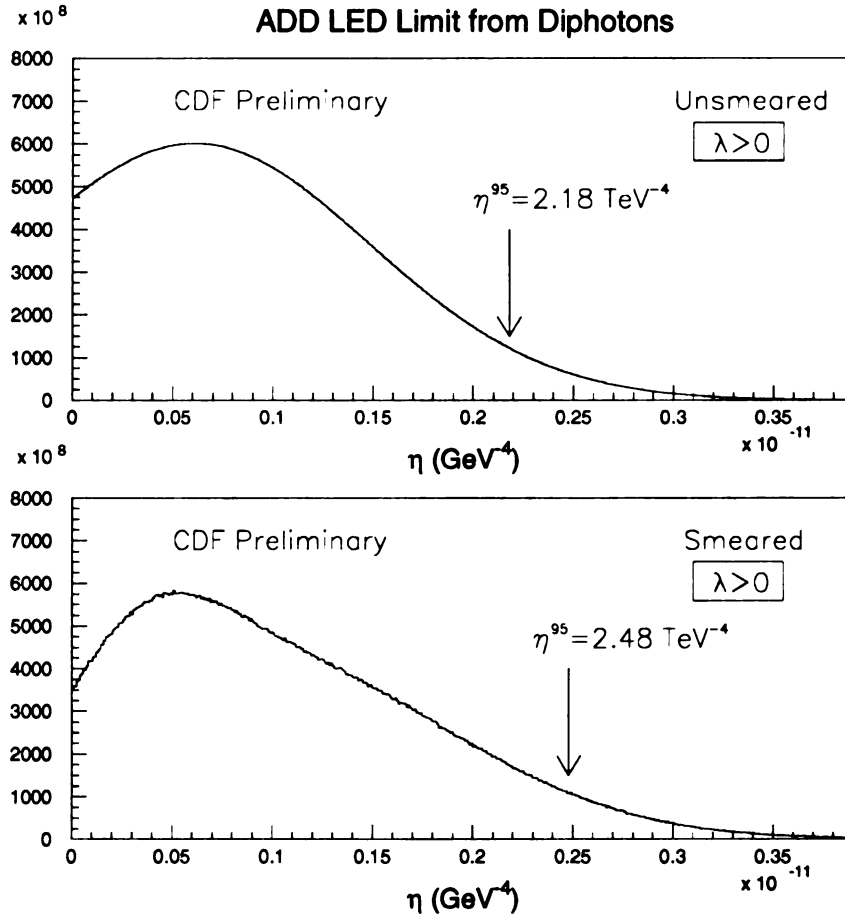


Figure 7.4: Unsmearred (top) and smeared (bottom) likelihood function for the combined CC+CP diphoton data sample for  $\lambda = +1$ .

For  $M_S=899$  GeV (Hewett), there are 1.7 interference and 1.3 direct KK events produced with CC topology, while the CP topology contributes 1.2 interference and 0.3 direct KK events. Thus a total of approximately 5 events is expected from LED sources. This is consistent with the 95% C.L. exclusion with zero events observed.

# CDF Preliminary

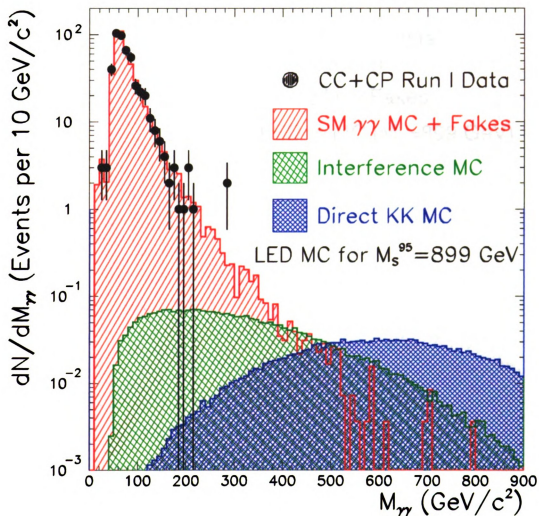


Figure 7.5: Invariant mass distribution for the diphoton data (circles) overlapped with the expected invariant mass distribution from SM  $\gamma\gamma$ +fake sources. The excluded contribution from the direct KK graviton exchange and SM+KK interference is also shown. The LED contribution corresponds to approximately 5 events.

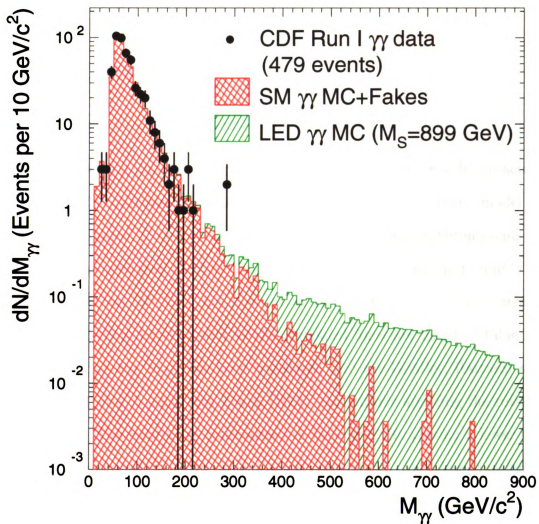


Figure 7.6: Invariant mass distribution for the diphoton data (circles) overlapped with the expected invariant mass distribution from SM  $\gamma\gamma$ +fake sources combined with the excluded contribution from LED sources. The invariant mass contribution from SM  $\gamma\gamma$ +fake sources alone is also shown.





# Chapter 8

## Conclusions

We have placed a limit on the Planck scale in the bulk,  $M_S$ , which characterizes the strength of the graviton interactions in the low-scale quantum gravity model proposed by Arkani-Hamed, Dimopoulos and Dvali (ADD) by using diphoton events collected at CDF. The combined Central-Central and Central-Plug diphoton limit is 899 GeV for  $\lambda = -1$  and 797 GeV for  $\lambda = +1$  in Hewett notation. The Central-Central and Central-Plug limits as well as the combined limit are listed in table 8.1. The combined diphoton limit has been translated into the Giudice, Rattazzi and Wells (GRW) and Han, Lykken and Zhang (HLZ) conventions applying the rules given in section 2.5. The results are summarized in table 8.2. By placing a lower bound on  $M_S$ , also the size of the extra dimensions is constrained. Applying equation 2.1 with  $M_S=899$  GeV, one finds that if there were 2 extra dimensions, their size should be smaller than  $2.5 \times 10^{-3}$  m (2.5 mm). For  $n = 4$ , the limit on  $M_S$  constrains the extra dimensions to be smaller than  $2.3 \times 10^{-11}$  m (23 pm) and if  $n = 6$  the maximum size is  $5.0 \times 10^{-14}$  m (50 fermi).

In addition to the diphoton analysis, LED have been searched at CDF by looking for an excess in the dielectron channel [28, 30]. No excess has been observed in the dielectron channel and thus a 95% C.L. limit on  $M_S$  has been determined. The di-

electron limits in Hewett, GRW and HLZ conventions are summarized in table 8.2. The procedure used to set a limit on  $M_S$  with dielectron events is very similar to the diphoton case and it involves the same general structure of the unbinned likelihood function. The dielectron and the diphoton samples have been combined [29] to improve the reach of the search for LED by following the same procedure used in combining the diphoton Central-Central and Central-Plug samples, i.e. by multiplying the likelihood functions for each of the samples and minimizing it with respect to the free parameters. The combined limits in the different notations are listed in table 8.2. Adding the dielectron sample only improves the diphoton limit by 6 GeV in the case of  $\lambda = -1$  in Hewett convention. The dielectron sample in fact contains one event in which the invariant mass of the  $e^+e^-$  pair is approximately 500 GeV. An event with such an high mass could be consistent with large extra dimensions and thus the dielectron sample is not very effective in improving the limit.

The D0, LEP and HERA collaborations have also searched for extra dimensions in the ADD scenario via virtual graviton exchange processes. No evidence of new physics has been observed. In the rest of this section, a brief summary of limits presented at recent conferences by these collaborations is presented. Unless otherwise specified, Hewett notation is assumed. Although the results are not as recent, more details about these analyses can be found in [34, 35, 36, 37, 38].

The D0 analysis searched for deviations from the SM in diphoton and dielectron events by studying the invariant mass and angular distributions of the pair, while only the invariant mass distribution has been considered at CDF (see section 2.4). The D0 analysis also includes a  $K$  factor of 1.3 to account for next-to-leading order effects for the SM dielectron and diphoton production as well as for the corresponding graviton mediated processes. A 95% C.L. limit was set on  $M_S$  of 1.1 TeV for  $\lambda = +1$  and 1.0 TeV for  $\lambda = -1$  in Hewett convention [31]. The D0 limits in different

Table 8.1:  $M_S^{95}$  in Hewett convention for the Central-Central (CC) and Central-Plug (CP) samples individually and combined (CC+CP) with  $K = 1.0$ .

Sample	$M_S^{95}$ (GeV)	
	$\lambda = -1$	$\lambda = +1$
CC $\gamma\gamma$	870	808
CP $\gamma\gamma$	718	639
CC+CP $\gamma\gamma$	899	797

Table 8.2: Dielectron and diphoton limits on  $M_S$  in Hewett, GRW, HLZ conventions. The combined dielectron and diphoton limit ( $e^+e^-+\gamma\gamma$ ) has been determined for  $K = 1.0$  and  $K = 1.3$ .

Sample	$K$	$M_S^{95}$ (GeV)							
		Hewett		GRW	HLZ				
		$\lambda=-1$	$\lambda=+1$		$n=3$	$n=4$	$n=5$	$n=6$	$n=7$
CC+CP $\gamma\gamma$	1.0	899	797	1006	1197	1006	909	846	800
$e^+e^-$	1.0	780	768	873	1038	873	789	734	694
$e^+e^-+\gamma\gamma$	1.0	905	826	1013	1205	1013	916	852	806
$e^+e^-+\gamma\gamma$	1.3	939	853	1051	1250	1051	950	884	836

conventions are summarized in table 8.3. The diphoton and dielectron CDF analyses use  $K = 1.0$  (see section 2.4), however, for comparison with the D0 limit, the limit has been recalculated with  $K = 1.3$  [29]. The CDF limits with  $K = 1.3$  in Hewett, GRW and HLZ notations are listed in table 8.2. In Hewett convention, the limit for  $\lambda = -1$  improves by approximately 35 GeV.

At LEP, several results constrain  $M_S$  by searching for graviton mediated processes[32].

The DELPHI collaboration has set a limit on  $M_S$  of 0.81 TeV for  $\lambda = +1$  and

Table 8.3: D0 combined dielectron and diphoton limits on  $M_S$  in Hewett, GRW, HLZ conventions with  $K = 1.3$ . Limits are expressed in  $TeV$ .

	Hewett		$M_S^{95}$ (TeV)		HLZ			
	$\lambda=+1$	$\lambda=-1$	GRW	$n=3$	$n=4$	$n=5$	$n=6$	$n=7$
$K=1.3$	1.1	1.0	1.2	1.4	1.2	1.1	1.0	1.0

0.75 TeV for  $\lambda = -1$  by combining  $\mu^+\mu^-$  and  $\tau^+\tau^-$  final states. At L3, all  $e^+e^- \rightarrow G^* \rightarrow f\bar{f}$  ( $f$  is a fermion in the final state) channels have been investigated and the combined limits are 1.06 TeV ( $\lambda = +1$ ) and 0.98 TeV ( $\lambda = -1$ ). Also the ALEPH collaboration has performed the full  $f\bar{f}$  search. Their limits are 1.18 and 0.81 TeV for  $\lambda = +1$  and  $\lambda = -1$  respectively. At OPAL all channels have been analyzed including graviton mediated diboson production. The limits are 1.03 TeV ( $\lambda = +1$ ) and 1.17 TeV ( $\lambda = -1$ ). LEP collaborations have also computed a combined limit on  $M_S$  with diphoton events only. The lower bounds on  $M_S$  are 0.97 TeV for  $\lambda = +1$  and 0.94 TeV for  $\lambda = -1$ .

Finally, at HERA, the H1 and ZEUS collaborations have searched for graviton exchange contribution to  $eq \rightarrow eq$  scattering. Their limits are weaker compared to the Tevatron and LEP limits. H1 limits are 0.83 for  $\lambda = +1$  and 0.79  $\lambda = -1$  (GRW notation). At ZEUS, the lower bounds on  $M_S$  are 0.81 for  $\lambda = +1$  and 0.82  $\lambda = -1$  (GRW notation).

The Tevatron, LEP and HERA limits cited above comprise analyses that searched for anomalous difermion or diboson production through virtual graviton mediated processes. The collaborations also investigated extra dimensions in the ADD scenario by searching for events where real graviton emission occurred. However, the cross

section for real graviton emission rapidly falls as the number of extra dimensions increases [9, 10]. For this reason, virtual graviton mediated processes offer a more powerful tool to search for extra dimensions when their number is large.

# Bibliography

- [1] For an overview of the Standard Model see G. Kane, “Modern Elementary Particle Physics”, Addison-Wesley, 1987; F. Halzen and A. D. Martin, “Quarks and Leptons: An introductory Course in Modern Particle Physics”, John Wiley and Sons, 1984.
- [2] For an overview of the parton model see S. Ellis, “Introduction to the Parton Model and Perturbative QCD”, CTEQ Summer School Lectures, 2000.
- [3] J. Huston, “Direct Photon Production”, CTEQ Summer School Lectures, 2000.
- [4] D.E. Groom *et al.*, The European Physical Journal **C15** (2000) 1, available on the PDG WWW pages (URL: <http://pdg.lbl.gov/>).
- [5] D. Toback, Searches for New Physics in Diphoton Events in  $p\bar{p}$  Collisions at  $\sqrt{s}=1.8$  TeV, Ph.D. thesis, University of Chicago (1997).
- [6] C. D. Doyle *et al.*, Phys. Rev. Lett. **86**, 1418 (2001); J. C. Long, H. W. Chan, and J. C. Price, Nucl Phys. **B539**, 23 (1999).
- [7] S. Cullen and M. Perelstein, Phys. Rev. Lett. **83**, 268 (1999); L. J. Hall and D. Smith, hep-ph/9904627; V. Barger, T. Han, C. Kao, and R. J. Zhang, hep-ph/9905474; G. C. McLaughlin and J. N. Ng, hep-ph/9909558.
- [8] N. Arkani-Hamed, S. Dimopoulos, and G. Dvali, Phys. Lett. **B249**, 263 (1998), hep-ph/9803315.
- [9] J. Hewett, Phys. Rev. Lett. **82**, 4765 (1999).
- [10] G.F. Giudice, R. Rattazzi, and J.D. Wells, Nucl. Phys. **B544**, 3 (1999).
- [11] T. Han, J. Lykken, and R. Zhang, Phys. Rev. D **59**, 105006 (1999).
- [12] O. J. Eboli, T. Han, M. B. Magro and P. G. Mercadante, Phys. Rev. D **61**, 094007 (2000) [arXiv:hep-ph/9908358].
- [13] K. Cheung, Phys. Lett. **B460**, 383 (1999), hep-ph/9904266.
- [14] K. Cheung and G. Landsberg, hep-ph/9909218.
- [15] John Carlson, David Gerdes, private communication.

- [16] The Collider Detector at Fermilab (CDF), A compilation of articles reprinted from *Nuclear Instruments and Methods in Physics Research - A*, North-Holland (1988).
- [17] P. Wilson, CDF Internal Document 4170.
- [18] CDF Collaboration, T. Affolder *et al.*, Phys. Rev. D **64**, 092002 (2001).
- [19] J. W. Berryhill, A Search for New Physics in Photon-Lepton Events in Proton-Antiproton Collisions at  $\sqrt{s}=1.8$  TeV, Ph.D. thesis, University of Chicago (2000).
- [20] Willis Sakumoto, private communication.
- [21] F. Abe *et al.*, Phys. Rev. D **50**, 2966 (1994).
- [22] H. Bengtsson, and T. Sjöstrand, *Comput. Phys. Commun.* **46**, 43 (1987).
- [23] F. Abe *et al.*, Phys. Rev. Lett. **73**, 2662 (1994).
- [24] We thank Jeff Berryhill for providing the University of Chicago jet data sample.
- [25] F. James and M. Roos, “Minuit’ A System For Function Minimization And Analysis Of The Parameter Errors And Correlations,” *Comput. Phys. Commun.* **10**, 343 (1975).
- [26] J. Owens, private communication.
- [27] D. Gerdes, and D. Berebitsky, CDF Internal Document 5373.
- [28] John Carlson, David Gerdes, Myron Campbell, CDF Internal Document 5391.
- [29] John Carlson, David Gerdes, Simona Murgia, CDF Internal Document 5753.
- [30] John Carlson, David Gerdes, CDF Internal Document 5892.
- [31] B. Abbott *et al.* [D0 Collaboration], Phys. Rev. Lett. **86**, 1156 (2001).
- [32] A review of LEP results is presented in G. Wilkinson, “LEP 2  $e^+e^- \rightarrow f\bar{f}, \gamma\gamma(\gamma)$ : results and interpretations”, XXXVII Recontres de Moriond, Les Arcs, 9-16 March 2002.
- [33] A review of HERA results is presented in J. Scheins, “Search for New Physics at HERA”, XVI Recontres de Physique de la Vallée d’Aoste, La Thuile, 3-9 March 2002.
- [34] M. Barate *et al.* [ALEPH Collaboration], Phys. Lett. B **429**, 201 (1998)
- [35] P. Abreu *et al.* [DELPHI Collaboration], Phys. Rev. B **485**, 45 (2000).
- [36] M. Acciari *et al.* [L3 Collaboration], Phys. Lett. B **464**, 135 (1999); M. Acciari *et al.* [L3 Collaboration], Phys. Lett. B **470**, 281 (1999)
- [37] G. Abbiendi *et al.* [OPAL Collaboration], Eur. Phys. J. C **13**, 553 (2000)
- [38] C. Adloff *et al.* [H1 Collaboration], Phys. Lett. B **479**, 358 (2000)



MICHIGAN STATE UNIVERSITY LIBRARIES



3 1293 02429 2405